QUANTITATIVE THREE-DIMENSIONAL IMAGING OF DROPLET CONVECTION AND CARDIAC CELL MOTIONS BASED ON MICRO DDPIV

Thesis by

Jian Lu

In Partial Fulfillment of the Requirements

for the Degree of

Doctor of Philosophy

California Institute of Technology

Pasadena, California

2008

(Defended November 26, 2007)

Acknowledgements

I would like to take this opportunity to express my sincere thanks to my advisor, Professor Mory Gharib, for his insightful ideas to direct my graduate research, for providing me an environment with great freedom in the group, and for his kind favors and supports in my life.

I would like to thank all members of my committee. Thanks to Professor Changhuei Yang, Dr. Rusty Lansford and Professor Jay Hove for all the discussions and time. Special appreciations to Professor Scott Fraser for his creative ideas directing my project as well as generously letting me use all experimental facilities in his lab.

The Gharib group at Caltech is a great place to work in, and I enjoy every day working with a group of brilliant people here. My thanks go to former group members Dr. Gabe Acevedo-Bolton and Dr. Arian Forouhar for the inspiration and favors they offered when I began to involve in the zebrafish project. I thank Bahram Valiferdowsi for helping me out in all the mechanical designs I used in my research. I thank Dr. Emilio Graff for demonstrating the software package for data analysis. The decent imaging technique I developed in this thesis includes the great efforts from Dr. Francisco Pereira (INSEAN, Italy). I would like to thank all his encouragements and kind favors in this work.

The Fraser lab is the best collaborative place to work with, and I learned a lot of biological methods from this lab. I appreciate Chris Waters for his help in solving

technical problems I met with the facilities. I would like to thank Dr. Le Trinh for answering all the questions I had with zebrafish literature.

Lastly, I want to express my deepest love and gratitude to my family. Thanks to my parents for the love they sent to my heart every moment in my life. My thanks go to my sister for all the help and happiness she brought to me. Especially, I would like to thank my wife, Fan, for being with me, for her unconditional support, and for everything she has done for me.

Abstract

Biomechanical forces such as blood flow induced shear stress as well as genetic programming are widely acknowledged as critical factors regulating vertebrate heart development. While mechanisms of genetic regulation have been well studied, effects of biomechanics are poorly understood due to the lack of proper imaging tools with sufficient spatial and temporal resolutions for quantitative analysis of the mechanical stimuli in complex three-dimensional (3D) living systems. 3D quantitative flow visualization by tracking microscale particles has become an invaluable tool in microfluid mechanics. Defocusing digital particle image velocimetry (DDPIV) can recover depth coordinates by calculating the separation between defocused images generated by an aperture mask with a plurality of pinholes forming an equilateral triangle. In this thesis, a novel high-speed 3D micro-PTV system was developed based on this technique with laser-induced fluorescence to achieve microscale velocity field measurements. Application of this technique to microscale imaging was validated by calibration of targets spread over the image field. A micro volume of 400x300 μm^2 with 100 μm depth has been mapped using an inverted microscope equipped with a 20X objective lens. The proposed technique was successfully applied to 3D tracking of 2-μm fluorescent particles inside an evaporating water droplet, exhibiting convective flow induced by Marangoni effects.

The microscopic imaging system was then utilized to acquire 3D time series data of highly dynamic cell motions in living embryonic zebrafish hearts. 1-μm and 500-nm fluorescent tracer particles were injected into the blood stream of developing zebrafish embryos at 32 hours post fertilization (hpf) to 59 hpf to help describe cardiac cell motions. Microinjection was delicately performed at the fish tail to minimize the influence to normal cardiovascular functions. The measurable depth in an embryonic heart is about 40 μm. 3D velocities of cardiovascular blood flow and trajectories of heart-wall motions were obtained, showing dynamic changes of the flow field and phase differences of wall movements between the atrium and the ventricle during heart beating. Endocardial ventricular strains were calculated based on the reconstructed coordinates of two particles adhered to the endocardium.

Table of Contents

Chapter 3: Microscale 3D flow mapping with μDDPIV……………………….… 29

Chapter 4: 3D flow mapping of droplet internal circulation…………………... 56

List of Figures

Chapter 1

Prologue

1.1 Introduction

There is an increasing development of microscale devices with the applications in both industrial and scientific research. Fluid mechanics is frequently involved in these microscale devices. As a result, quantifying flow related phenomena is an essential feature to consider in device design and application. Micromechanics are ubiquitous in biological processes such as swimming, cell migrations and morphogenesis. One biomechanical stimulus, biofluid flow, induces forces through shear stress, transmural pressure, and circumferential stretch and these have profound impacts on organizational development. Endothelial cells lining the vasculature of vertebrates have been shown to respond to shear stress, undergoing morphological changes which in turn lead to the regulation of cellular functions and organizational changes in the cytoskeleton (Galbraith et al., 1998). Alterations of flow environments inside developing vertebrate bodies have been observed to change the morphology and functions of living tissues (e.g., blood vessels, brain, lung, and heart) as a consequence of the response of endothelial cells (Cartwright et al., 2004; Seki et al., 2003; Kramer-Zucker et al., 2005). Furthermore, biomechanical stimuli are involved in pathogenesis of many diseases in these organs as well (Feldman et al., 2002; Bateman, 2004). The study of cardiogenesis is of considerable interest in biological and medical research. Abnormalities in early vertebrate heart development are the leading form of congenital birth defects. It is well known that genetic regulation plays an important role in heart development. Recent studies have revealed that the shear stress induced by blood flow can cause changes in cardiogenesis (Hove et al., 2003).

The old adage “seeing is believing” is perhaps the best way to describe the underlying theme of this thesis. Understanding the effects of mechanical stimuli on dynamic biological processes requires proper imaging tools to visualize and analyze the interactions of complex three-dimensional (3D) intravital structures. A number of noninvasive techniques have been applied in biological and clinical research for in vivo diagnostics (McVeigh, 2006). While *in vivo* imaging techniques such as magnetic resonance imaging (MRI) and positron emission tomography (PET) can operate reasonably well in some instances, none of them can provide instantaneous velocity fields at an adequate spatial and temporal resolution to quantify highly dynamic processes such as microscale flows. Recent advances in confocal laser scanning microscopy (CLSM) provide a method to enable fast 3D imaging at various tissue depths in a sample volume by moving the objective lens along the depth direction. However, a fundamental limit of this technique is that a phase difference exists between images acquired at different depths due to the time delay. As a result, this technique is not optimal for acquisition and quantitative analysis of 3D motions of dynamic biological processes.

The motivation of the present research is to enhance the capability of understanding the effects of highly dynamic biomechanical forces on complex 3D living biological structures. Herein I describe a novel high-speed 3D microscopic imaging technique that is based on an optical defocusing concept, defocusing digital particle image velocimetry (DDPIV). This technique is able to resolve a particle’s depth location in a single planar image by matching the corresponding defocused image patterns of the particle generated by an aperture mask. Using this methodology, dynamic volumetric information can be acquired in real-time using a microscope equipped with a high-speed camera. The internal circulation existing within an evaporating water droplet is studied to demonstrate the capability of this approach. I then use the zebrafish (*Danio rerio*) as a living biological model to test my ability to follow the 3D dynamic motions within the developing cardiovascular system. Zebrafish are an ideal experimental model for this work as they are characterized by rapid development, small body size, external fertilization, and optical accessibility (Harvey and Rosenthal, 1999).

1.2 Thesis organization

Chapter 2 reviews the background in the literature for the presented research. I introduce the effects of biomechanical stimuli (especially blood-flow induced forces) on biological processes from the cellular scale (endothelial cells) to vertebrate organs, and in particular on heart development. I also provide some evidence that hemodynamics contribute to abnormal organ development and to other diseases. The advantages of using embryonic zebrafish as an animal model for this study as well as the morphological changes that occur during early heart development are explained. Principles and applications of in vivo imaging using current noninvasive imaging tools including MRI, PET, and ultrasound biomicroscopy (UBM)-Doppler are reviewed. 4D (3D plus time) confocal laser scanning microscopy techniques capable of 3D volumetric reconstructions of the zebrafish cardiovascular system are further described, as well as their limitations in quantitative imaging and mapping of 3D motions.

Chapter 3 describes the development of a novel 3D real-time imaging system, based on a micro DDPIV concept that provides quantitative information on microscale flows. The integration of the defocusing principle with a microscope is accomplished by attaching a mask with three pinhole apertures, forming an equilateral triangle, to the back of the objective lens. A point light source out of the focal plane will generate three defocusing images on the camera chip where their spatial separation is related to the point's distance from the focal plane. Unfortunately, the relative inaccessibility of several optical components of a microscope makes such a relationship difficult to establish. A calibration procedure modifies the original equation derived from geometrical analysis, and makes it more suitable for resolving the depth coordinate from microscopic images. Laser-induced fluorescence is used to enhance the brightness and contrast of the measuring volume. Defocusing image patterns are preprocessed prior to triangle matching to remove the background and noise generated by an image sensor. The measurable depth of the microscopic system is approximately 110 μm with fluorescent particles on a transparent cover glass. The depth resolution can reach sub-micron level with a sub-pixel detection algorithm. Finally, the measurement uncertainties using this technique have been fully determined and validated.

In chapter 4 I utilize the developed imaging modality to visualize the convective flow due to Marangoni effects inside a sessile evaporating droplet on a substrate. 2-μm fluorescent particles identical with the calibration targets are mixed with the droplet to serve as flow tracers. The reconstructed 3D coordinates of tracer particles are then fed into a computational statistics procedure called particle tracking velocimetry (PTV), which then find the velocity fields of internal circulations over time. The obtained velocity fields reveal fountain-like flow in the core region and vortex flow near the edge of the droplet. Additionally, the existence of vortex flow in all three planes is clearly visible in the reconstructed trajectories of the flow tracers. This cannot be seen in 2D visualization experiments but is consistent with computational results done by others.

Chapter 5 reveals the 3D motions of cardiac cells within the living embryonic zebrafish as determined by the micro DDPIV imaging system. A minimal invasive method is used to introduce fluorescent particles into the zebrafish heart via systematic circulation (caudal vein injection). Defocusing images are firstly processed by removing the non-uniform background component generated by particles trapped in surrounding static tissues. The flow field in the yolk sac is mapped, revealing a spherically-shaped flow pattern around the yolk. Blood flow over a few cardiac cycles in an early heart tube is measured; together with motions of two particles marking the atrial and the ventricular walls. Contractions and expansions of both heart chambers also are reconstructed with particles embedded in the heart wall. 3D endocardial strains in the ventricle are calculated based on the reconstructed coordinates of two such particles. Blood flows in the atrium and the ventricle are dynamic in nature with changing distributions of the flow fields during systole and diastole.

Chapter 6 summarizes the results of the present research. Remaining challenges of the newly developed imaging technique are discussed, as well as future work to enhance its application.

References:

Cartwright JHE, Piro O., Tuval I (2004) Fluid-dynamical basis of the embryonic development of left-right asymmetry in vertebrates. *Proc Natl Acad Sci USA* 101(19): 7234-7239.

Feldman CL, Ilegbusi OJ, Hu Z et al. (2002) Determination of in vivo velocity and endothelial shear stress patterns with phasic flow in human coronary arteries: a methodology to predict progression of coronary atherosclerosis. *Ameri Heart J* 143(6): 931-939.

Galbraith CG, Skalak R, Chien S (1998) Shear stress induces spatial reorganization of the endothelial cell cytoskeleton. *Cell Motil Cytoskeleton* 40:317–330.

Harvey RP, Rosenthal N (1999) *Heart Development*. Canada: Academic Press.

Hove JR, Köster R., Forouhar AS, Acevedo-Bolton G, Fraser SE, and Gharib M (2003) Intracardiac fluid forces are an essential epigenetic factor for embryonic cardiogenesis. *Nature* 421: 172-177.

Kramer-Zucker AG, Olale F, Haycraft CJ et al. (2005) Cilia-driven fluid flow in the zebrafish pronephros, brain and Kupffer's vesicle is required for normal organogenesis. *Develoment* 132(8): 1907-1921.

McVeigh ER (2006) Emerging imaging techniques. *Circ Res* 98:879-886.

Seki T, Yun JH, Oh SP (2003) Arterial endothelium-specific activin receptor-like kinase 1 expression suggests its role in arterialization and vascular remodeling. *Circ Res* 93(7): 682-689.

Chapter 2

Background: micromechanics, biomechanics in developmental biology, and imaging techniques

2.1 Introduction

Recently small systems at micron or submicron scales have been progressively developed for use in the biomedical and chemical fields. During fluid transport, mixing and flow-structure reactions commonly occur in such micro systems and are significant when contemplating the design and application of micro devices. Visualization and analysis of microscopic flow (e.g., velocity measurement) thus become critical needs. In addition, microfluid forces are essential in many biological behaviors from the swimming motions of sperms to the motions of motile bacteria. Currently, biofluid motions, and the forces they impose on surrounding cells, are thought to be key factors in the development, maintenance, and remodeling of intravital tissues in living systems. Understanding of the micro fluid phenomena in devices and biological systems both require direct quantitative analysis of the salient flow fields. Therefore quantitative visualization of microscopic flow is of great biological and fluid mechanical interest.

2.2 Microscale biomechanics

Intravital fluid flows recently have been broadly acknowledged to play a significant role in developmental biology owing to the biomechanical stimuli (i.e., transmural pressure and shear stress) they impose on adjacent cells or tissues. Blood is a complex biofluid consisting of many small molecules (i.e., proteins, nutrients and hormones) as well as larger cells (i.e., red and white blood cells, platelets). Among all biologically relevant fluids, blood exhibits the most intricate behavior. Blood as a whole acts chemically with its environment by transporting gases, waste products, and nutrients throughout the body after being pumped out of the heart. In addition to its chemical actions, blood reacts mechanically with the tissues it comes in contact with. At the same time the various components of whole blood react mechanically and chemically with one another. Biofluid flow-induced forces, in particular hemodynamic forces include: 1) wall shear stress, which is caused by blood moving near the vessel wall (Ling et al., 2002; Zamir et al. 2003); 2) transmural pressure exerted against the walls due to contraction and relaxation of muscles (Taber et al. 2001); 3) circumferential stretch resulting from the action of pressure as well as the shear stress (Helmlinger et al. 1991).

2.2.1 Effects of biofluid forces on endothelial cells

Endothelial cells (ECs), lining the vascular bed in the entire vertebrate body serve as a barrier between the intravascular blood and vascular wall, and are permeable to a number of bioactive molecules. ECs demonstrate a variety of behaviors involved in physiological function such as migration, regulation, secretion, remodeling, proliferation, and apoptosis. Chemical ligands are well known to stimulate and modulate the functions of ECs. In a similar manner, ECs also respond to mechanical stimuli such as shear stress and transmural pressure. Mechanotransduction is essentially a feedback mechanism whereby the ECs respond to external mechanical forces (e.g., those imposed by moving biofluids). Briefly, mechanical forces activate myriad mechanosensors in the ECs, which communicate within and between cells via a multitude of signaling pathways. Transcription factors may be activated as well, binding with promoters in a gene to regulate its expression. As a result, altered protein expression patterns lead to regulation of cellular functions.

The responses of ECs to shear stress are the best studied of all three types of mechanical forces. Shear stress, which acts parallel to the luminal surface of the vessel, is generated by the viscosity of the flowing fluid as well as the velocity gradient between adjacent fluid layers, particularly at the interface between the fluid and the vessel wall. Mechanotransduction in ECs in response to shear stress has been studied utilizing both in vitro and in vivo methods. Flow chambers are usually adopted as a model vascular system for in vitro study as experimental variables can be easily controlled in such an apparatus. ECs are cultured and grown on the inner surface of channels exposed to various flow environments generated by pressure pumps. Biomechanical engineers have utilized in vitro methods to show that the imposition of shear stress on ECs may activate many mechanosensors and transducers including the vascular endothelial growth factor (Wang et al. 2002), G proteins (Kuchan et al. 1994) and ion channels (Yamamoto et al. 2006). Furthermore, changes in gene expression patterns in response to shear stresses have been observed to regulate cell phenotypes. For examples, sustained laminar shear stress has been shown to result in a down-regulation of monocyte chemotactic protein-1 (MCP-1), reducing monocyte attraction to the vessel wall (Shyy et al. 1994). Lin et al. (2000) found that relatively long-term, steady shear stress inhibited the growth of ECs. Organization of cytoskeletal elements of ECs and morphology of cells are changed as a consequence of a sustained laminar shear stress (Garcia-Cardena et al. 2001). All these studies have proved that ECs respond actively with the imposition of shear stress.

In vitro studies mentioned above have contributed a great deal to our understanding of how ECs react to biomechanical forces as well as how flow regimes can regulate gene expression patterns. However, in vitro experiments are able to accurately reproduce neither the complex biological flows nor the interconnectivities of adjacent tissues in living systems. Further progress will likely be facilitated by in vivo studies of flow-cell interactions. Results from in vivo experiments have already begun to corroborate data collected in vitro. Examination of MCP-1 shows less localization of monocytes exists in where blood flow is laminar and steady, for instance near the most linear portions of the aorta (Chien 2003). Stress fibers of ECs in this segment of the aorta also show prominent orientation parallel to the direction of blood flow (Kim et al. 1989, Wong et al. 1983).

2.2.2 Effects of mechanical forces on vertebrate organs

The ability of ECs to sense and transduce experimentally induced biomechanical stimuli provides us with a number of options when studying the relationship between flow and structure. Genetic, pharmacological, or surgical manipulations that alter the local flow environment have been shown to profoundly influence morphological and functional phenotypes in developing vertebrate systems. Forces produced by intravital fluid flow appear to be critical to the proper development and maintenance of many aspects of biological form and function. This is particularly true during embryonic development where internally derived, flow-induced forces are thought to be key factors in a number of processes including: symmetry determination, blood vessel formation, glomerulogenesis, brain development, lung development, and cardiogenesis. Cartwright et al. (2004) found that fluid dynamics within the node of developing mouse embryos influenced the initiation of left-right body asymmetry (e.g., heart on the left of the body and liver on the right). Seki et al. (2003) observed that remodeling of blood vessel formation was regulated by changes in gene expression which were, in turn, affected by hemodynamic changes. Serluca et al. (2002) found that hemodynamic forces influenced endothelial signaling during kidney morphogenesis. Kramer-Zucker et al. (2005) extended this work and found a role for fluid flow on distension pathologies in both the kidney and brain. Mechanotransduction may even serve as a stimulus for apoptosis during lung remodeling (Del Riccio et al., 2004). The role of flow induced forces on cardiovascular development is perhaps the most intensely studied example of living flow/structure interaction and will be discussed in detail later.

In addition to their role during development, the biomechanical forces generated by intravital flow also are considered to be factors in the pathogenesis of a variety of diseases in the cardiovascular (Langille and Ojha, 1997; Feldman et al. 2002; Wasserman and Topper, 2004), nervous (Bateman, 2004; Chang and Nakagawa, 2004) and, renal (Nauli et al. 2003, Forman et al. 2005, Simons et al. 2005) systems as well.

2.2.3 Effects of mechanical forces on vertebrate heart development

Vertebrate heart development is an interesting process consisting of several well-defined structural and functional changes. Cardiogenesis involves growth (increase of organ mass), remodeling (changes in physical properties) and morphogenesis (changes in structure). Although proper structure and function of the heart is not required for survival in the zebrafish embryo, abnormalities in early vertebrate heart development often become life-threatening and are the leading causes of congenital birth defects (Olson et al. 1996). Therefore, the study of cardiogenesis is of enormous scientific interest in both the biological and medical research communities. The heart is a hollow, muscular, pumping organ and is one of the first organs to form in the developing vertebrate embryo. The contractile cycle of the heart can be divided into two phases. The first phase is called diastole, representing the time when blood fills the heart as well as a short period prior to filling during which the heart is relaxing. The second phase, systole, represents the time during which the heart muscle contracts and ejects blood from the heart. As in all vertebrate muscle, an electrical event precedes the mechanical contraction of the heart muscle. A brief delay in the conduction of these bioelectrical impulses from the atrium to the ventricle allows the atrium to contract first, squeezing blood into the ventricle. The heart wall is predominantly composed of muscle cells, which are tied together by a collagen network.

While many conditions have to be met to ensure proper cardiac development, genetic programming and biomechanical signaling are the two predominant focuses in the field of cardiovascular regulation. Fundamentally, the heart development is defined by genetic programming. The effects of mechanical forces on the developmental genetic program have become a topic of research focus due in large part to the availability of cardiac mutants. Hogers et al. (1997) found that abnormal intracardiac flow patterns may result in cardiac malformation in embryonic chicks. Hu et al. (2000) studied ventricular pressure changes in developing zebrafish heart. Besides flow-induced forces, other mechanical properties of tissue or muscle can also affect the development of cardiovascular systems. Zamir et al. (2003) studied the difference of stiffness between the concave inner curvature and the convex out curvature of embryonic chick heart tube, which contributes to cardiac looping during development. Berdougo et al. (2003) found a zebrafish mutant (*wea*) with atrium contractility defects had a profound influence on normal ventricular development, rendering a compact ventricle with thickened myocardium. Recent studies have revealed that the looping embryonic heart is capable of morphogenetic adaptation to changes in the mechanical environment (Nerurkar et al. 2006).

These studies clearly demonstrate that biomechanical forces have a profound impact on a variety of biological phenomena from the molecular to organismal level. In vitro studies of the mechanisms between external forces and biological responses are not able to provide accurate information due to the complexity of microscale living systems. An urgent need of further understanding of micromechanics has led biologists and bioengineers to seek proper in vivo quantitative imaging approaches.

2.3 A remarkable model for developmental biology-zebrafish

Model systems such as mice, chicks, and zebrafish have been used to study a variety of human hematopoietic and cardiovascular diseases. The zebrafish (*Danio rerio*) is an increasingly utilized vertebrate model for the study of normal and pathological cardiac development. Compared with mammals, this species is “half-hearted”, i.e., only one atrium and one ventricle in the heart. Despite this important structural difference, the development of embryonic zebrafish heart and early human heart is quite similar in a number of respects. The two-chamber heart is the first organ to form in early embryonic zebrafish. It starts periodic contraction at approximately 24 hours after fertilization (hpf), pumping blood into the high-resistance gill arches and then to the rest of the body via its systemic vascular network.

A few attractive features of this tiny vertebrate include short generation time, small body size, external fertilization, optical clarity, and genetic tractability. It takes approximately 5 days for an embryonic zebrafish heart to fully develop, and only 3 months for an embryo to become sexually mature. Its rapid development and small size at maturation (~ 4 cm) greatly reduces the time and space requirements for large-scale or multi-generational studies. External fertilization, combined with optical clarity at early embryonic stages allow for direct monitoring of cardiac development of normal and compromised fish.

In addition to the many life history characteristics that make the zebrafish a potential animal modle is the fact that its genome has been successfully sequenced and hundreds of valuable mutants have been produced. While many genetic tools are available for use with established models such as Drosophila and Xenopus, the accessibility of zebrafish to a variety of genomic methodologies throughout development has given rise to numerous cardiovascular phenotypes (Chen et al. 1996, Stainier et al. 1996). As a result, identifying and functionally characterizing zebrafish genes have been facilitated. In addition, many mutants resemble human cardiac malformation and malfunction, and even lethal mutants survive much longer than in other vertebrate models (North and Zon, 2003). Finally, mutants with transgenic genes expressing fluorescent proteins have been developed as well, producing added contrast at places of interest inside the body.

Accessibility to the inner workings of the embryonic zebrafish heart allows for more focused studies on the effects of biofluid dynamic flow/structure interactions and their underlying control. Occlusion of cardiovascular inflow or outflow has been shown to have a profound impact on heart looping and valve formation (Hove et al. 2003). The early embryonic heart tube is proven to drive the blood by a suction pumping mechanism (Forouhar et al. 2006). Taken in total, these factors favor modeling human cardiovascular diseases and even studying drug deliveries with the zebrafish model.

2.4 Zebrafish heart morphogenesis

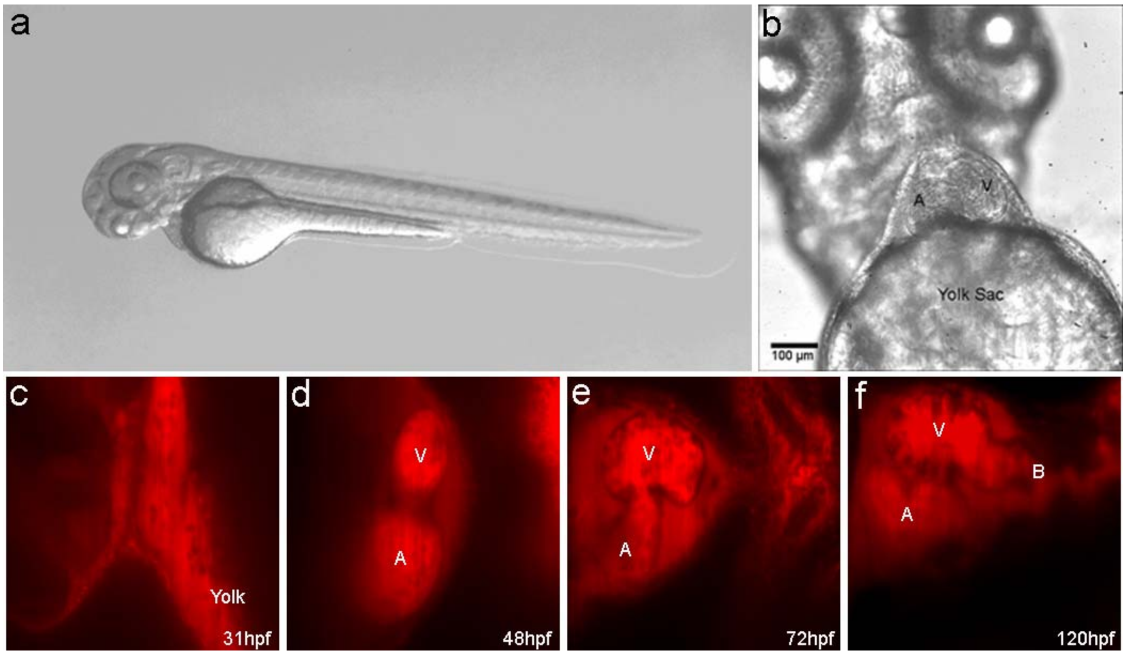

Figure 2.1. Zebrafish embryo and morphology changes during heart development. (a) A 48 hpf embryo is clearly observed by brightfield microscopy owing to its optical clarity. (b) In a higher magnification brightfield image of the heart, the atrium and the ventricle are prominent. (c, d, e, f) Morphological changes during rapid heart development are illustrated with images under a 40X objective lens acquired by confocal laser scanning microscopy. The embryonic heart has been fluorescently stained by BODIPY-ceramide (Molecular Probes). A: atrium; V: ventricle; B: bulbus arteriosus.

During zebrafish heart morphogenesis, the heart originates from progenitor cells, develops into a linear heart tube, and rapidly transforms into a dynamic two-chambered functioning organ (Fig. 2.1(c)-(f)).

Zebrafish heart development starts at 15 somite stage (16 hpf) when myocardial progenitor cells assemble into two primitive myocardial tubes. These tubes come together and fuse to form a cone-shaped heart tube deep to the brain by 22 hpf (Stainier et al., 1993), enclosing the endocardial progenitors in the process. This primitive heart tube consists of concentric rings of endocardium and myocardium separated by elastic cardiac jelly and is more dorsal than its later location. Myocardial contractions initiate at this stage (22 hpf) without apparent direction and do not effectively drive blood circulation. By 24 hpf, the heart initiates periodic contractions at the venous end, and blood circulation begins. The heart beat frequency steadily increases with time throughout development.

Subsequently, prominently distinct atrial and ventricular chambers form by 30 hpf. The linear heart tube begins to gradually loop to the right, adopting an intermediate “C” shape and then a more advanced “S” configuration, with the atrium being positioned to the left of the ventricle. The boundary between the two chambers forms the cardiac cushions by an epithelial to mesenchymal transition of ECs by 48hpf, where the future AV valve is located. Definite structures of four segments including sinus venosus, atrium, ventricle, and bulbus arteriosus are clearly defined (Hu et al., 2000).

By 5 dpf, functional bicuspid valves form between the atrium and the ventricle (AV), as well as between the ventricle and the bulbus (VB), preventing retrograde circulation through the heart. The ventricle develops to a densely trabeculated chamber while the atrium inner wall remains smooth. The embryonic zebrafish heart now has developed to its mature configuration and effectively drives blood circulation as an adult.

2.5 Current in vivo imaging techniques

2.5.1 Noninvasive images techniques

Visualizing blood flow and other dynamic motions within a living subject is challenging due to difficulties such as low light conditions and low contrast tissues. There are a number of noninvasive imaging techniques available for biological and clinical in vivo diagnostics of structure and function, including magnetic resonance imaging (MRI), nearinfrared fluorescence (NIR), X-ray computed tomography (CT), single photon emission computed tomography (SPECT), positron emission tomography (PET), and ultrasound biomicroscopy (UBM)-Doppler. Important characteristics of a useful in vivo imaging technique include high spatial resolution, temporal resolution, detection sensitivity, signal-to-noise ratio, quantitative accuracy, and minimal risk of damage to the tissue, as well as cost and throughput. Several different imaging modalities are currently used because while they may operate excellently in some applications, they are often very poorly suited for others. For example, a “perfect” imaging instrument one would imagine should have the spatial resolution of MRI, the temporal resolution of ultrasound, and the sensitivity of PET.

Some of these approaches have been broadly applied. The principle of MRI is based on the alteration of unpaired atoms by a radio frequency pulse, resulting in magnetic contrast in tissues with very high spatial resolution. MRI has been practically used in studying structure of brain and cardiovascular systems, as well as human blood flow (Hata et al. 2005, Alperin et al. 2005). Decay of injected nuclei in living subjects emit positrons interacting with free electrons. The energy of the interaction is detected by PET in the form of gamma ray. Hemodynamic influences in the human body have also been measured by PET (Oku et al. 2005). Ultrasound imaging is achieved by scanning of organisms with ultrasound waves in the 20 MHz to 60 MHz range and detection of the resulting wave reflections. UBM-Doppler has proven to be effectively quantifying blood flow in mouse embryos (Turnbull 1999).

Characteristics of in vivo biomechanical behaviors such as highly dynamic motion and complex three-dimensional (3D) structure bring additional difficulties to quantitative imaging. A common method of acquiring 3D geometry is to take a series of planar images along the third dimension and to reconstruct the 3D volume via a proper post assembly of the image sections. Recent advances in developing high-speed CCD or CMOS image sensors provide a solution to adequately describe highly dynamic motions by sequentially collecting images over time. The short interval between two successive images (e.g., temporal resolution) enables access to time-dependent information on the motions. While *in vivo* imaging techniques are able to operate reasonably well in some instances, none of them is able to obtain instantaneous 3D velocity fields at an adequate spatial and temporal resolution.

2.5.2 4D (3D + time) confocal laser scanning microscopy

Confocal laser scanning microscopy (CLSM) has emerged as a popular approach in planar imaging of biological systems, especially the ones that are fluorescently labeled. The principle of CLSM is to place a pinhole in front of the conjugate image plane of a conventional optical microscope, before the image detector. Ray tracing of the microscopic system reveals that light from places out of the focal plane is blocked by the pinhole. As a result, only signals from the focal plane are detected greatly enhancing the axial resolution of the acquired image.

Remarkable advances recently have been made in acquiring high-speed 3D data through confocal microscopy. Liebling et al. (2005) took advantage of CLSM to reconstruct dynamic 3D volume of living biological systems by consecutively scanning the volumetric structures rapidly from one spatial slice to another through the use of a periodically moving objective lens and synchronizing successive optical sections. Motions of the beating embryonic zebrafish heart were recorded and analyzed using this technique. Traditional point laser beam confocal systems collects images in a pixel by pixel manner, limiting the speed of data collection (<10 frames per second). In Liebling's system, a blade-shaped laser beam was used with a fast CCD line detector to allow for parallel acquisition of an entire line of pixels. As a result, the acquisition speed of the imaging system was greatly enhanced (151 Hz at 256×256 pixel^2 resolution) with even high speeds attainable if spatial resolution is compromised by scanning fewer lines of pixels. Image sequences describing volumetric information were collected by the objective lens moving at a predefined depth. Because of the temporal difference between two consecutive images, assembly of the slices for 3D volumetric reconstruction was performed by a postacquisition synchronization procedure to correctly adjust the spatial shift.

Despite the success of this experimental approach, there are three fundamental limitations: (i) 3D volume can be correctly recovered only if the dynamic motion is periodic (such as heart beat). Synchronization of slice-sequence pairs, the core procedure to reconstruct 3D volume, requires periodic boundary conditions to maximize the similarity between two adjacent slices. Consequently the dynamic motions being imaged have to be periodic as well. Therefore not all possible motions in living biological systems can be imaged using this technique. (ii) The scanning rate of a CLSM system is limited to 151 frames per second with a full resolution at 256x256 pixel^2. While the technique is successfully applied to some in vivo dynamic processes (e.g., cell migration, heart-wall motions, etc.), it may not be capable of providing sufficient speed or spatial resolution to study other important intravital motions. (iii) This resulting reconstruction does not provide real-time information of motions within this volume. As the two adjacent slices were scanned at different time, cells that were imaged in the first optical slice may not be present in the second slice due to the time delay between imaging the two slices. The recovered 3D structure can only provide qualitative information of how cells move. And quantitative analysis of cell motions, such as velocity measurements of blood flow and moving organs, is not accessible using this technique owing to the lack of real-time motion information.

As a result, the recent CLSM imaging system cannot be applied effectively for quantitative dynamic motions imaging and mapping. The goal of the present research is to develop a proper 3D imaging modality capable of quantitative diagnostics of highly dynamic time-dependent motions in living animal organs as well as other complex microscale systems.

References:

Alperin N, Lee SH, Sivaramakrishnan A, and Hushek SG (2005) Quantifying the effect of posture on intracranial physiology in humans by MRI flow studies, *J Magn Reson Imaging* 22(5), 591-596.

Bateman GA (2004). The role of altered impedance in the pathophysiology of normal pressure hydrocephalus, Alzheimer’s disease and syringomyelia. *Medic Hypo* 63(6): 980-985.

Berdougo E, Coleman H, Lee DH et al. (2003) Mutation of *weak atrium/atrial myosin heavy chain* disrupts atrial function and influences ventricular morphogenesis in zebrafish. *Development* 130(24): 6121-6129.

Cartwright JHE, Piro O., Tuval I (2004) Fluid-dynamical basis of the embryonic development of left-right asymmetry in vertebrates. *Proc Natl Acad Sci USA* 101(19): 7234-7239.

Chang HS and Nakagawa H (2004) Theoretical analysis of the pathophysiology of syringomyelia associated with adhesive arachnoiditis. *J Neurol Neurosury & Psychi* 75(5): 754-757.

Chen JN, van Eeden FJM, Warren KS, Chin A, Nusslein-Volhard C, Haffter P and Fishman MC (1997) Left-right pattern of cardiac BMP4 may drive asymmetry of the heart in zebrafish. *Development* 124: 4373-4382.

Chien S (2003) Molecular and mechanical bases of focal lipid accumulation in arterial wall. *Prog Biophys Mol Biol* 83: 131–151.

Del Riccio V, van Tuyl M, Post M (2004) Apoptosis in lung development and neonatal lung injury. *Pediatc Res* 55: 183-189.

Feldman CL, Ilegbusi OJ, Hu Z et al. (2002) Determination of in vivo velocity and endothelial shear stress patterns with phasic flow in human coronary arteries: a methodology to predict progression of coronary atherosclerosis. *Ameri Heart J* 143(6): 931-939.

Forman JR, Qamar S, Paci E et al. (2005) The remarkable mechanical strength of polycystin-1 supports a direct role in mechanotransduction. *J Mol Biol* 349(4): 861-871.

Forouhar AS, Liebling M, Hickerson AI, Naisrei-Moghaddam A, Tsai HJ, Hove JR, Fraser SE, Dickinson ME, Gharib M (2006) The embryonic vertebrate heart tube is a dynamic suction pump. *Science* 312: 751-753.

Garcia-Cardena G, Comander J, Anderson KR, Blackman BR, Gimbrone MA (2001) Biomechanical activation of vascular endothelium as a determinant of its functional phenotype. *Proc Natl Acad Sci USA* 98: 4478-4485.

Hata N, Wada T, Kashima K, Okada Y, Unno N, Kitagawa M, and Chiba T (2005) Non-gated fetal MRI of umbilical blood flow in an acardiac twin. *Pediatr Radiol* 35(8): 826-829.

Helmlinger G, Geiger RV, Schreck S, Nerem RM (1991) Effects of pulsatile flow on cultured vascular endothelial cell morphology. *J Biomech Eng* 113:123– 131.

Hogers B, DeRuiter MC, Gittenberger-de Groot AC et al. (1997) Unilateral vitelline vein ligation alters intracardiac blood flow patterns and morphogenesis in the chick embryo. *Circ Res* 80: 473-481.

Hove JR, Köster R., Forouhar AS, Acevedo-Bolton G, Fraser SE, and Gharib M (2003) Intracardiac fluid forces are an essential epigenetic factor for embryonic cardiogenesis. *Nature* 421: 172-177.

Hu N, Sedmera D, Yost J. et al. (2000) Structure and function of the developing zebrafish heart. *Anat Record* 260: 148-157.

Kim DW, Langille BL, Wong MK, Gotlieb AI (1989) Patterns of endothelial microfilament distribution in the rabbit aorta in situ. *Circ Res* 64: 21–31.

Kramer-Zucker AG, Olale F, Haycraft CJ et al. (2005) Cilia-driven fluid flow in the zebrafish pronephros, brain and Kupffer’s vesicle is required for normal organogenesis. *Develoment* 132(8): 1907-1921.

Kuchan MJ, Jo H, Frangos JA (1994) Role of G proteins in shear stressmediated nitric oxide production by endothelial cells. *Am J Physiol Cell Physiol* 267: C753–C758.

Langille BL and Ojha M (1997) Blood flow dynamics, atherosclerosis and bypass graft failure. *Trends in Cardiovas Med* 7(4): 111-118.

Liebling M, Forouhar AS, Gharib M, Fraser SE, and Dickinson ME (2005) Four-dimensional cardiac imaging in living embryos via postacquisition synchronization of nongated slice sequences. *J Biomed Opt* 10(5), 54001-54010.

Lin K, Hsu PP, Chen BP, Yuan S, Usami S, Shyy JY, Li YS, Chien S (2000) Molecular mechanism of endothelial growth arrest by laminar shear stress. *Proc Natl Acad Sci USA* 97: 9385–9389.

Ling P, Taber LA, Humphrey JD (2002) Approach to quantify the mechanical behavior of the intact embryonic chick heart. *Ann Biomed Eng* 30:636–645.

Nauli SM, Alenghat FJ, Luo Y et al. (2003) Polycystins 1 and 2 mediate mechanotransduction in the primary cilium of kidney cells. *Nat Gene* 33(2): 129-137.

Nerurkar NL, Ramasubramanian A, Taber LA (2006) Morphogenetic adaptation of the looping embryonic heart to altered mechanical loads. *Dev Dyn* 235: 1822-1829.

North TE and Zon LI (2003) Modeling human hematopoietic and cardiovascular diseases in zebrafish. *Dev Dyn* 228:568-583.

Oku N, Kitagawa K, Imaizumi M, Takasawa M, Piao R et al. (2005) Hemodynamic influences of losartan on the brain in hypertensive patients. *Hypertens Res* 28(1), 43-49.

Olson EN and Srivastava D (1996) Molecular pathways controlling heart development. *Science* 272: 671-676.

Seki T, Yun JH, Oh SP (2003) Arterial endothelium-specific activin receptor-like kinase 1 expression suggests its role in arterialization and vascular remodeling. *Circ Res* 93(7): 682-689.

Serluca FC, Drummond IA, Fishman MC (2002) Endothelial signaling in kidney morphogenesis: a role for hemodynamic forces. *Current Biology* 12(6): 492-497.

Shyy YJ, Hsieh HJ, Usami S, Chien S (1994) Fluid shear stress induces a biphasic response of human monocyte chemotactic protein 1 gene expression in vascular endothelium. *Proc Natl Acad Sci USA* 91: 4678–4682.

Simons M, Gloy J, Ganner A et al. (2005) Inversin, the gene product mutated in nephronophthisis type II, functions as a molecular switch between Wnt signaling pathways. *Nat Gene* 37(5): 537-543.

Stanier DYR, Lee RK, Fishman MC (1993) Cardiovascular development in the zebrafish I. Myocardial fate map and heart tube formation. *Development* 110:31-40.

Stanier DYR, Fouquet B, Chen J, Warren KS, Weinstein BM et al. (1996) Mutations affecting the formation and function of the cardiovascular system in the zebrafish embryo. *Development* 123: 285-292.

Taber LA (2001) Biomechanics of cardiovascular development. *Annu Rev Biomed Eng* 3:1–25.

Turnbull DH (1999) In utero ultrasound backscatter microscopy of early stage mouse embryos. *Comput Med Imaging Graph* 23:25–31.

Wang Y, Miao H, Li S, Chen KD, Li YS et al. (2002) Interplay between integrins and FLK-1 in shear stress-induced signaling. *Am J Physiol Cell Physiol* 283: C1540–C1547.

Wasserman SM and Topper JN (2004). Adaptation of the endothelium to fluid flow: in vitro analyses of gene expression and in vivo implications. *Vascular Medicine* 9(1): 35-45.

Wong AJ, Pollard TD, Herman IM (1983) Actin filament stress fibers in vascular endothelial cells in vivo. *Science* 219: 867–869.

Yamamoto K, Sokabe T, Matsumoto T, Yoshimura K, Shibata M et al. (2006) Impaired flow-dependent control of vascular tone and remodeling in P2X4-deficient mice. *Nat Med* 12: 133–137.

Zamir EA, Srinivasan V, Perucchio R, Taber LA (2003) Mechanical asymmetry in the embryonic chick heart during looping. *Ann Biomed Eng* 31:1327–1336.

Chapter 3

Microscale 3D flow mapping with µDDPIV*

---

* This chapter is adapted from Pereira F, Lu J, Graff E, and Gharib M. “Microscale 3D flow mapping with µDDPIV” Experiments in Fluids (2007) 42: 589-599. Some paragraphs have been modified.

3.1 Introduction to micro PIV/PTV

Quantitative visualization of microscale flow is of great biological and fluid mechanical interest. Particle image velocimetry (PIV) and particle tracking velocimetry (PTV) are essential tools for quantitative flow mapping. Relatively small seeding particles to the flow field are employed to represent features of the flow in both visualization methods. In general, images of particle moving within a defined flow field are recorded over a short time interval by a high-speed camera. Velocity vectors of the field are measured through two consecutive images, by dividing the displacement of particles in the first image frame relative to the particles in the second one by the time interval between the images. Given high particle intensity and/or a small displacement gradient across the image field, PIV is optimally applied to calculate the displacements through the use of a statistical evaluation scheme called cross correlation. A small interrogation window containing a group of particles in the flow field in the first image is correlated with various sections around the same position in the second image until the maximum correlation value of image intensity is obtained, where is the most probable spatial shift of the particle pattern. On the other hand, if the seeding particles are sparsely distributed in the flow field, (i.e., the distance between two neighboring particles is larger than the displacement), Particle tracking velocimetry would be the preferred algorithm of determining velocity field by tracking movements of individual particles. Instead of cross-correlating the grey level of two consecutive images in PIV, PTV requires a preprocessing step which determinates the spatial coordinates of every particle image. The tracking of an individual particle from one image frame to the next one includes three principal procedures: select a search volume in the second image frame where exists a small amount of matchable candidate particles, define a neighborhood radius for the search volume within which the displacement field is highly correlated, and apply suitable tracking schemes to select the most likely matched link.

Microscale particle image velocimetry (micro PIV, Santiago et al., 1998) and microscale particle tracking velocimetry (micro PTV, Suzuki et al., 2003) have been developed to measure velocity fields in microscopic fluid flow based on their successful application in macroscale flow. Hove et al. (2003) implemented micro PIV to measure the velocity and shear stress fields of in vivo cardiovascular blood flow in embryonic zebrafish.

Micro PIV/PTV systems have been well applied but are limited to two-dimensional measurements. However, many microscale fluid flows have three-dimensional characteristics, thus requiring volumetric quantitative imaging techniques to capture the flow 3D features. Holographic PIV (Pu et al., 2000), stereoscopic PIV and defocusing DPIV (Pereira and Gharib, 2002), are commonly used in three-dimensional macroscale flow mapping. Recently, a lot of efforts have been made to measure three-dimensional microscale flow fields. Following closely the experimental layout used for macroscale stereoscopic PIV, Bown et al. (2005) developed a stereoscopic micro-PIV system based on stereomicroscopy. In this work, a stereomicroscope with two cameras was utilized. Particle images from two different angles were captured simultaneously by the cameras. Vector fields of images from each angle were then obtained by the 2D PIV method. Three dimensional velocity vectors were calculated by recombining the two vector fields from different angles. Since microscale flow measurement was achieved with the aid of a microscope, other image techniques of microscopy were applied to enable three-dimensional particle imaging. Wu et al. (2005) took advantage of the three-dimensional diffraction ring patterns of small tracer particles when out of focus to track 3D particle motions. Defocusing position of a particle was resolved by calculating radius of the outmost ring. The three-dimensional trajectories of swimming E. coli were obtained using this technique.

In the present paper, a microscale three-dimensional flow diagnostic system was developed based on the defocusing DPIV technique (DDPIV). The principle of the technique was initially described by Willert and Gharib (1992). Later work by Pereira et al. (2000, 2002) enhanced the DDPIV concept and introduced an imaging system to map 3D two-phase flow fields. The DDPIV approach is the natural extension of in-plane DPIV to the third spatial dimension. Unlike other three-dimensional imaging techniques, such as photogrammetry and holography, the optical arrangement in a DDPIV system has a single optical axis. This conveys a number of unique advantages such as use of out-of-the-shelf components, compactness of the instrument and versatility. DDPIV holds many analogies with a standard 2D imaging system, where the light scattered by a point source is collected through a converging lens and a single aperture, located usually on the lens axis. In contrast, the DDPIV technique uses a mask with a multiplicity of apertures, arranged in a predefined pattern, to obtain multiple images from each scattering source. These images form the same geometrical figure on the image plane, but scaled according to the depth location of the scattering source. Hence, the particle's three-dimensional location can be determined, through simple ray optics relationships, by measuring the centroid and size of the pattern on the image plane. DDPIV maps instantaneously a given volume of interest and provides sets of particles quantitatively located in the physical space. If such particle sets are recorded in time, it is then possible to reconstruct their time evolution in space in a Lagrangian manner and derive their individual displacement and velocity, following the particle tracking methodologies described in Pereira et al. (2006).

The DDPIV principle is here applied for use with an inverted microscope, with the multiple pinhole aperture implemented into the microscope objective. The same idea has been put into practice in a recent and independent work by Yoon and Kim (2006), who captured the 3D flow field over a backward-facing step in a 50-μm deep micro-channel. The concept is not original in essence, since the implementation of a mask with multiple apertures into a single lens for the specific purpose of fluid diagnostics has been initially proposed by Willert and Gharib (1992). It implicitly extends to all sorts of lenses, including a microscope objective. However, and despite they being conceptually identical, the system proposed here and that described by Yoon and Kim (2006) differ at their core in the way the system is calibrated. The central issue with implementing the defocusing principle in a microscope resides in the complexity of the optical path and in the fact that the optical specifications of the objectives used therein are generally not accessible. Aware of this, Yoon and Kim (2006) describe a calibration-based method where calibration curves are constructed that link the size of the multiple-image pattern to the depth location, hence departing from the geometrical optics analysis typical of traditional DDPIV. Furthermore, their work does not provide any sort of uncertainty analysis that would help characterize a general microscopic defocusing system.

In this paper, we propose an alternate approach to the calibration problem that preserves the integrity of the DDPIV framework. An original calibration methodology is laid out where the optical characteristics of the system are derived in order to enable the use of the standard DDPIV analysis, as in a macroscale DDPIV apparatus. This allows us to apply the uncertainty analysis introduced by Pereira and Gharib (2002) and further extended by Kajitani and Dabiri (2005). We describe the technique, with a special emphasis on the calibration procedure and measurement uncertainty.

3.2 Experimental setup

A schematic of the experimental setup is shown in Fig. 3.1. The optical system consists of a microscope, a three-pinhole aperture mask, an argon ion laser and a high speed CCD camera. An inverted microscope (Nikon™, Eclipse TE2000-S) was utilized to implement the defocusing technique. An aperture mask with three pinholes forming an equilateral triangle was attached to the back of a 20X objective lens (Nikon™ Plan Apo, NA =0.75). The diameter of the pinholes is 2 mm and the separation between each two pinholes is 7 mm. In a conventional DDPIV system, only the distance between tracer particles and lens plane is allowed to change. Since any adjustment of the focus of the inverted microscope would have caused a change of the distance between the lens plane and the image plane, the focal knob has been locked during the performance of the measurements. Thus, the built-in horizontal stage on the microscope was replaced by a vertically mounted 1-μm resolution stage to allow adjustment along the axial direction (**Z**). Bright field microscopy was initially adopted in the measurement. However, strong reflections were caused by the sample surface, consequently hindering the particle detection because of the poorly contrasted images. Therefore, fluorescence microscopy, which is broadly used for biological imaging and small scale fluid visualization, was chosen to perform the experiments. We chose 2 μm yellow-green fluorescent microspheres (Molecular Probes™, FluoSpheres) as the flow markers. We used the 488 nm spectral line of a 5W argon-ion laser to excite the microspheres, the emission being 515 nm. The illumination of the measurement domain was done through the optical path normally used for regular bright field imaging. Time series of defocused images were recorded using a high speed CCD camera with 512x384 pixel^2 resolution (Kodak™ EktaPro Motion Analyzer, Model 1000HRC). The frame rate was 250 frames per second.

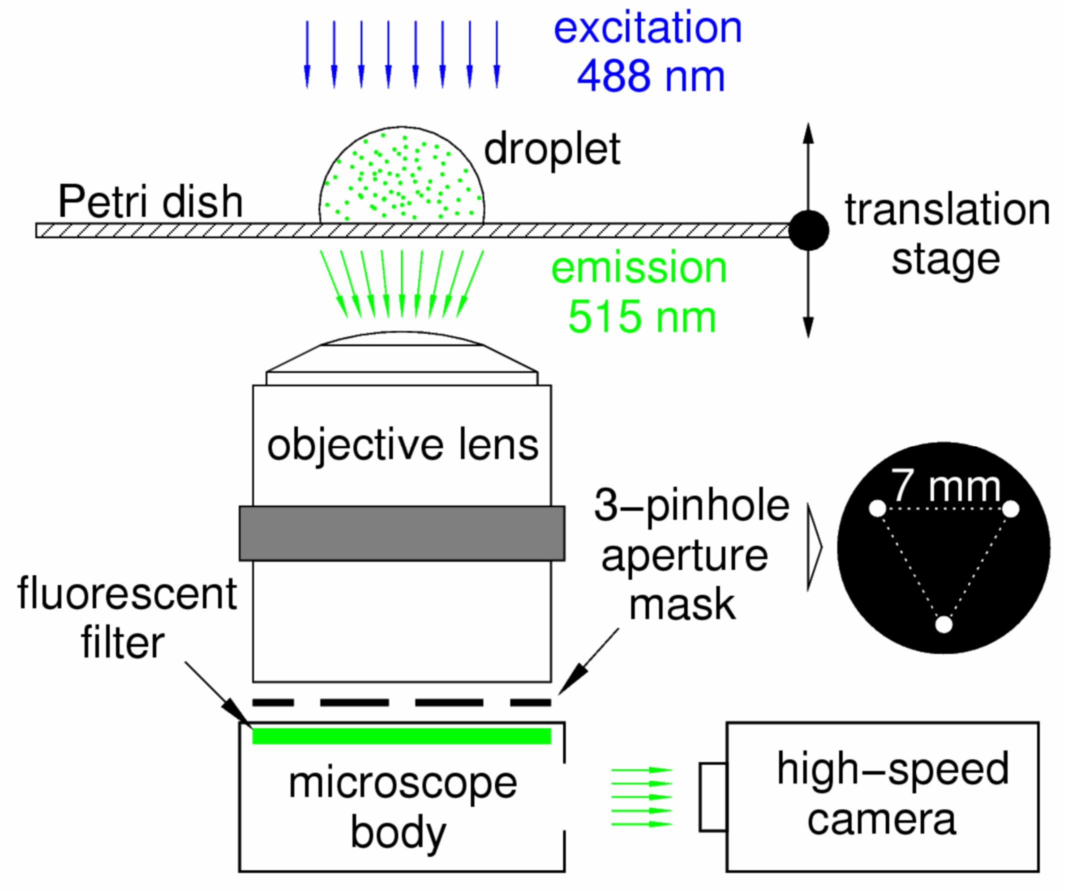

Figure 3.1. Schematic of μ-DDPIV experimental setup.

3.3 Calibration

3.3.1 Principle

Fig. 3.2 shows a schematic of a DDPIV optical configuration, composed of only two apertures for clarity of explanation. Let the coordinates of the system be (**X, Y, Z**), with the **Z**-axis corresponding to the optical axis. A point **A** out of the focal plane focuses on a point **B** beyond the image plane and, because of the off-axis apertures separated by the distance **d**, generates two images **A'** and **A"** on the image plane, separated by the distance **b**. If point **A** is moved to the focal plane, the two images coincide on the image plane with **b=0**.

Geometrical analysis was utilized in Pereira et al. (2002) to determine the relationship between the depth coordinate **Z** and the separation **b** between the multiplicity of defocused images of a given particle. This approach requires knowledge of parameters such as the distance **L** between the reference plane (or focal plane) and the aperture plane, the mean separation **d** between pinholes in the aperture mask and the focal length **f**. The latter parameter is also related to the objective magnification **M** by the lens formula: $\mathbf{f} = \mathbf{ML/(1+M)}$.

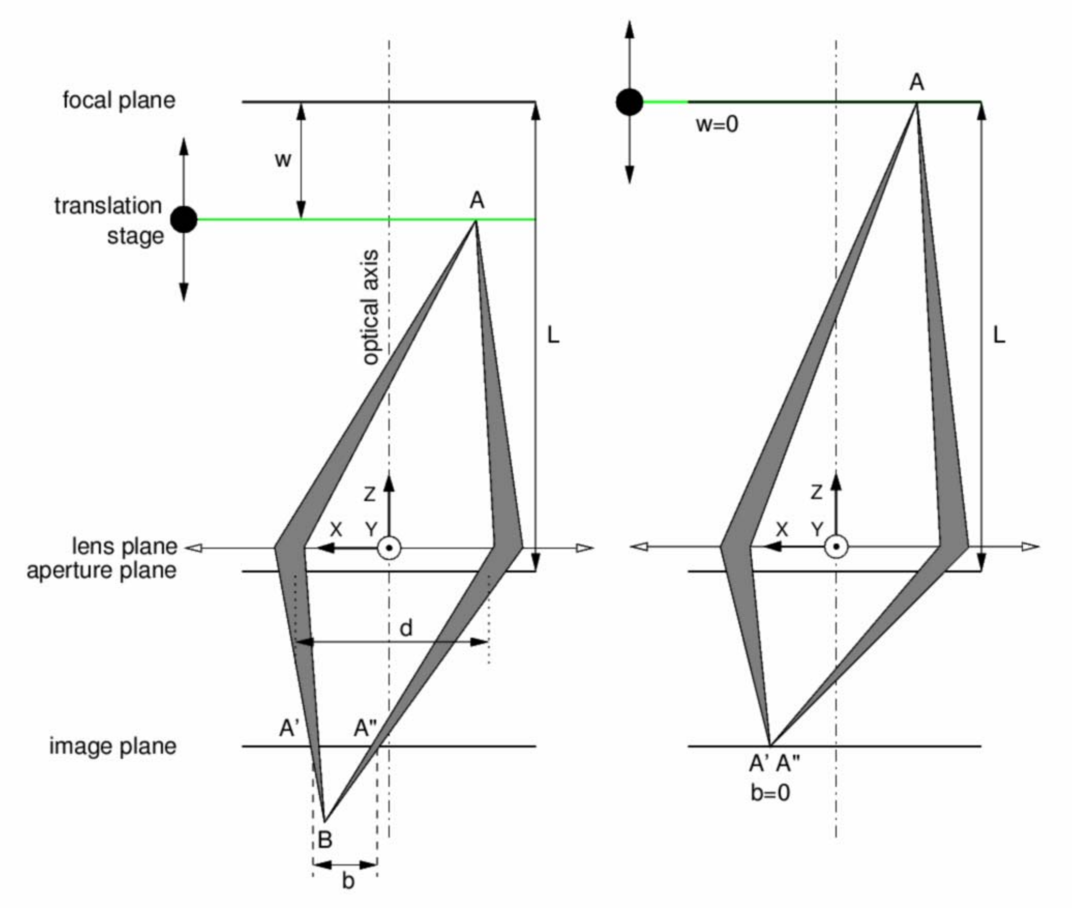

Figure 3.2. DDPIV optical schematic

However, for a microscope-based system, the actual optical properties of the objective lens are not generally accessible. In addition, the axial position of the objective optical center, and therefore of the aperture plane, cannot be explicitly measured in absolute terms. For these reasons, the standard DDPIV geometrical analysis, as outlined in the previous works, is not readily applicable for the μ-DDPIV system proposed here.

However, it is possible to determine the unknown parameters through calibration. Indeed, the separation **b** is related to the depth coordinate **Z** by the following relation (see Pereira et al., 2002):

$$\mathbf{b} = \mathbf{MdL}\left(\frac{\mathbf{1}}{\mathbf{Z}} - \frac{\mathbf{1}}{\mathbf{L}}\right) \tag{3.1}$$

M and **d** are known parameters of the optical system: **M** is given by the objective prescription and **d** is a design characteristic of the aperture mounted into the objective. Hence, we shall rewrite Eq. 3.1 in the following form:

$$\mathbf{L} = \mathbf{Z}\left(\frac{\mathbf{b}}{\mathbf{Md}} + \mathbf{1}\right) \tag{3.2}$$

M and **d** being known, a measure of **b** at a known position **Z** would suffice to determine **L**, which does not depend on **Z** or on any optical parameter. However, as we pointed out before, the absolute position of the lens optical center is not known a priori, thus **Z** is also unknown in absolute terms. Let **Z=L-w**, where **w** is the relative distance of a given point

A to the reference plane (see Fig. 3.2). From Eq. 3.2 we can then express **L** as a function of **w**:

$$\mathbf{L} = \mathbf{w}\left(\frac{\mathbf{Md}}{\mathbf{b}} + \mathbf{1}\right) \text{ with } \mathbf{w} = \mathbf{L} - \mathbf{Z} \text{ and } \mathbf{Z} < \mathbf{L} \qquad 3.3$$

Hence, the problem is now reduced to the determination of the actual origin for **w**. This origin shall define the location of the reference plane. Although **L** is unknown, the reference plane can be practicably located if one uses a target composed of a transparent plate with marker particles and translates it, by means of a precise translation device (see Fig. 3.2), along the **Z**-axis until the **b** separation is cancelled (**b=0**). This particular position corresponds also to **w=0**. Fig. 3.3 shows typical triple images of particles (or DDPIV images) obtained with our 3-aperture microscopic setup (Fig. 3.1) for three different values of **w**. Setting the precision positioning system for any value of **w** such that $\mathbf{w} > \mathbf{0}$, and consequently measuring the separation **b**, automatically defines **L** through Eq. 3.3. Once **L** is determined, one can calculate the focal length by simply using the lens formula. The optical system is then fully characterized and the standard DDPIV formulas can be applied normally.

We shall stress out that this procedure should be performed from a statistical standpoint, hence a large number of measurements are recommended to obtain statistically representative estimates. This can be done by performing measurements across the observation volume. In addition, the optical parameters **L** and **f** are only approximate values that do not necessarily match the actual characteristics of the single optical elements of the microscope optics, such as the objective focal length. However, they allow reducing the whole microscopic setup to an equivalent single lens system, suitable to apply the DDPIV conceptual approach.

In practice, a two-aperture mask introduces ambiguities since the line pattern has no privileged orientation. For instance, two particles (**C** and **D**) aligned parallel to the line connecting the two apertures in the mask will generate two defocused image pairs (**C'-C"** and **D'-D"**) aligned in a straight line. However, matching the four defocused images produces six possible image pairs (i.e., **C'-C"**, **D'-D"**, **C'-D'**, **C"-D"**, **C'-D"**, and **C"-D'**). Hence there is high probability to mismatch the defocused images and to generate particles that never exist. For this reason, a mask with three apertures forming an equilateral triangle was adopted (Fig 3.1), in which case the resulting triple-image pattern of a particle can be unambiguously identified (Fig 3.3).

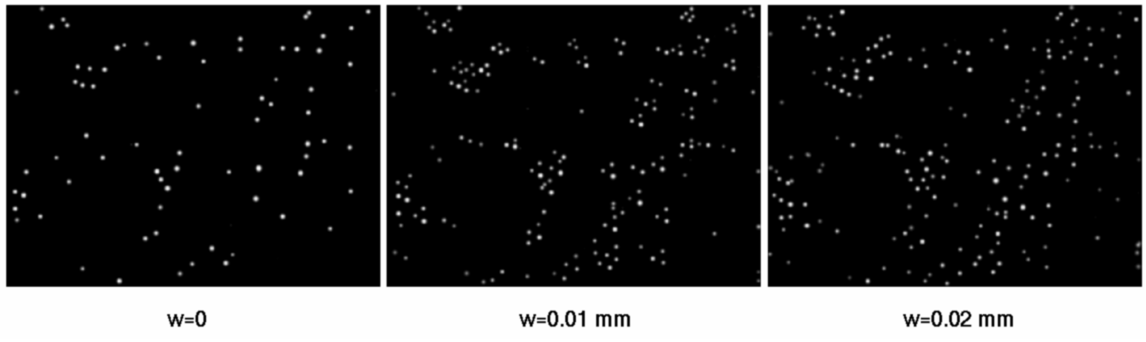

Figure 3.3. DDPIV images as a function of w

3.3.2 Experimental procedure

To perform the calibration, we used the 2 μm fluorescent microspheres as the calibration targets. It is known that diffraction and spherical aberration in microscopic imaging may cause distortion of defocused images (Inoué and Spring, 1997). Therefore we used a few targets spread over the whole field of view to calibrate the defocusing instrument. To manage this micro-target setup, we diluted the fluorescent particles into de-ionized water and put one droplet of diluted solution onto a plastic Petri dish (see Fig. 3.1). After a few minutes, water would evaporate completely and particles would dry mount on the plate. The mounted particles were then placed under the microscope and defocused by moving the translation stage. Defocused images of particles located at different distances **w** away from the focal plane were captured by the camera. The Petri disk was moved in one direction starting from the reference plane (**Z=L**, **w=0**), where the defocused images overlap (separation **b=0**), up to a point of maximum separation where detection was not possible. The target was moved in steps of 10 μm starting from the reference plane, totaling a depth range of 110 μm.

Fig. 3.4 describes the image processing performed prior to the triangle pattern matching (see Pereira et al., 2002). In particular, the high-speed camera uses a CCD sensor split into 16 areas, each 64x196 pixels. Each area has a separate gain amplifier, causing the image to show a non-uniform background. We recorded an image of this background in darkness conditions. The resulting image, shown in Fig. 3.4, is then subtracted from the particle image. Further processing includes lowpass filtering, particle subpixel detection, particle 2D Gaussian modeling and noise particle removal. This latter operation filters out the particles based on their image size.

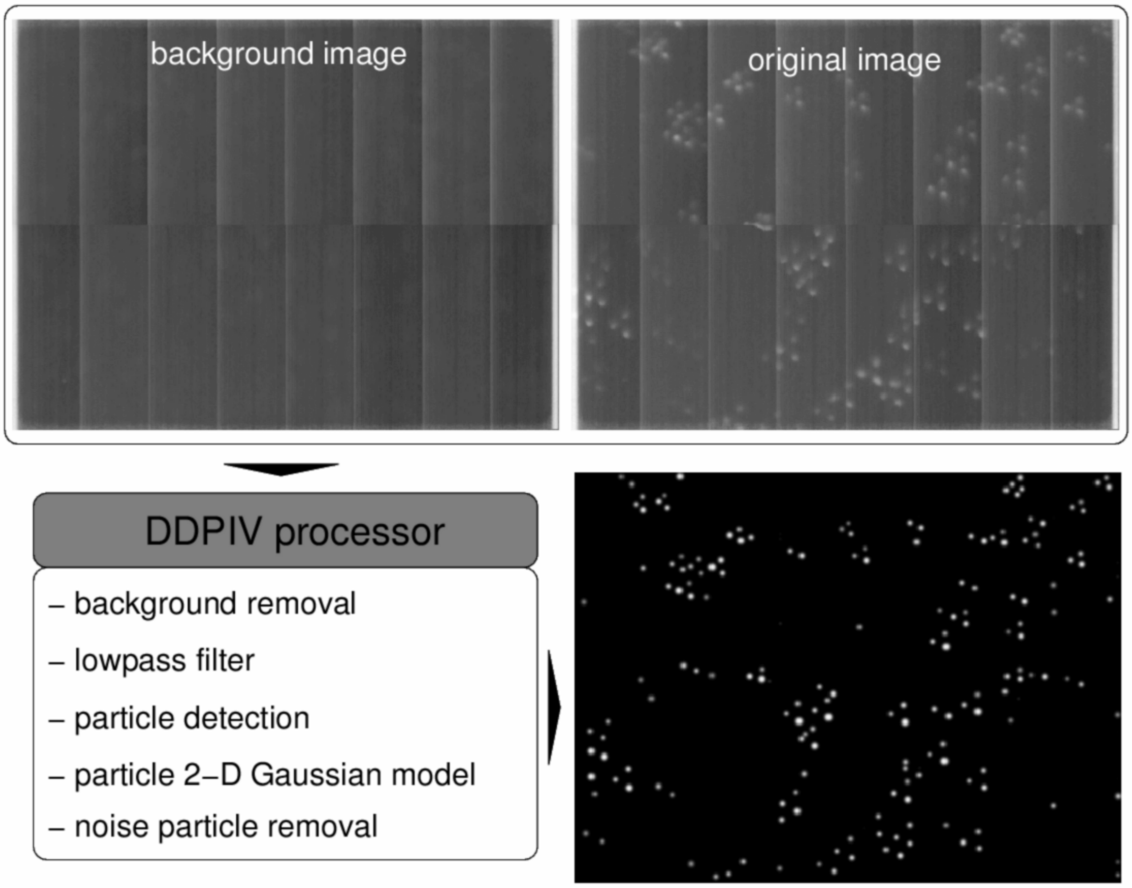

Figure 3.4. Image processing procedures (background and original images are enhanced for display).

3.3.3 Results

For each position **w** of the target plate, we calculate the mean and corresponding root mean square error. These two quantities are reported in Fig. 3.5. Since **b** is zero for **w**=0, no (or very limited) information is available at the starting **Z** position. Sample triangle images are shown to illustrate the increasing pattern size as **w** is increased. The pattern is reduced to a point when **w=0**. The depth range of the current μ-DDPIV system is found to be approximately 110 μm.

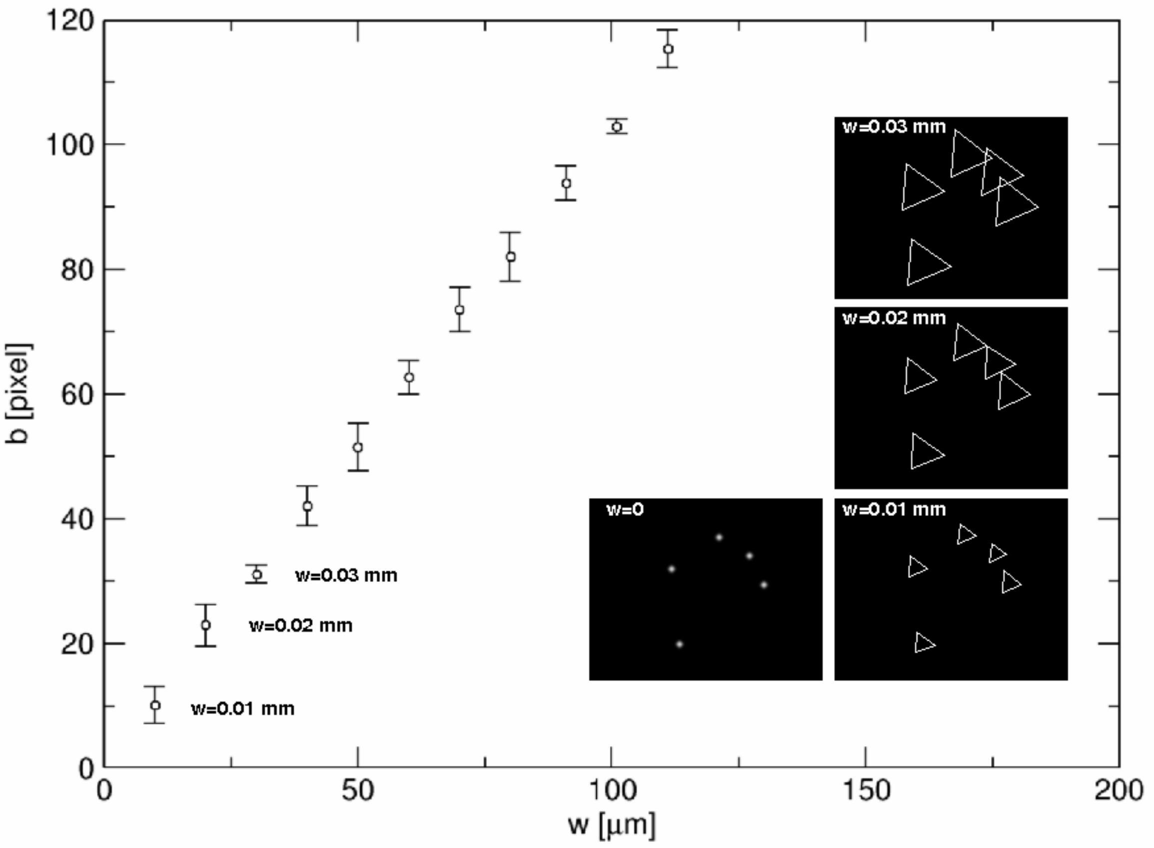

Figure 3.5. Mean separation b as a function of the relative distance w

Fig. 3.6 shows the corresponding focal distance **L**, on a per-particle basis. One can observe that **L** is not dependent on the **Z**-location, as expected. We obtain for **L** a mean value of 7.9765 mm with an RMS error of 393.5 μm. The resulting focal length **f** is 7.597 mm. The error on the mean value has four main sources. The first is related to the **Z**-positioning system, which has a limited resolution of 1 μm with an analog reading that affects the final accuracy on the reference displacement **w**. The second comes from the reduced CCD sensor size of the high-speed camera used in this experiment, giving a limited image resolution (1.166 pixel/µm on the image). The third is linked to the DDPIV processor itself, which introduces errors at the particle peak detection level. Finally, optical aberrations and geometrical distortions are not fully accounted for. In that latter case, errors can be partly overcome, as suggested by Pereira et al. (2002), following the distortion compensation procedure proposed by Soloff et al. (1997). Larger errors are observed for small **w**, where the pattern size is equally small, inducing larger relative error on the measurement of the image separation **b**.

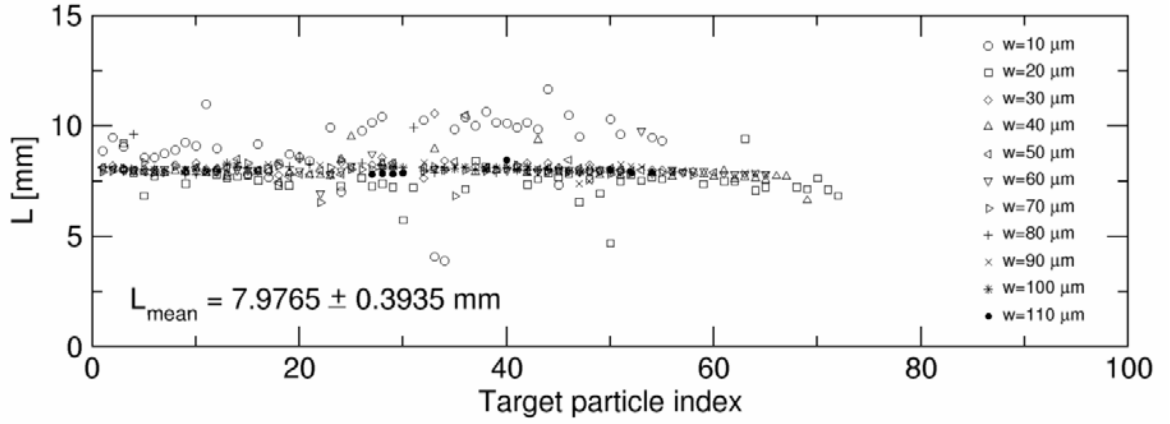

Figure 3.6. Focal distance L versus w, and mean estimate.

Using these calibrated parameters, the images are reprocessed to obtain the absolute depth **Z** with the following relation (see Eq. 3.1):

$$\mathbf{Z} = \mathbf{L}\left(\mathbf{1} + \frac{\mathbf{b}}{\mathbf{Md}}\right)^{-1} \qquad 3.4$$

Fig. 3.7 represents the measured relative displacement, named $\mathbf{w_m}$, versus the actual displacement of the target $\mathbf{w}$, with the regression line also reported. The relative error $|\mathbf{w_m} - \mathbf{w}| / \mathbf{FS}$, where $\mathbf{FS}$ stands for full scale and represents the depth range of the current μ-DDPIV system (110 μm), is within 3%.

The system sensitivity is defined as the separation change for a given Z-displacement, and is expressed as

$$\frac{\partial \mathbf{b}}{\partial \mathbf{Z}} = -\frac{\mathbf{MdL}}{\mathbf{Z}^2} \text{ with } \mathbf{Z} = \mathbf{L} - \mathbf{w} \qquad 3.5$$

We report in Fig. 3.8 the evolution of this quantity as a function of the distance $\mathbf{w}$ to the focal plane. The **b**-gradient is found to be fairly constant across the full measurement depth, with a variation of only 4% and an average value of 1.04 pixels for a displacement of 1 μm along the out-of-plane direction.

The image coordinates of the particle centroid are calculated using the subpixel algorithms described in Pereira and Gharib (2002). The particle images are modeled with non-isotropic two-dimensional Gaussian functions estimated through least squares minimization methods. Pixel resolutions lower than one tenth of a pixel are common with less accurate techniques such as the 3-point Gaussian fit or the bilinear interpolation. Hence, we can reasonably state that the depth resolution of the μ-DDPIV system assembled here is lower than 100 nm (i.e. <0.1% of **FS**).

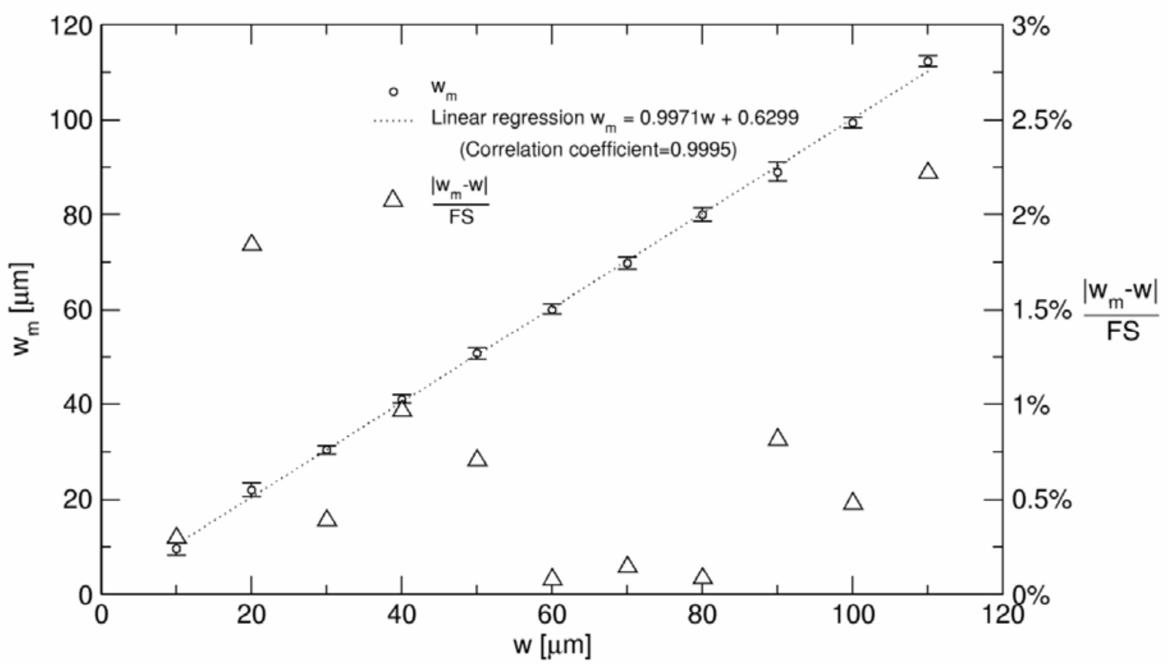

Figure 3.7. Measured distance to focal plane versus reference displacement w, and relative error with respect to the total displacement (full scale FS)

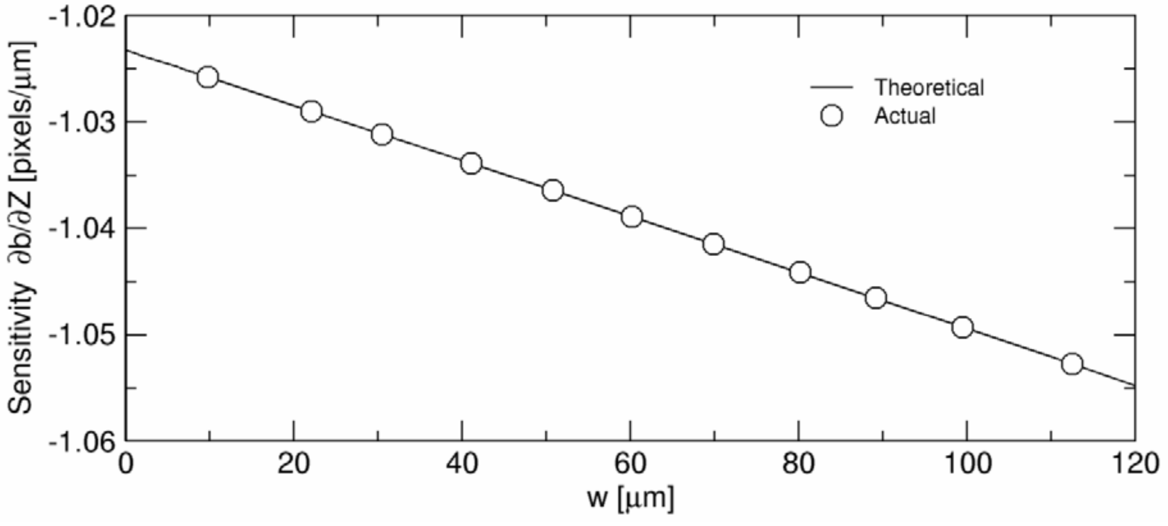

Figure 3.8. µ-DDPIV sensitivity curve

3.4 Uncertainty analysis

In this section, the measurement uncertainties are discussed. In this respect, theoretical developments are readily available in the literature: Pereira and Gharib (2002) have laid out the formulas for a generic DDPIV layout with two apertures. Kajitani and Dabiri (2005) have extended these formulas to describe a DDPIV system composed of three apertures arranged in the form of an equilateral triangle. This particular layout has been implemented in most of the macroscale DDPIV systems developed so far (see for instance Pereira et al, 2000), and is also the configuration used for the μ-DDPIV setup proposed here.

Let **$\delta(dX)$** , **$\delta(dY)$** and **$\delta(dZ)$** be the measurement uncertainties on **X**, **Y**, **Z**, respectively. They represent the uncertainties on the object space displacements (**dX**, **dY**, **dZ**). Tab. 3.1 summarizes the relations given by Pereira and Gharib (2002) and by Kajitani and Dabiri (2005):

Table 3.1. Uncertainty definitions, according to Pereira and Gharib (2002) and Kajitani and Dabiri (2005)

Uncertainty type	Pereira and Gharib (2002)	Kajitani and Dabiri (2005)
$\delta(\mathrm{d}X)$	$K\|Z\|d\Delta x\sqrt{1+\frac{2X^2}{d^2}}$	$\frac{\Delta x}{\sqrt{3}}K\|Z\|d\sqrt{1+\frac{3X^2}{d^2}}$
$\delta(\mathrm{d}Y)$	$K\|Z\|d\frac{\Delta x}{\sqrt{2}}\sqrt{1+\frac{4Y^2}{d^2}}$	$\frac{\Delta x}{\sqrt{3}}K\|Z\|d\sqrt{1+\frac{3Y^2}{d^2}}$
$\delta(\mathrm{d}Z)$	$\sqrt{2}KZ^2\Delta x$	$KZ^2\Delta x$

with $\mathbf{K} = \mathbf{1/MdL}$. $\mathbf{\Delta x}$ represents the uncertainty on the image plane, i.e. the uncertainty on the determination of the pixel location of a particle image centroid. Note that the uncertainties on $\mathbf{X}$ and $\mathbf{Y}$ are identical in Kajitani and Dabiri (2005), while they differ in the work by Pereira and Gharib (2002) because of the two-dimensional derivation used thereby.

To establish the measurement uncertainties $\boldsymbol{\delta}\mathbf{(dX)}$, $\boldsymbol{\delta}\mathbf{(dY)}$, and $\boldsymbol{\delta}\mathbf{(dZ)}$, we consider the trajectories of the individual calibration particles used in the previous section and calculate their deviation in all three directions from the actual path, which is a pure translation along the $\mathbf{Z}$-axis. In a sense, we use the calibration dataset as a flow test case to qualify the performance of the μ-DDPIV system. We represent in Fig. 3.9 the experimentally determined uncertainties, expressed in terms of root mean square errors, as a function of the distance $\mathbf{w}$ to the focal plane. This figure shows that the uncertainty levels on the particle in-plane location (i.e. $\mathbf{X}$ and $\mathbf{Y}$ coordinates) are fairly equal, as expected. This is also in full agreement with the theoretical formulations above. The in-plane uncertainty is about 0.5 μm. For the out-of-plane component, the uncertainty is found to be larger with a mean value of 1.2 μm. The in-plane uncertainty has a slightly decreasing trend starting from the focal plane ($\mathbf{w=0}$) that is in agreement with the linear relationship existing between $\boldsymbol{\delta}\mathbf{(dX)}$ and $\boldsymbol{\delta}\mathbf{(dY)}$ and the depth coordinate $\mathbf{Z}$, for constant $\mathbf{X}$ and $\mathbf{Y}$. Beyond $\mathbf{w}$=50 μm, the trend has a seemingly increasing behavior, which could possibly be an effect of the image blurring that takes place as the particles move off from the focal plane, hence affecting their intensity and their detection, and ultimately the particle location error. However, a parametric study based on particle size and aperture characteristics is desirable to identify the elementary sources of errors and better quantify their individual contribution to the overall performance.

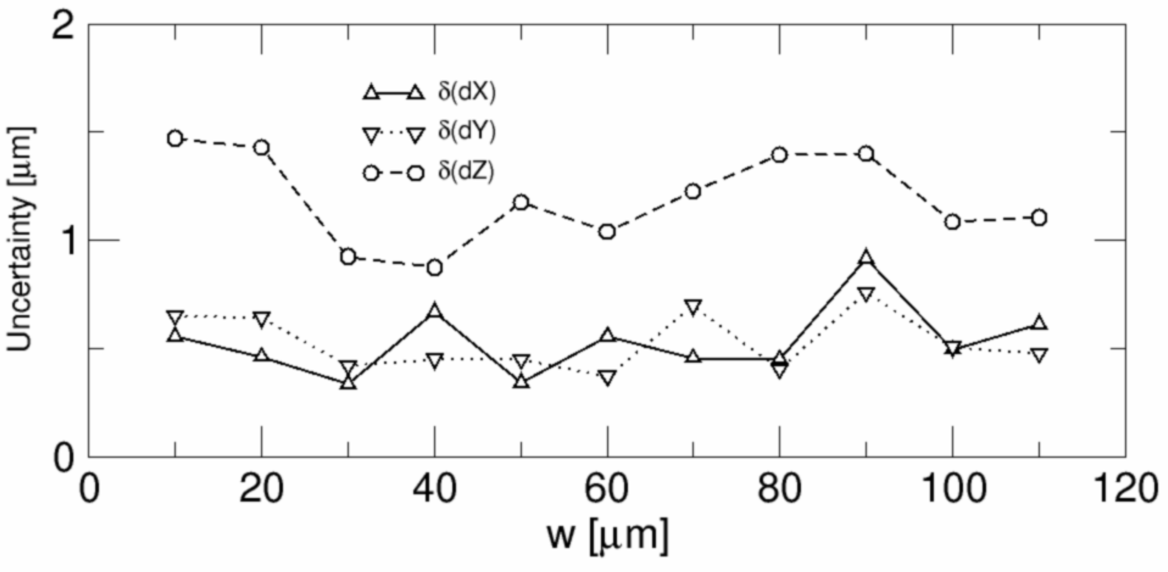

Figure 3.9. Uncertainty levels on the space coordinates X, Y, Z

The ratio between the out-of-plane and the in-plane uncertainties is a useful parameter that is generally used to measure the overall performance of a 3-component measurement system, as outlined by Pereira and Gharib (2002). For a 3-aperture system, Kajitani and Dabiri (2005) give the following expressions for the ratios ε_{ZX} and ε_{ZY} of the out-of-plane error $\delta(dZ)$ to the in-plane components $\delta(dX)$ and $\delta(dY)$, respectively:

$$\varepsilon_{ZX} = \frac{\delta(dZ)}{\delta(dX)} = \frac{\sqrt{3}(|Z|/d)}{\sqrt{1+\frac{3X^2}{d^2}}} \quad \text{and} \quad \varepsilon_{ZY} = \frac{\delta(dZ)}{\delta(dY)} = \frac{\sqrt{3}(|Z|/d)}{\sqrt{1+\frac{3Y^2}{d^2}}} \qquad 3.6$$

We report in Fig. 3.10 the values of these ratios, versus the distance **w** to the focal plane. We also plot the theoretical value, as per equation 3.6 above, calculated at the centerline of the optical system (**X**=**Y**=0) where ε_{ZX} and ε_{ZY} reach their maximum. The measured ratios are found to be slightly larger than the theoretical value, with a mean of 2.4 μm for ε_{ZX} and 2.33 μm for ε_{ZY}, while the predicted value is sensibly constant at 1.96 μm. However, there is an overall strong agreement between the actual and the theoretical trend that confirms the well-sounded nature of the calibration approach. It is important to underline the fact that the out-of-plane error is only two to three times as large as the in-plane components, which is a peculiar characteristic of the μ-DDPIV layout implemented here, where the focal length is almost equal to the focal distance. This is in contrast with the results obtained with a macroscopic-type DDPIV design, where the focal distance **L** is typically much larger than the aperture separation **d**. Pereira and Gharib (2002) report ratios varying from 4 to 6 for an error-free system with **L**=1000 mm and **d**=100 mm. Hence, higher magnification objectives (i.e. >20X) are expected to provide even better performance, at the cost a shallower mappable volume.

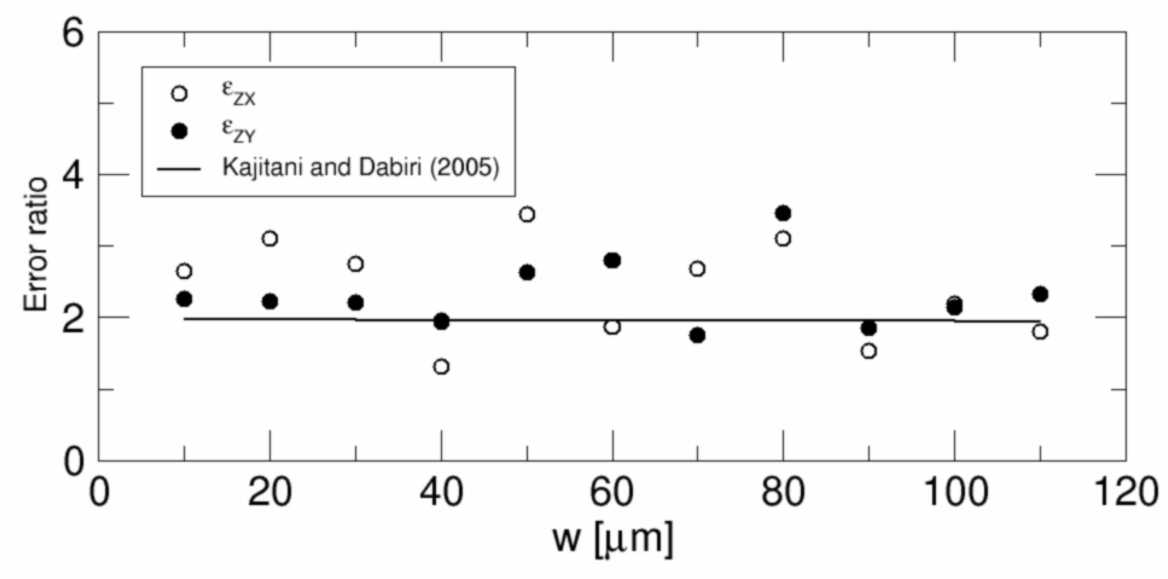

Figure 3.10. Out-of-plane to in-plane error ratios ε_{ZX} and ε_{ZY}

Finally, we estimate the image uncertainty $\Delta\mathbf{x}$, expressed in pixel units from the equations listed in Table 3.1 and report the result on Fig. 3.11. As expected, $\Delta\mathbf{x}$ is found to be fairly constant across the volume depth, with a mean value of 1.077 pixels and a standard deviation of 0.145 pixels.

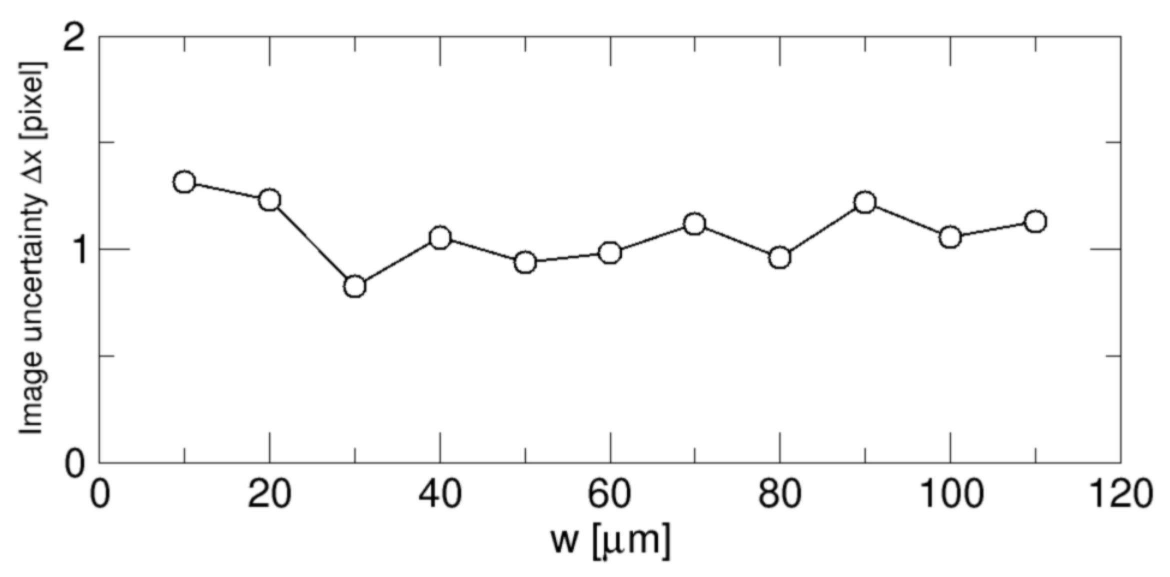

Figure 3.11. Uncertainty on the pixel coordinates

3.5 Conclusion and perspectives

A three-dimensional visualization system was devised based on the defocusing DPIV technique (DDPIV) to provide quantitative information on micron-scale flows. The defocusing concept was implemented for use with fluorescent microscopy and a calibration procedure was outlined to establish the optical parameters needed to apply the DDPIV analysis. Sub-micron resolution has been verified and the measurement uncertainties have been fully determined.

The microscopic defocusing technique (μ-DDPIV) introduced here provides a method to visualize and quantify three-dimensional real-time flow. With an objective lens of higher magnification and smaller tracer particles, the system can be easily extended to submicron flow visualization. And the micron-scale imaging system can be adopted to *in vivo* imaging of biological fluid systems as well.

One limitation of the microscopic DDPIV technique, as it was applied in this work, is that it requires high intensity illumination because of the high f-number. Tien el al. (2007) provided a possible overcome of this limitation by floodlighting the whole field of view and seeding the flow by black tracer particles under bright field illumination. However, for *in vivo* biological fluid imaging, instead of bright light illumination fluorescence imaging is usually preferred due to its highly enhanced image contrast within even thick tissues. And the intensity of excitation light source must be within reasonable limits to avoid damage to the biological system. Hence, future development in this direction will require the use of intensified and high-resolution digital cameras.

Further study is also foreseen to address the effect on the performance of μ-DDPIV of parameters such as the numerical aperture of the objective, the size of the apertures and size of tracer particles.

References

Bown MR, MacInnes JM, Allen RWK, Zimmerman WBJ (2005) Three-component microfluidic velocity measurements using stereoscopic micro-PIV. *In: The 6th Int. Symp. on PIV (PIV'05),* Pasadena, CA, Sept. 2005.

Kajitani L, Dabiri D (2005) A full three-dimensional characterization of defocusing digital particle image velocimetry. *Meas Sci Technol* 16:790-804

Hove JR, Koster RW, Forouhar AS, Acevedo-Bolton G, Fraser SE, Gharib M (2003) Intracardiac fluid forces are an essential epigenetic factor for embryonic cardiogenesis. *Nature* 421, 172-177.

Inoué S, Spring KR (1997) *Video microscopy*, 2nd edn. Plenum, New York.

Pereira F, Gharib M, Dabiri D, Modarress D (2000) Defocusing digital particle image velocimetry: a 3-component 3-dimensional DPIV measurement technique. Application to bubbly flows. *Exp Fluids* 29 (Suppl): S78-S84

Pereira F, Gharib M (2002) Defocusing digital particle image velocimetry and the three-dimensional characterization of two-phase flows. *Meas Sci Technol* 13:683-694.

Pu Y, Song X, Meng H (2000) Holographic PIV for diagnosing particulate flows. *Exp Fluids* 29:S117.

Santiago JG, Wereley ST, Meinhart CD, Beebe DJ, Adrian RJ (1998) A particle image velocimetry system for microfluidics. *Exp Fluids* 25:316-319.

Soloff SM, Adrian RJ, Liu ZC (1997) Distortion compensation for generalized stereoscopic particle image velocimetry *Meas Sci Technol* 8:1441-54.

Suzuki H, Nakano M, Kasagi N, Ho CM (2003) Particle tracking velocimetry measurement of chaotic mixing in a micro mixer. *Int. Symp. Micro-Mechanical Engineering (ISMME2003)*, Tsuchiura, Japan, 1-3 December 2003.

Tien W, Kartes P, Yamasaki T, Dabiri D (2007) A modified single camera three-dimensional defocusing particle image velocimetry system. *Exp Fluids* (submitted).

Willert CE, Gharib M (1992) Three-dimensional particle imaging with a single camera. *Exp Fluids* 12:353-358.

Wu M, Roberts JW, Buckley M (2005) Three-dimensional fluorescent particle tracking at micron-scale using a single camera. *Exp Fluids* 38:461-465.

Yoon SY, Kim KC (2006) 3D particle position and 3D velocity field measurement in a microvolume via the defocusing concept. *Meas Sci Technol* 17:2897-2905.

Chapter 4

3D flow mapping of droplet internal circulation

4.1 Introduction

Minute fluid droplet (~1 mm) evaporation in a gaseous media occurs in many biological and engineering processes. There is a continuous opinion that the phenomena associated with the evaporation (e.g., evaporation rate, surface area change, contact angle change, etc.) are fundamental in a large variety of practical applications and scientific researches, for instance combustion of fuel, heat radiators, internal combustion engines, and colloidal suspensions in particle adsorption (Uno et al., 1998). Recent studies discovered further application of droplet drying (evaporation) related effects in biochemistry such as DNA array hybridization. DNA samples sandwiched in a conventional closed array system made up of glass surfaces always have limited access and can not adequately accommodate the arrays. However, evaporation at the liquid surface will generate forces and uniformly pull the coiled DNA chains to a straight manner. Jing et al. (1998) and Abramchuk et al. (2001) found that DNA stretching through the process of a droplet drying is able to produce usable population of elongated samples without modifying the biochemical properties, where patterns of the internal circulation flow are believed to play a key role.

While the droplet evaporation process is commonly considered as diffusion between the liquid and the outside environment, the droplet exhibit a vigorous internal convection, or circulation, when the evaporation is sufficiently fast. As an evaporating fluid droplet decreases in mass, the external flow of the surrounding gas is coupled with the internal flow via the boundary conditions on the surface, where mass and energy transfer exists. In a volatile media such as ethonal/water solution, the phase change from liquid to gas through the liquid-air surface generates a nonuniform concentration distribution, which in turn creates a surface tension gradient inside the droplet. The presence of gradient in surface tension will naturally force the surface fluid towards regions of higher surface tension, generating a flow pattern (or convection) which tends to equilibrate the concentration distribution, balance surface tension gradients and finally stop the convection to a state of stability. The phenomenon of surface tension causing internal circulation is called Marangoni effect, which can be generated by temperature gradient as well. Other factors such as buoyancy force may also have influence in convections in some instances (Savino et al., 2002).

Some investigations have been carried out to deal with the evaporation of droplets with Marangoni effect. Most of the previous works have generally focused on numerical simulations of the internal circulation, for instance Shih and Megaridis (1996), Dwyer and Shaw (2001), and Wegener et al. (2007). However, direct experimental measurement of droplet interior flow is scarce. Very few experimental studies to obtain quantitative information on the internal circulation have been done in the past because of the difficulties of flow visualization such as small flow domain and image distortion due to light reflection on the spherical surface. Hegseth et al. (1996) presented the first flow streaks image in a methanol drop. Savino et al. (2002) obtained velocity vectors of a hanging n-octance drop in presence of Marangoni effect. A recent work performed by Kang et al. (2004) have devised a mapping method based on ray tracing to correct for the strong image distortion caused by the refraction of light at the air-water interface of the droplet. Illuminating a sessile droplet from the side with a thin laser light sheet and observing the flow with a long-distance zoom lens, they applied the PIV technique and their correction method to obtain planar 2-component velocity fields. All the experimental studies could in particular demonstrate the existence of a vortex-type convection flow during the evaporation process.

However, fully three-dimensional flow mapping is a necessity as previous computational results suggested if one intends to address issues related to the droplet evaporation mechanism, such as the effect of Marangoni instabilities or the effect of the contact angle and of the evaporation rate. In the present work, we will apply the newly developed microscopic system to acquire time-resolved quantitative volumetric velocities of a volatile water droplet.

4.2 Materials and methods

4.2.1 Droplet preparation

A solution with 5% ethanol in de-ionized water was used as the evaporating liquid in this experiment. The 2 µm yellow-green fluorescent microspheres identical to previous calibration targets (see Section 3.3.2) were added to the solution as tracer particles. A droplet of 2 µl was placed on a Petri dish with a micro-pipette. The diameter of the droplet was about 2 mm. The Petri dish was transferred to the translational stage under the microscope objective lens and rested for a few seconds before imaging to prevent external disturbance to the interior flow. Flow image sequences of the internal circulation were captured and recorded by the high-speed camera at 250 frames per second. The experiment was performed under room temperature. Fig. 4.1 represents a schematic of the test droplet and the coordinate axes, with indicated two test regions in the experiments. The shape of the droplet is axisymmetric, with the droplet axis parallel to **Z** direction. We present three cases, observed under different experimental conditions to illustrate the use of μ-DDPIV in essence and the volumetric flow field inside the droplet.

Time-resolved 3D flow mapping of a droplet internal circulation caused by evaporation was achieved with the particle spatial coordinates inferred from their DDPIV images. Particle tracking (PTV) was used to derive the velocity field from the particle spatial field, see Pereira et al. (2006).

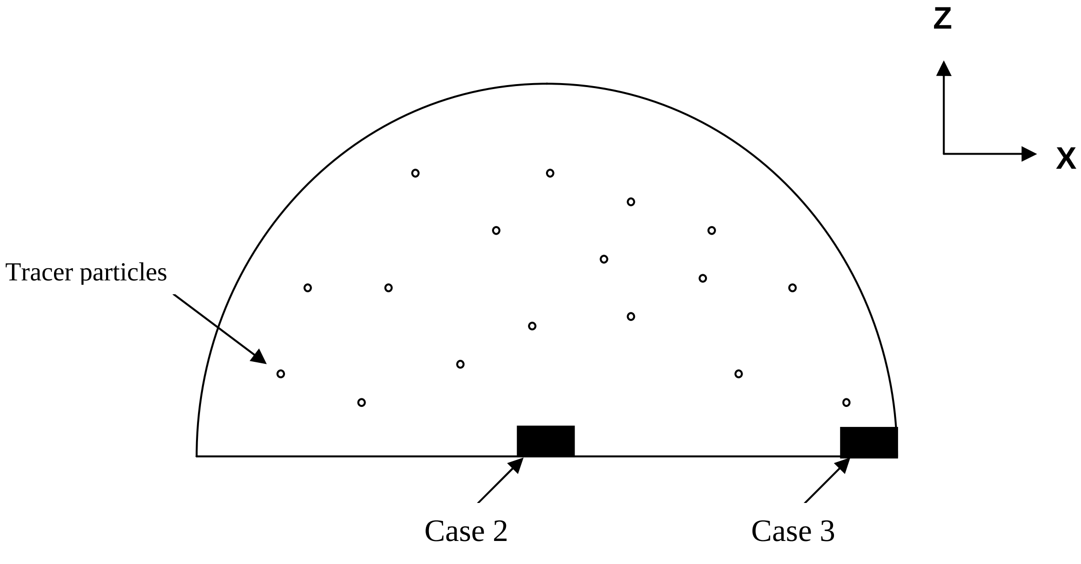

Figure 4.1. A schematic of a sessile droplet with solid tracer particles. The two black areas indicate the test regions in the experiments.

4.2.2 Particle tracking

In μ-DDPIV method, since three-dimensional coordinates of individual tracer particles are reconstructed before further data processing, PTV is most suitable for velocity mapping in the present situation. The PTV method tracks individual particle images in consecutive image frames and computes the directionally resolved vector for each matched particle. For the consideration of reliability and simplicity in this work, three different tracking schemes, including nearest neighbor method, neural network method, and relaxation method, have been chosen among the many tracking algorithms available.

The nearest neighbor method considers only the search volume. The link criterion is the minimum distance of a match within a predefined neighborhood volume (Pereira et al., 2006).

The neural network method we used here was described by Labonté (1999). This approach generally divide two consecutive image frames into two similar subnetworks composed of large amount of neurons, with a corresponding weight vector assigned to each neuron. The basic goal of this method is to that the weight vectors of the neurons converge to a common vector, through an iterative competition between all neurons of each subnetwork. The iterative process starts with the predefined radius of the neighborhood volume, while adjusting the radius to contain an increasingly larger number of matching particles as well as the weight vectors after each cycle. The neural network is usually adopted as a pre sorting procedure for the nearest neighborhood method. After the iterative process completes, the finally updated weight vectors are used as a link criterion for the nearest neighborhood search to find the matching particle pairs.

The relaxation scheme was described by Baek et al (1996), and implemented into DDPIV by Pereira et al. (2006). This algorithm has proven to be superior, both in performance and robustness, to other approaches. The basic concept of particle tracking in the relaxation method is to search for the most probable link of a given particle while assuming similar displacements of its neighbor particles (the so-called quasi-rigidity condition), within a neighborhood of specified size. Thus, the search for the matching particle in the next time step is made in the direction that the neighbor particles are most likely pointing to. In an iterative process, the correct link probability is gradually increased close to unity while the other probabilities tend to zero. After successful termination of this iterative process, the correct particle link is the one with the highest probability. Unlike the neural network scheme, the neighbor volume during iterative process is fixed in relaxation technique. Therefore, enough matching particles have to be selected in the search volume to guarantee a reliable particle link upon the completion of the iterative process.

There is a criterion in the PTV method which requires the distance between tracer particles to be larger than the displacement. Since the high-speed image acquisition was used in the system and particle density was low in the images, the distance of a particle traveled between two consecutive time frames is smaller than the separation between particles even though the motions of our seeding tracers are highly dynamic. Hence, the criterion was met and PTV is capable of obtaining 3D velocity vectors from the images. In addition, the recorded image sequences described continuous movements of each particle (i.e., no strong displacement gradient exists between every two consecutive images.), and most particle links can thereby be correctly found. So the complex velocity fields inside the droplet can be reconstructed.

4.3 Results

4.3.1 Case 1

Fig. 4.2 shows, on the top image, the accumulated information of the 550 DDPIV images recorded in the first sequence, and shows the complex trajectories of the fluorescent markers as they are transported by the internal flow. Note that, on a DDPIV image, every flow marker is represented by a triplet of particle images (see Fig. 4.4 for a sample image); hence this image provides only indicative information. The bottom plot represents the corresponding reconstructed particle field, where the particles are individually located in space and time. The domain has been translated to the system origin, hence **Z**=0 represents the surface of the Petri dish on which the droplet sits. The volume depth is slightly less than 160 μm, while the field of view is about 400x300 μm^2. The present measurements explicitly demonstrate the capability of our imaging system in volumetric quantitative microscale flow visualization, without much physical consideration of the flow itself.

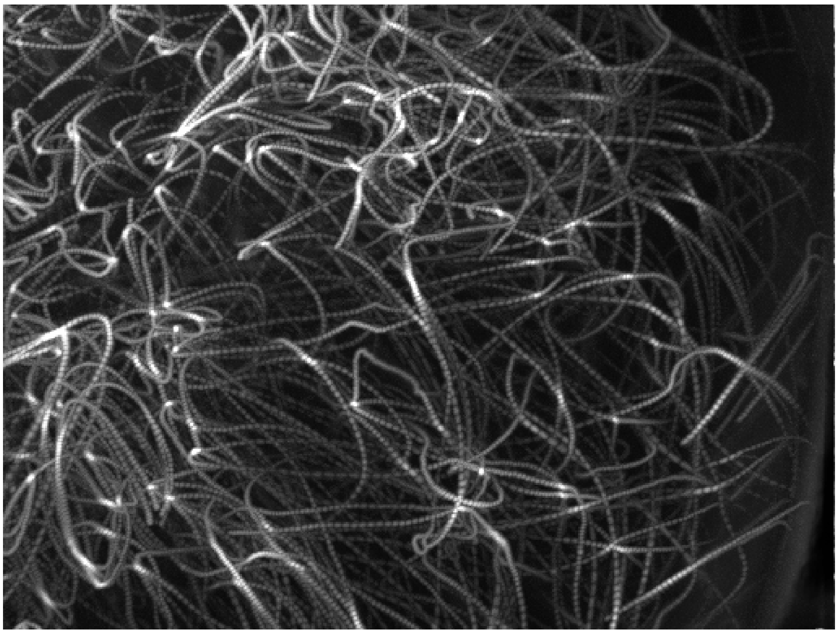

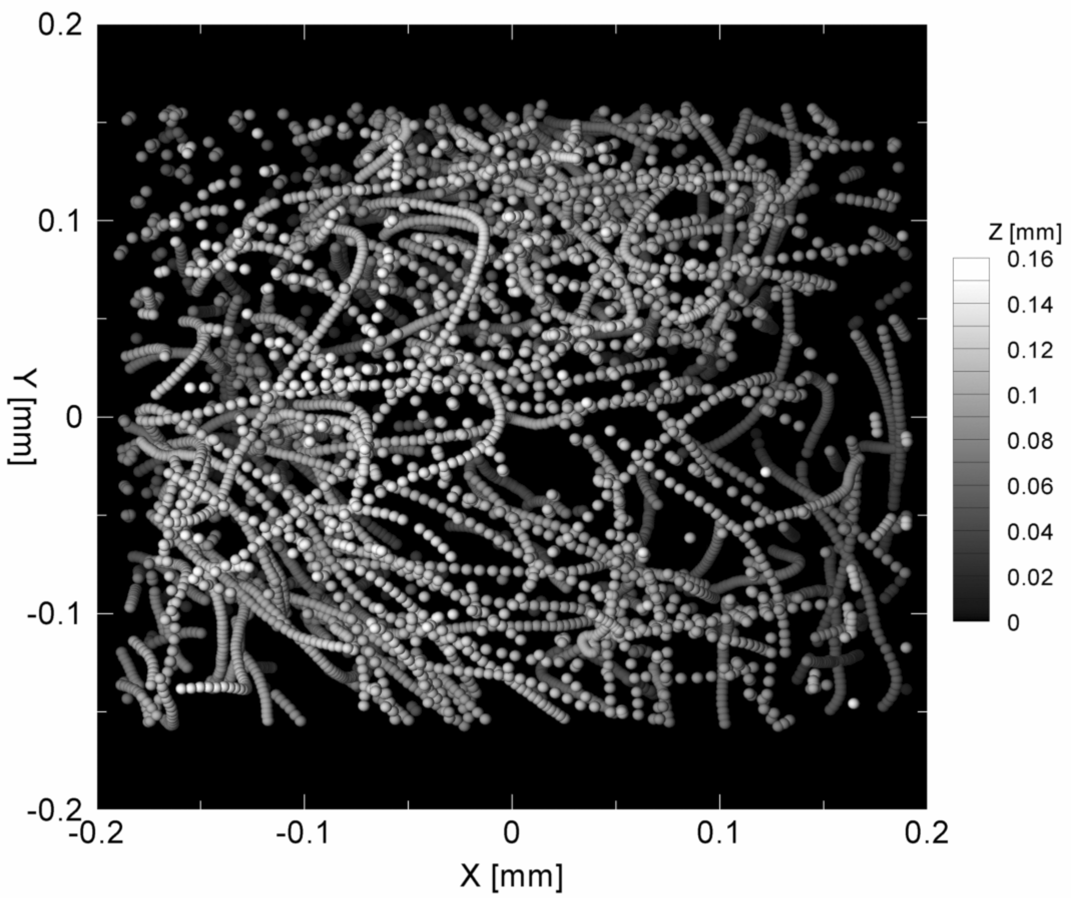
0.2
0.1
0
-0.1
-0.2
-0.2
-0.1
0
0.1
0.2
Y [mm]
X [mm]
Z [mm]
0.16
0.14
0.12
0.1
0.08
0.06
0.04
0.02
0

Figure 4.2. Droplet internal flow (case 1): sequence of 550 DDPIV triple-aperture images (top) and reconstructed particle field (bottom). (Adapted from Pereira et al. 2007)

4.3.2 Case 2

In the following two cases, the droplet was seeded with the fluorescent particles at a lower density. More than 10 experiments have been carried out in each case. Flow near the bottom center of the droplet was mapped in case 2, with velocities resolved by PTV. As in the previous case, the volume is translated to the system origin, with **Z**=0 indicating the Petri dish surface. The flow field exhibits a fountain-like "upstream" motion from near the central region of the base plane (see Fig. 4.3). Fluids near the droplet bottom move closer towards the center as well as vertically towards the core of the droplet. As was discussed in other numerical simulations, this phenomenon is due to the convection and the continuity of the flow itself. Since the droplet has an axisymmetric structure, fluids in the central core moves only upwards along the axis, then return to the base plane along the outer surface. The measuring volume is 400x300x100 μm^3. The flow field does not exhibit a high velocity gradient; and the mean velocity is about 0.05 mm/s.

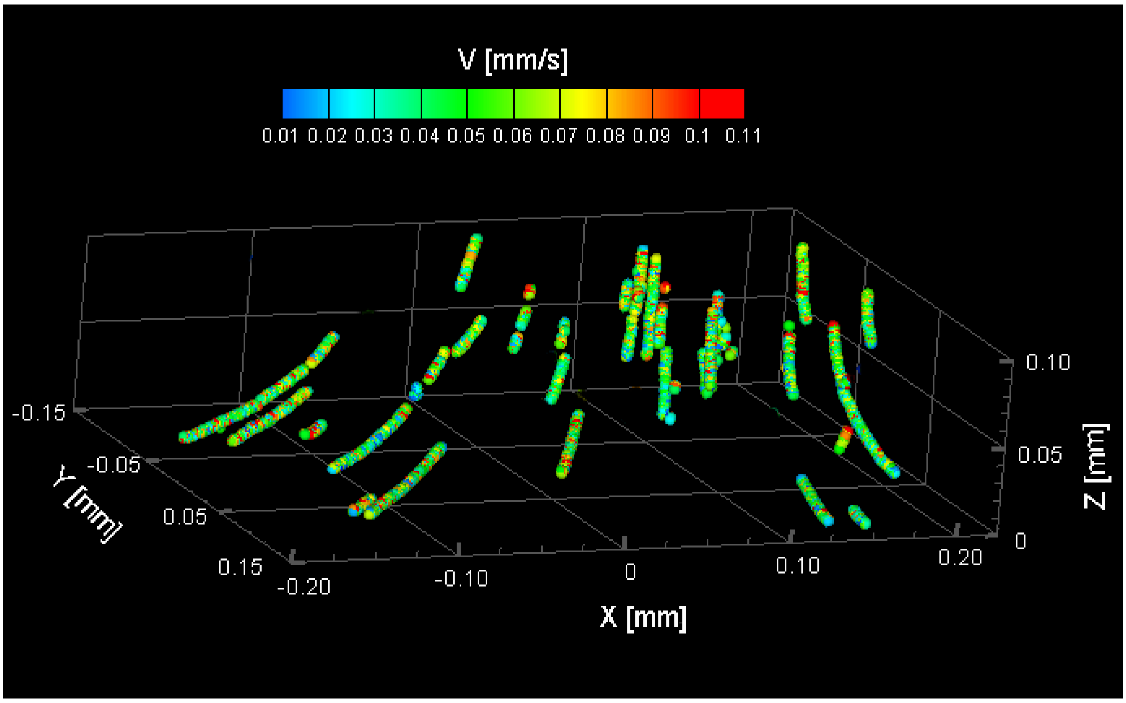

Figure 4.3. Reconstructed droplet internal flow (case 2): velocity and particle fields near the bottom center of the droplet. Velocity magnitudes are color coded.

4.3.3 Case 3

Interior flow near the edge was imaged in the experiment due to the highly dynamic and complex Marangoni flow patterns near the surface. Fig. 4.4 shows the time-lapsed DDPIV images of the tracer particles. Size change of the defocused triangular patterns represents particle movements in depth. Fig. 4.5 exhibits the reconstructed particle field together with the velocity field, calculated using the tracking technique. The size of the particle markers is proportional to their **Z**- location within the droplet, while their color is indicative of their velocity. The volume depth is 100 μm, while the field of view is about 300x250 μm^2. The maximum velocity is approximately 1.3 mm/s, which is much faster than that in the core (Fig. 4.3). Faster fluid motions and vortex flow near the edge produce mass transfer between the surface and the core, imposing concentration re-distribution in the droplet.

To further illustrate the potential for Lagrangian analysis of the method proposed here, we isolated a particle and reconstructed its path in space and time. We developed a long-time tracking algorithm to establish the particle link from frame to frame. Hence, by selecting a particle in a given frame, the algorithm reconstructs its complete path by tracking the particle in the neighboring backward and forward frames. Fig. 4.6 represents one such single particle track, extracted from the data shown in Fig. 4.5, with the color and size indicating respectively the particle local velocity and the depth location. Fig. 4.7 shows the evolution in time and space of the velocity vector (U_x,U_y,U_z) and of the acceleration (U'_x,U'_y,U'_z) of this single particle as a function of time. Minute information on the particle motion is shown in Fig. 4.8, which represents the fluctuations of the particle location with respect to its mean path. The plot shows a periodic motion of the particle along the X-axis, a similar behavior being also observed on the other axes. The frequency of the fluctuation is about 100 Hz and the amplitude is 200 nm. This motion has no physical origin and is believed to be an artifact of the experimental setup, most probably a structural vibration induced by a rotating mechanical part. However it allows us to clearly illustrate the capability of the μ-DDPIV technique, as implemented here, to capture and isolate a submicron scale feature of the flow. It also confirms the 100-nm resolution performance estimated during the calibration process.

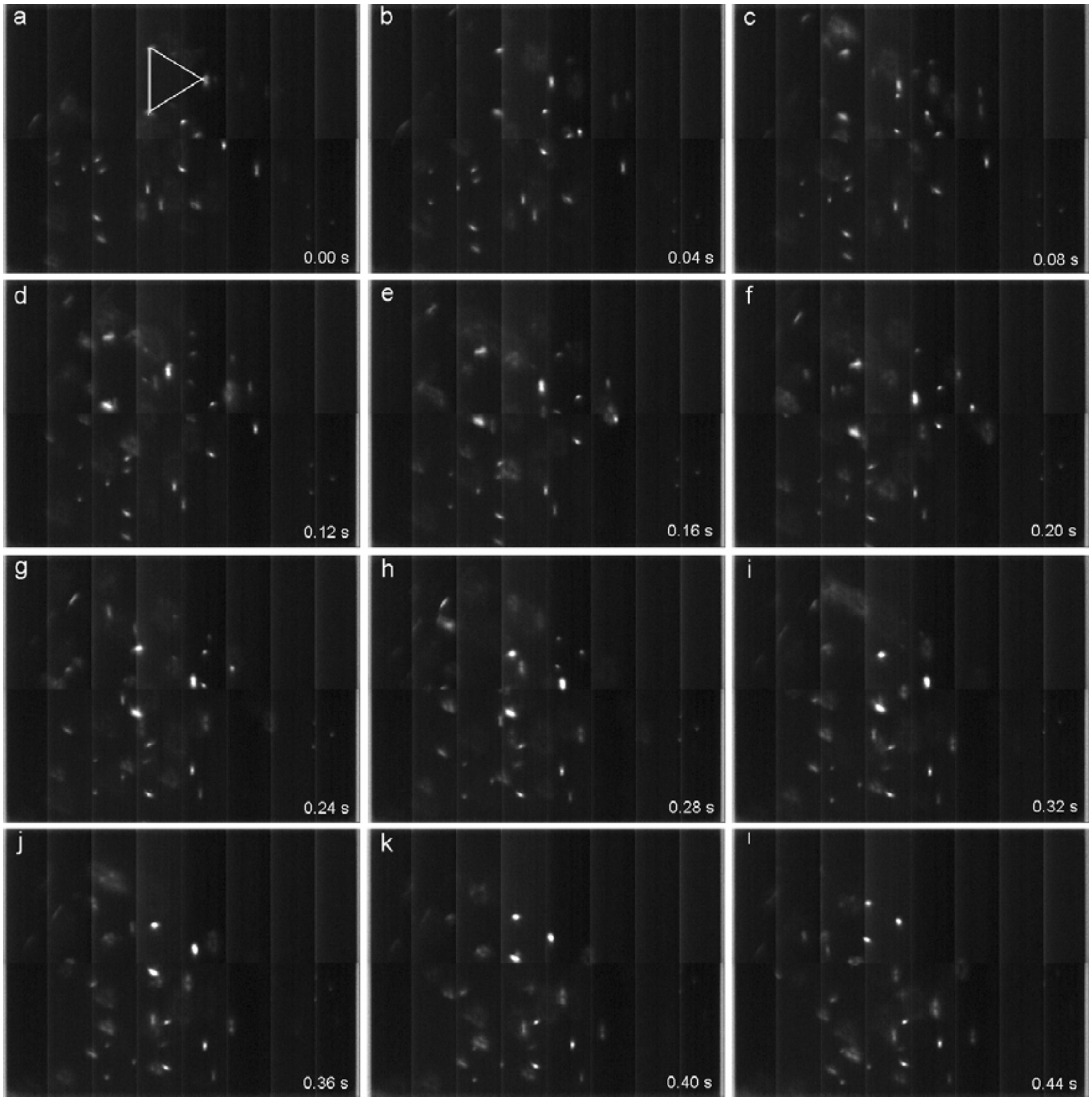

Figure 4.4. Time-lapsed DDPIV images of 2-μm tracer particles seeding droplet internal circulation at the edge (case 3). A triangle was connected in (a) to demonstrate the defocused image pattern.

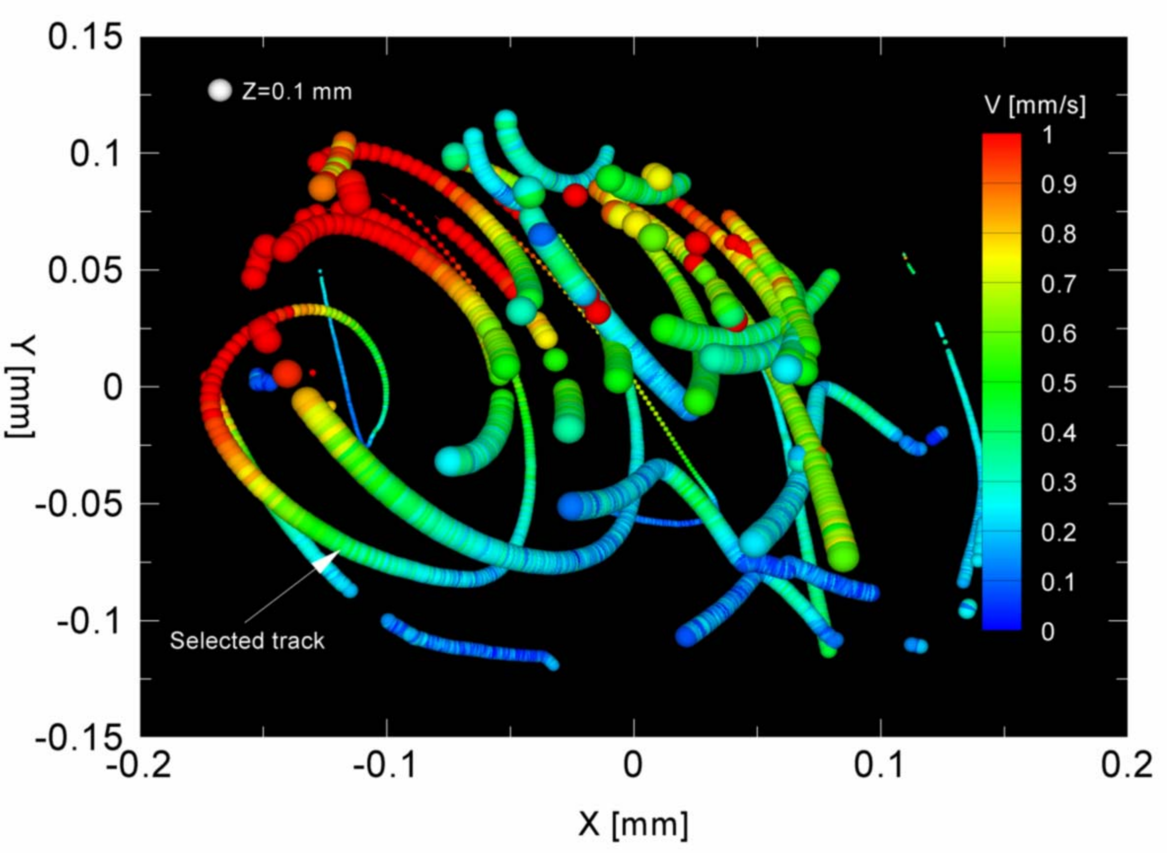

Figure 4.5. Reconstructed droplet internal flow (case 3): particle and velocity fields. (Adapted from Pereira et al. 2007)

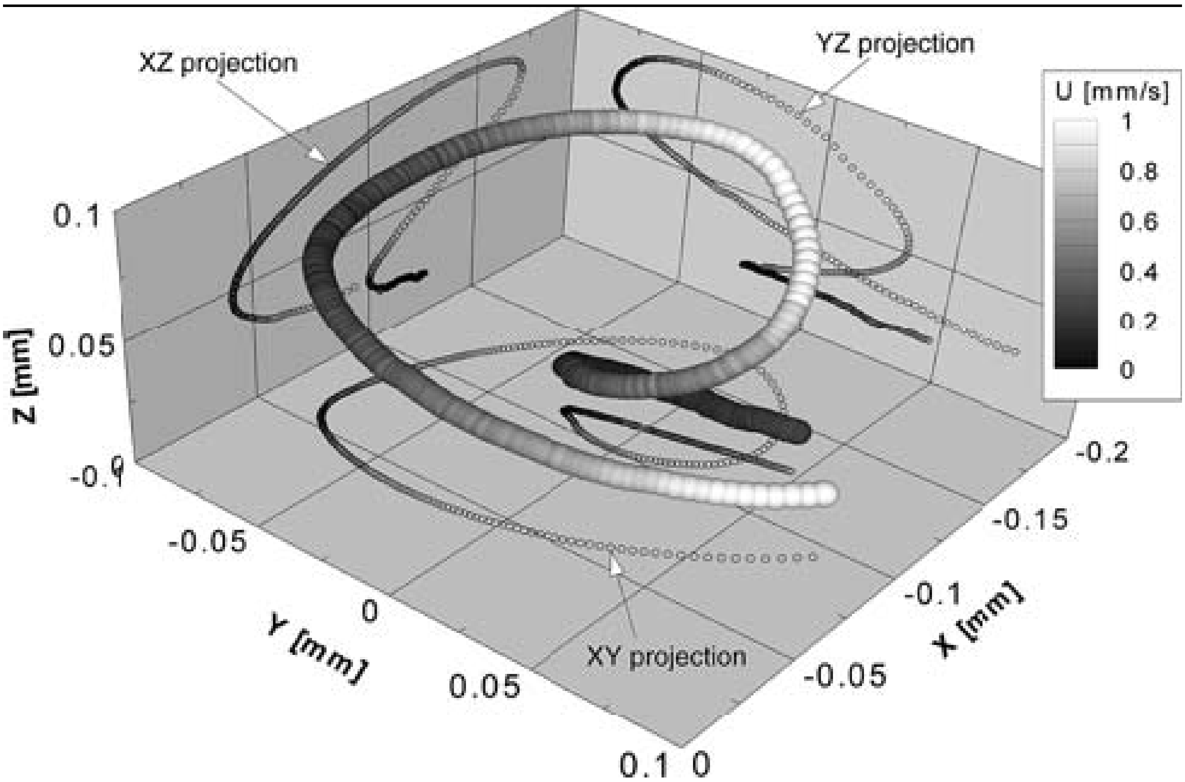

Figure 4.6. Droplet internal flow (case 3): velocity along a single track. (Adapted from Pereira et al. 2007)

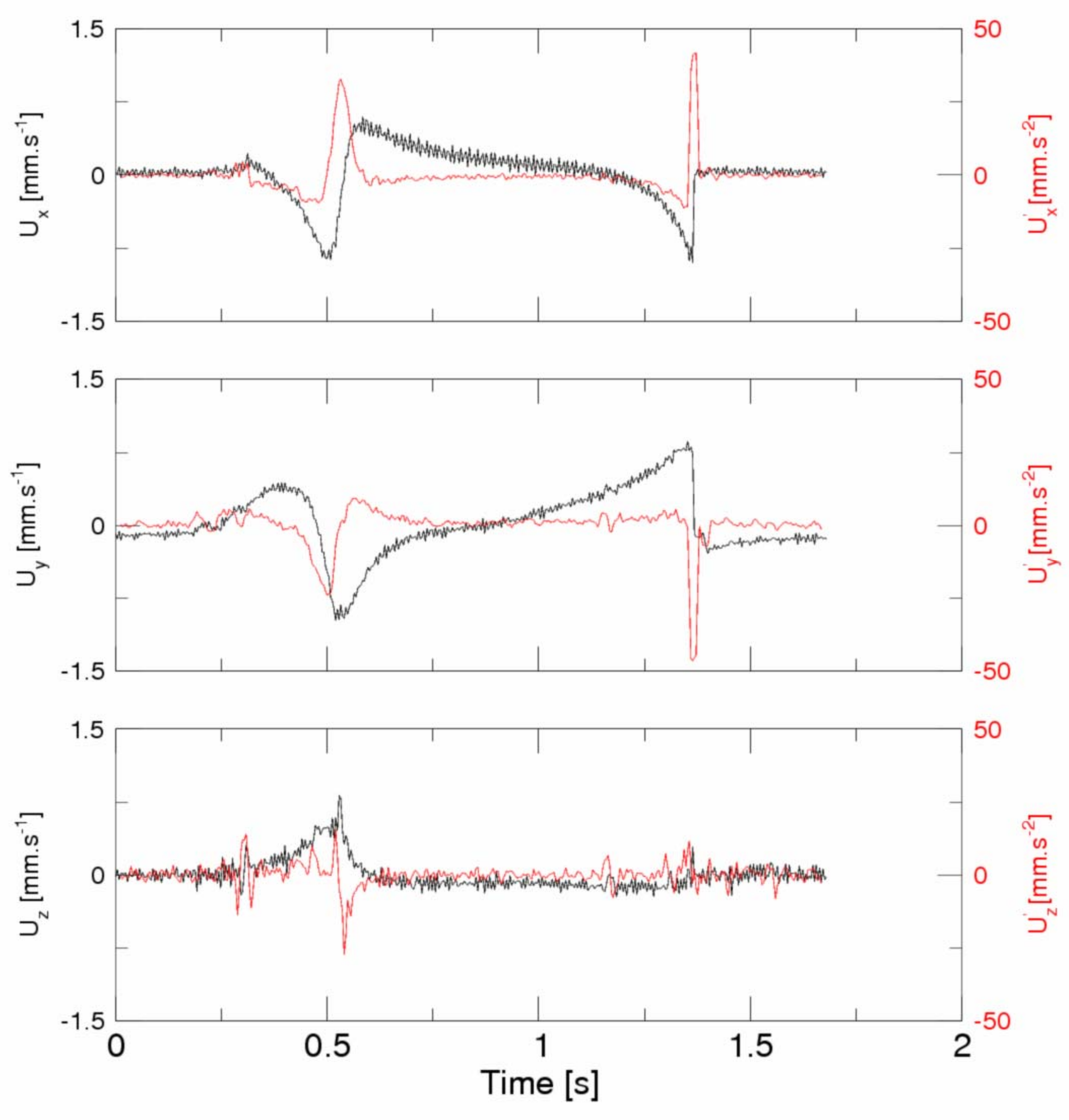

Figure 4.7. Velocity (black) and acceleration (red) history along the extracted track. (Adapted from Pereira et al. 2007)

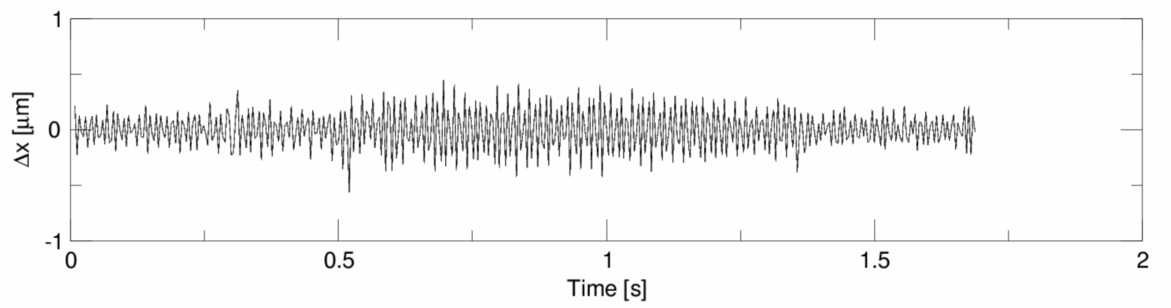

Figure 4.8. Droplet internal flow (case 2): particle X-fluctuations along the extracted track. (Adapted from Pereira et al. 2007)

4.4 Conclusion and discussion

Capability of the newly developed μ-DDPIV system for quantitative microscale flow volumetric imaging has been well demonstrated by the flow mapping of evaporating droplet internal circulation in the bottom center and near the edge. An additional advantage of the present approach is that illumination of the droplet was perpendicular to the substrate surface and images were captured from underneath the transparent substrate, which avoided image distortion due to droplet surface reflection and ensured accuracy of the measurement.

Evaporation of ethanol at the droplet surface makes the fluid density in the core lower than that near the surface. This density distribution may induce another type of convection due to buoyancy forces, which drives the fluid near the surface to the inner regions if buoyancy is the primary factor inducing interior flow. However, in practical experiments one could only observe a fountain-like vertical flow moving upwards from the central core of the droplet. Therefore Marangoni convection dominates the internal circulation in the ethanol droplet with moderate concentration in this experiment. In addition, the fountain-like fluid motions suggested that particles would not be able to deposit on the bottom due to the shear stress by the flow. This characteristic in droplet evaporation can be broadly applied to microfluidic devices to remove microparticles clogged on the surface of microchannels (Chang and Velev, 2006).

2D experiments only included velocity fields of a slice of a hemispherical droplet without extension in the third direction in space, equivalent to the **X**-**Z** (or **Y**-**Z**) plane in the present 3D coordinates. However, 2D flow field is not able to provide explicit information on fluid motions in the entire 3D space. Experimental results by Kang et al. (2004) obtained a toroidal shape of velocity distribution in the meridian plane (i.e., a 2D cross-section including the droplet axis), exhibiting vertical motions in the core and two ring-like vortices parallel to the plane near the edge. Based on previous 2D measurements and the assumption of axisymmetry, one could only imagine the 3D velocity field by rotating the 2D cross-section along the droplet axis. And thereby all the vortices would be perpendicular to the **X**-**Y** plane, which is inconsistent with results of 3D numerical simulations and our experimental measurement.

Experimental 2D images captured at different angles were able to provide some clues on the 3D structure of the vortex flow. The difference of flow field between two separate meridian planes represents that 3D vortex flow is not strictly axisymmetric (Chang and Veleo, 2006). Numerical simulations of half-zone Marangoni convection by Lappa

(2003) obtained 3D velocity fields of a few planes parallel to the **X-Y** plane at different depths. The flow field showed a series of concentric iso-velocity contour lines were obtained in the planes based on axisymmetry assumption and simplified initial and boundary conditions, with uniform velocity distributions along each contour. The results explicitly confirmed the existence of vortex flow in all three planes (i.e., **X-Y**, **Y-Z**, **X-Z**). Similar results are obtained in our 3D reconstructed velocity field, with an evident vortex in the flow region near the droplet edge (Fig. 4.5). A single particle trajectory in Fig. 4.6 exhibits ring-like motions in projections of all three planes, indicating a 3D vortex flow in space. Despite the similarity of vortex flow with numerical simulations, experimental results such as velocity gradient of moving particles in **X-Y** projection (Fig. 4.5 and 4.6) indicate an asymmetric vortex flow in a droplet interior flow. Therefore the internal circulation in the droplet is more complex in reality. Neither 2D experimental results nor 3D numerical simulations are sufficient to study droplet internal circulation. Volumetric time-resolved measurement is a necessity for analysis of the complex flow pattern in the presence of Marangoni effects.

Geometric aspect ratios and exterior thermal conditions are known as factors affecting Marangoni convection. Further investigations should focus on the Marangoni effects under different conditions as well as influence of other force-induced convections. 3D experiment studies in droplet internal flow would also be used to visualize the whole field of view in the droplet with proper cameras and map other internal flow fields such as droplet drying process for DNA or protein microarraying.

References:

Abramchuk SS, Khokhlov AR, IwatakiT, Oana H and Yoshikawa K (2001) Direct observation of DNA molecules in a convection flow of a drying droplet. *Europhys Lett* 55: 294–300.

Baek SJ and Lee SJ (1996) A new two-frame particle tracking algorithm using match probability. *Exp Fluids* 22:23-32.

Chang ST and Velev OD (2006) Evaporation-induced particle microseparations inside droplets floating on a chip. *Langmuir* 22: 1459-1468.

Dwyer HA, Shaw BD (2001) Marangoni and stability studies on fiber-supported methanol droplets evaporating in reduced gravity. *Combust Sci Tech* 162(1): 331-346.

Hegseth J, Rashidnia N, and Chai A (1996) Natural convection in droplet evaporation *Physical Review E* 54 (2): 1640-1644.

Jing J et al. (1998) Automated high resolution optical mapping using arrayed, fluid-fixed DNA molecules. *Proc Natl Acad Sci USA* 95: 8046–51.

Kang HK, Lee SJ, Lee CM, Kang IS (2004) Quantitative visualization of flow inside an evaporating droplet using the ray tracing method. *Meas Sci Technol* 15:1104-1112.

Labonté G (1999) A new neural network for particle-tracking velocimetry. *Exp Fluids* 26, 340-346

Lappa M (2003) Three-dimensional numerical simulation of Marangoni flow instabilities in floating zones laterally heated by an equatorial ring. *Phys Fluids* 15: 776-789.

Pereira F, Stüer H, Castaño-Graff E, Gharib M (2006) Two-frame 3D particle tracking. *Meas Sci Technol* 17:1680-1692.

Savino R, Paterna D, and Favaloro, N (2002) Buoyancy and Marangoni effects in an evaporating drop. *J Thermo Heat Transfer* 16 (4): 562-574.

Shih AT and Megaridis CM (1996) Thermocapillary Flow Effects on Convective Droplet Evaporation. *Inter J Heat Mass Tran*s 39(2): 247–257.

Uno K, Hayashi K, Hayashi T, Ito K and Kitano H (1998) Particle adsorption in evaporating droplets of polymer latex dispersions on hydrophilic and hydrophobic surfaces *Colloid Poly. Sci* 276: 810–815.

Wegener M, Fevre M, Wang Z, Paschedag AR, and Kraume M (2007) Marangoni convection in single drop flow: experimental investigations and 3D-simulations. *6th Inter Conference on Multiphase Flow (ICMF)* Leipzig, Germany

Chapter 5

3D real-time imaging of cardiac cell motions in embryonic zebrafish*

---

* Please note that scale bars in supplemental movies of defocusing images represent 30 µm.

5.1 Introduction

Non-invasive three-dimensional real-time imaging of embryonic zebrafish cardiovascular cell motions is a critical need for understanding effects of biomechanics on developmental biology. Three significant requirements have to be met to ensure proper imaging in this highly dynamic organ. Appropriate tracers at micron or even submicron scale with neutral weight density have to be introduced to label the heart wall or cardiovascular blood flow. Date acquiring hardware such as high-speed camera working under extreme low light condition with sufficient temporal and spatial resolution is a necessity to adequately record cardiac cell motions. Powerful software is to be adopted to accurately reconstruct the 3D volume based on the images taken by the hardware.

Conventional 3D imaging approaches based on scanning a volume at various depths are not suitable for quantitative analysis of the zebrafish heart due to the lack of real-time information. Mirco DDPIV system has been validated for volumetric quantitative visualization in the regime of fast motions (see Chapter 4 for details). In this research the micro DDPIV technique is applied for 3D real-time imaging of zebrafish cardiac cell motions including blood flow and heart wall motions. Yellow-green fluorescent microspheres with 1 μm or 500 nm in diameter were utilized as the tracers. We should address here that some transgenic zebrafish embryos have been derived expressing fluorescent proteins (e.g., GFP, RFP, etc.) labelling red blood cells (i.e., Tg(gata1: GFP)) or cardiac myocytes (i.e., Tg(clmc2: GFP)). However, the emitted fluorescent light is too dim to capture in micro DDPIV system. External tracers were therefore introduced into the heart through the blood stream, providing sufficient contrast and brightness in thick tissues. High-speed cameras working with imaging intensifier were used to acquire fast DDPIV images under low light condition because the aperture mask blocks a large amount of emitted light. PTV was adopted to reconstruct the 3D motions by tracking movements of tracer particles in the field of view.

5.2 Materials and Methods

5.2.1 Target preparation and calibration

Calibration targets were prepared in the identical environment as the working condition to avoid potential discrepancy due to different optical indices of media. A cover glass instead of the previous used Petri dish was selected as the substrate to allow for more optical accessibility as well as enhance working distance owing to its small thickness. 1-µm or 500-nm yellow-green fluorescent microspheres (Molecular ProbesTM, FluoSpheres, USA) were initially diluted into preheated 1% ultra low melting temperature agarose (Sigma-Aldrich, USA) in 30% Danieau solution. One small droplet of the diluted solution was placed on a 24x50mm^2 cover glass. We then put another cover glass over the droplet, and pressed the two cover glasses tightly, allowing the agarose solution to cool within minutes. Afterwards, fluorescent targets were spread over the cover glasses. A similar calibration procedure was then carried out to resolve the significant parameters for volumetric reconstruction.

5.2.2 Embryo preparation and microinjection

Wild type zebrafish embryos were raised at 28.5°C and cultured in egg water or 30% Danieau solution, following the standard procedure (Westerfield, 2000). 0.03% PTU was added into the solution to prevent pigment from forming all over the body. Test embryos underwent further preparation at 32-56 hpf (hours post fertilization) by dechorionation, anaesthetization with 0.02% tricaine in 30% Danieau solution.

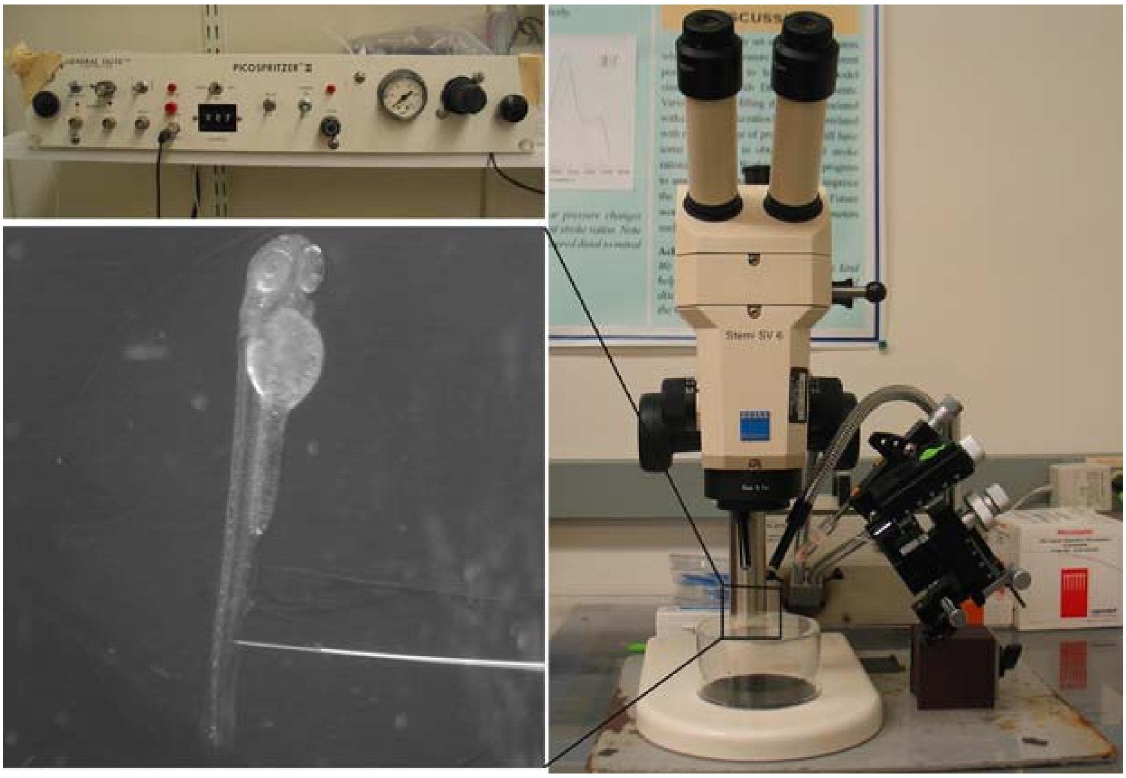

Figure 5.1. Experimental setup for zebrafish embryo microinjection with a sample image of a glass needle at the embryo tail.

The test embryos were transferred to 1% melted agarose, and then pipetted in a drop of agarose on a chilled cover glass to facilitate particles injection. The orientation of the embryos was manually adjusted to expose the blood vessels in the tail, through the use of a small capillary tube. Embryos were appropriately positioned and mounted on the cover glass within minutes when the agarose hardened. Fluidized yellow-green fluorescent microspheres were loaded through a microloader into a glass injection needle with approximately 10-µm tip, which was connected with a Pico-Spritzer assembly (General Valve PLC-100). The test embryo was placed underneath a Zeiss Stemi SV 6 dissecting microscope for observation. The injection needle was positioned by a 6-direction micromanipulator to the tail of the embryo (Fig. 5.1). The needle tip then penetrated the skin in order to inject the tracer particles into the blood vessel. It should be addressed here that because direct injection of particles into the developing heart may cause serious damage to the cardiac muscle and impact the physics of normal cardiac cell motions, microinjection was performed at blood vessels in the tail of the embryo to minimize the potential influence. Tracer particles then entered the heart through the circulatory system. The rate of successful injections suitable for defocusing imaging is about 25% (14 successes out of 55 injections) at 1 dpf (day post fertilization) and about 50% (31 successes out of 60 injections). Fig. 5.1 shows the microinjection setup as well as the position of the injection needle on the embryo.

5.3 In vivo imaging of cardiac cell motions in zebrafish

The zebrafish embryonic heart is composed of two chambers, i.e., the atrium and the ventricle. Each chamber is about 80 µm in diameter and 100 µm longitudinally. A 32-hpf heart is a straight tube, with a two-part heart-beat indicating the formation of two chambers. At 48 hpf, the heart tube bends to separate the two chambers.

A very small volume (e.g., picoliters) of fluorescent microspheres was injected into the blood stream of a zebrafish embryo immobilized by a drop of 1% agarose gel at 32-59 hours post fertilization (hpf) (see Section 5.2.2). The tracer particles then moved with the blood flow along the circulation system to the heart. The same modified microscopic imaging setup with a 20X objective and a 3-pinhole aperture mask (see Section 3.2) was used for zebrafish imaging except that the substrate was changed to a cover glass. A continuous 488nm laser beam was used for fluorescence excitation. The injected test embryos were transferred to the microscope and adjusted by the translational stage such that all tracer particles labeling the volume of interest were located under the focal plane and closer to the objective, i.e., all defocused patterns were in the same direction. Defocused image patterns of in vivo cardiac cell motions were recorded by the high-speed camera at up to 250 fps (Photron, APX Ultima; or Dantec, Nanoscience III with a grey-tube image intensifier built by Professor Scott Fraser at Biological Imaging Center, Caltech). Because the embryos were directly exposed to the laser beam, image acquiring only took a few seconds to avoid heart rate increase in the embryo due to overheat.

It has been observed that injected polystyrene microspheres are likely to aggregate or to be trapped by the walls of blood vessels within minutes after injection. In heart-wall motions imaging experiments, the microspheres trapped in the heart were used as tracers to describe heart-wall motions. However, particle trapping by heart walls may significantly affect their ability to function optimally as cardiovascular flow tracers. In blood flow imaging experiments, the test zebrafish embryo was immediately moved to the modified microscopic setup for imaging after a successful injection.

Although microinjection was carefully performed, some particles already adhered to the surrounding tissues outside of the heart, generating a non-uniform background in the images. Therefore images were processed prior to identifying the particles by their self-similar triangular image patterns. Fig. 5.2 shows a sample of the image processing procedure. A single image frame (Fig. 5.2(a)) among a raw image sequence showing blood flow in the yolk sac of a 32-hpf embryo included both particles in the blood stream and those trapped by the tissues. Fluorescent image patterns of the particles on the tissues were considered as the background and needed to be separated from the particles of interest in the blood in order to measure the flow velocities. Since the surrounding tissues were stationary during the experiment, the background particles existed in the same positions of every frame among an image sequence, while the particles moving in the blood were present in different locations. Therefore the average intensity of the entire sequence only contains the background (Fig. 5.2(b)), which was initially calculated using ImageJ (National Institutes of Health, USA) and was then subtracted from every single image frame. After background removal, an image frame only contains signals of particles in the blood stream. The typical signal-to-noise ratio of the recorded images was 12.6 dB. Particle image detection in our experiments was then performed, following the procedures of Pereira et al.(2002): low-pass filtering, particle subpixel detection, particle 2D Gaussian modeling and noise removal were performed to further improve the image quality, followed by triangle pattern matching to find the 3D coordinates of the tracer particles.

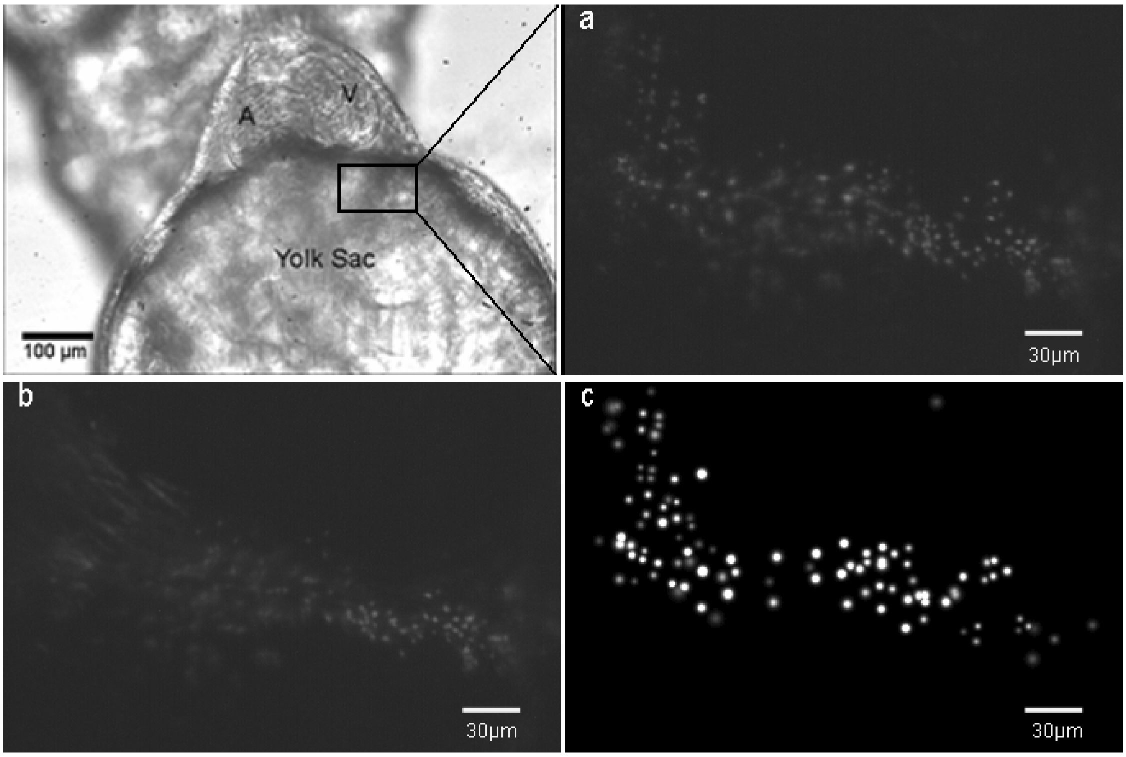

Figure 5.2. Particle image processing. (a) Defocusing images acquired in experiments. (b) Background due to microspheres trapped by surrounding tissues. (c) Processed images after background removal, lowpass filtering, particle detection, 2-D Gaussian model and noise removal. (Adapted from Lu et al., J Biomed Opt)

5.4 Results

5.4.1 Blood flow in the yolk sac

The complex 3D velocity field is able to be resolved by PTV based on the reconstructed particle positions. Fig. 5.3 exhibits the flow field in the yolk sac of a 48-hpf embryo with blood moving from right to left. The region of interest and a sample of the original DDPIV image of the tracer particles are shown in Fig. 5.2. The blood in the yolk sac is seen to be moving first upward, then following a downward direction as the yolk sac is approximately spherical. Flow velocities accelerate as blood enters the yolk sac and decelerate when blood flows to the heart.

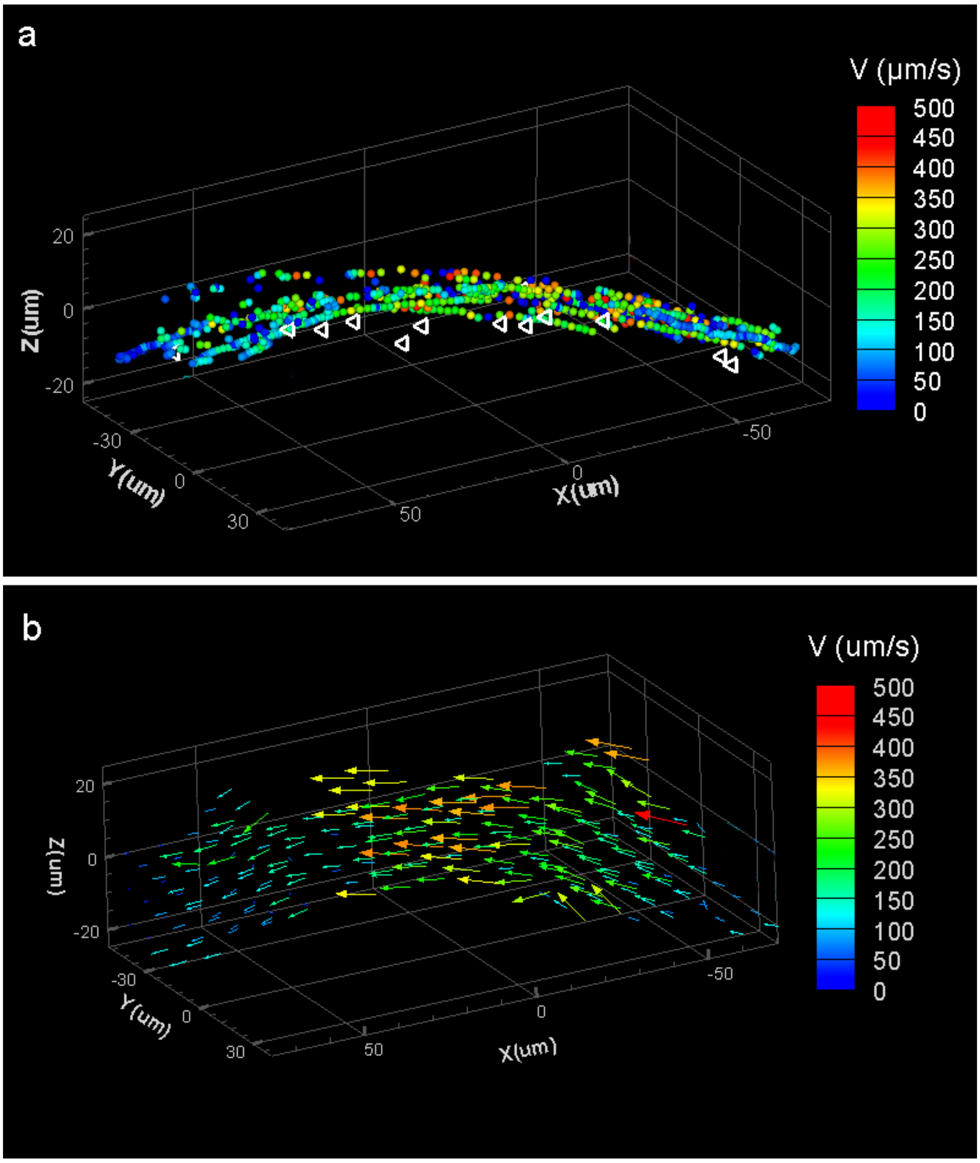

Figure 5.3. (a) 3D positions of tracer particles in the yolk sac of a 48-hpf embryo.

Spheres represent particles moving in the blood. The white left triangles represent spatial positions of particles adhered to the tissues. (b) Computed mean velocity field of blood flow in the yolk sac. The velocity magnitudes are color coded.

Positions of the static particles trapped in the tissue which were considered as the background in Fig. 5.2(b) were resolved and superimposed to the reconstructed 3D blood flow field. It is evident in Fig 5.3(a) that the blood flow trajectories strictly follow the spatial structure of the tissues underneath, which is labeled by the adhered microspheres. The mean velocity field can be computed since the blood flow in the yolk sac is approximately steady, with an average velocity of about 50 µm/s in the inflow and outflow regions and about 250 µm/s in the main region of the yolk sac.

5.4.2 Blood flow in a 32-hpf heart tube with partially labeled heart wall

Cell motions inside the heart were imaged with the aid of injected particles as well. Fig. 5.4 exhibits a series of defocusing image patterns forming downwards triangles and reconstructed 3D velocity fields in a 32-hpf heart tube at a few time instances. Blood flow entered the heart from the right to the left. Two injected particles were trapped in the atrium and the ventricle, respectively. While paths of the particles labeling blood flow in the atrium within a cardiac cycle is evident in the reconstructed image, trajectories of tracer particles trapped in the wall of the atrium and the ventricle of the embryo are easier to identify as the heart wall motions always follow a loop. The loop centered at **Y**=25 µm represents the particle in the ventricle, and the one at Y=-50 µm indicates the particle in the atrium.

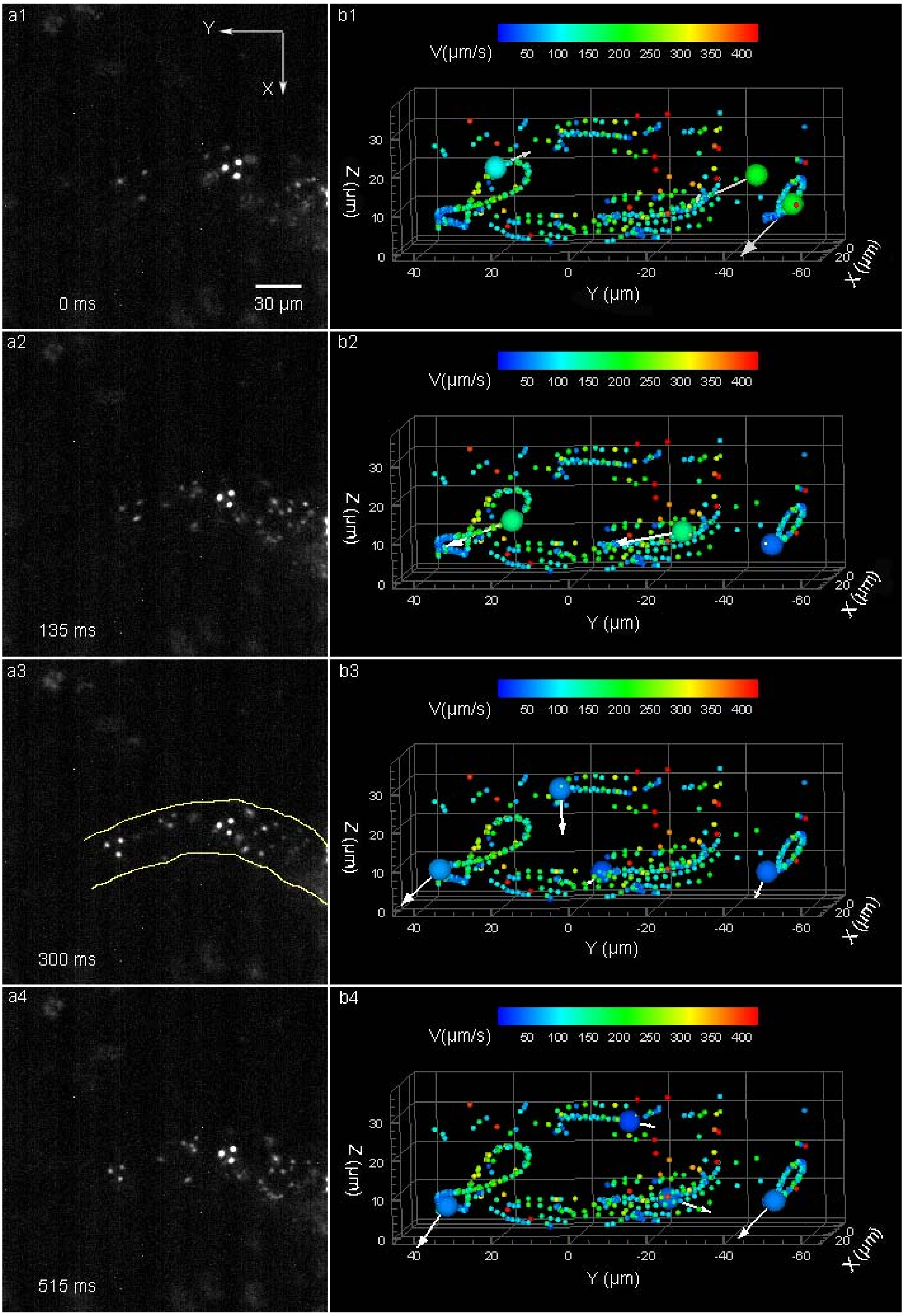
a1
Y
X
30 µm
0 ms
b1
V(µm/s)
50 100 150 200 250 300 350 400
Z (µm)
0 10 20 30
Y (µm)
40 20 0 -20 -40 -60
X (µm)
0 20
a2
135 ms
b2
a3
300 ms
b3
a4
515 ms
b4

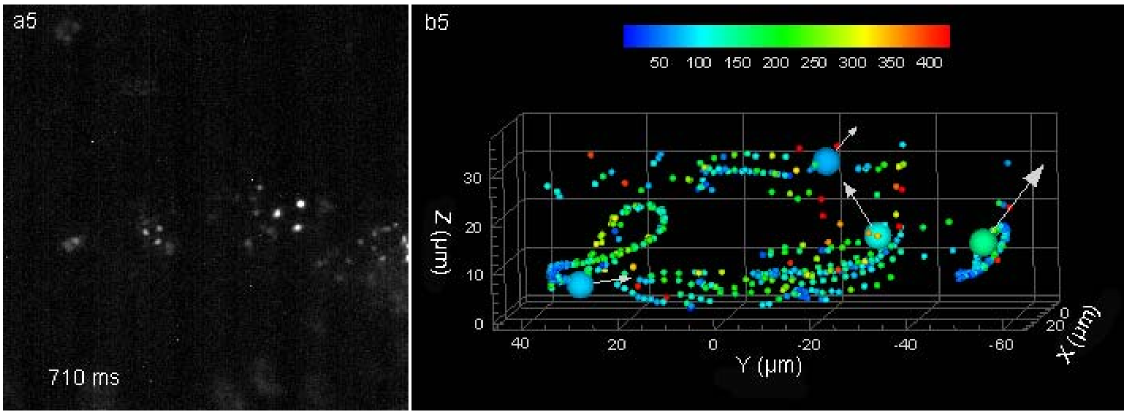

Figure 5.4. 3D PTV results of cardiovascular flow and heart-wall motions. (a) Defocusing images of the tracer particles in the blood and adhered to the heart wall during a cardiac cycle. The two bright image triplets originated from the tracer particles of interest in the heart wall, with the ventricle on the left side and the atrium on the right. Images were recorded at 60 fps. (b) Trajectory of the tracer particle inside the heart tube with the two loops representing particles trapped in the atrium and the ventricle, respectively. The spheres stand for positions of the injected tracer particles, with colors representing velocity magnitudes and vector arrows indicating velocity directions. The big spheres in each image indicate the particle position at the corresponding time instance. The yellow line in a3 shows the border of the heart tube.

Three-dimensional positions of the particles within a cardiac cycle demonstrated the phase difference between heart-wall motion and blood flow as well as difference between the atrium wall and the ventricle wall in a beating heart. One would find that both trapped particles are in the lower side of radial direction (**Z**) in the heart tube. Therefore upward motion of trapped particles indicates wall contraction and downward motions represent expansion. At t=0 ms, the blood started to enter the heart while the atrium started to expand and the ventricle contracted. The ventricular part of the heart tube then expanded as the blood moved further into the atrium (t=135 ms). Then the ventricular wall initiated contraction to allow inflow to the ventricle at t= 300 ms. Retrograde flow appeared in the atrium while the atrial wall stayed expanded (Fig. 5.4(b4)). The atrium and the ventricle started contraction when the retrograde flow tended to stop at t=710 ms. It can be inferred from the velocity gradient along the trajectory loops of the trapped particles that the heart wall moved faster at smaller diameters. Actually the heart tube remained almost fully expanded (i.e., inactive) for about a half of the cardiac cycle (Fig. 5.4(b3)-(b5)).

The heart wall motions and blood flow during heart beating followed a suction pump mechanism as described by Forouhar et al. (2006). Further evidence of the pumping flow can be found in this experiment by tracking a single tracer particle in the blood within a few cardiac cycles. Fig. 5.5 shows the longitudinal positions of a few particles in the field of view. It can be observed that there is a particle in the blood moving back and forth in the atrium between the two particles adhered to the wall. By tracking the peak positions of the particle, one can find that it took about 4 beating cycles for that particle to be pumped into the ventricle. Details about particle motions throughout 5 cardiac cycles can be seen in Movie 1a (defocusing images) and Movie 1b (reconstructed images).

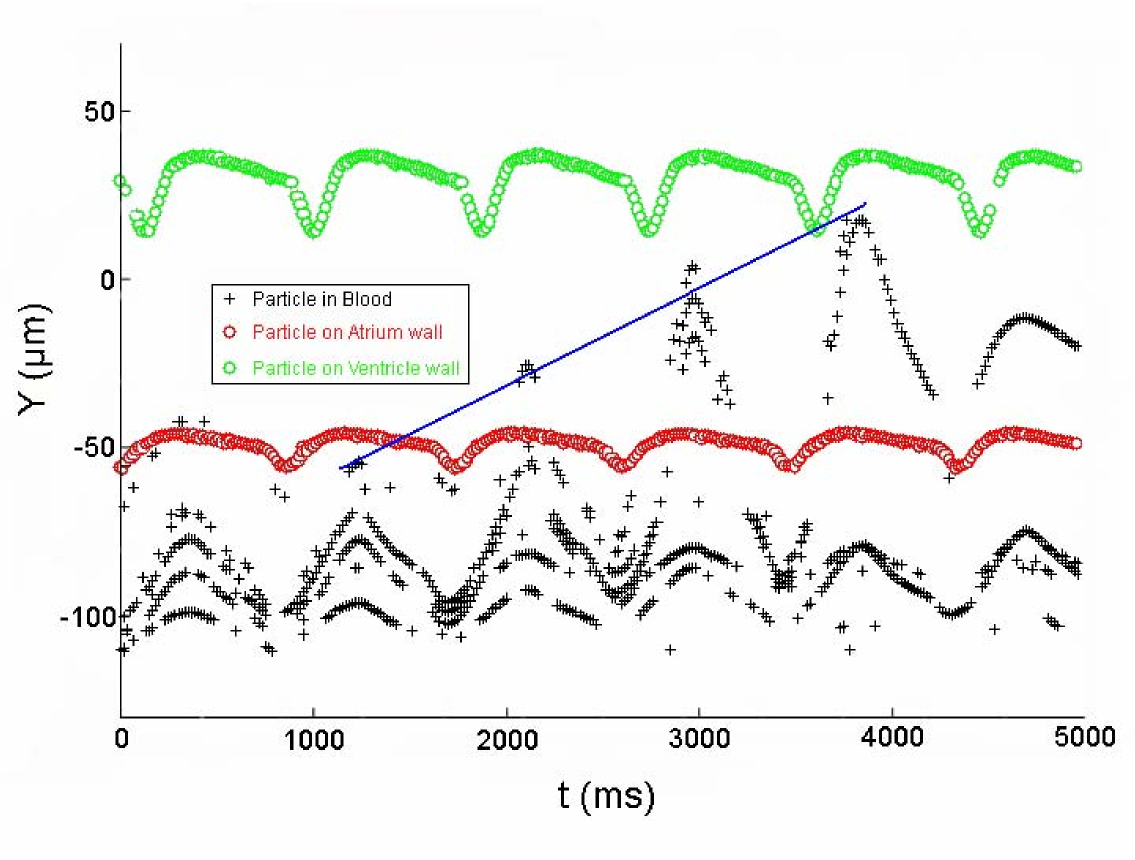

Figure 5.5. Y-location (longitudinal direction) of particles in the blood and in the heart wall within 6 cardiac cycles. The solid blue line links the peak position of a particle in the blood throughout 4 cycles.

One can also observe that the wall motion in the ventricle is more active and more complex than that in the atrium. Fig. 5.6 is the **Y**-**Z** and **X**-**Y** projections of tracer particles in the 32-hpf heart tube within a cardiac cycle. The **Y**-**Z** projection exhibits that the magnitude of the trajectory of the particle in the ventricular wall is much higher. And a bent heart tube is evident in the **X**-**Y** projection, which is a sign of the cardiac looping. Comparing the particle trajectories in the two projections, one can also observe that the early embryonic heart tube (32-hpf) motion during is mostly longitudinal (**Y**-direction) and radial (**Z**-direction), while circumferential movement is scarce. Therefore the early cardiac pumping mechanism is mainly composed of contractions in the heart wall, generating wall thickness (**Z**-direction) and length (**Y**-direction) shortening with little torsion along the heart tube.

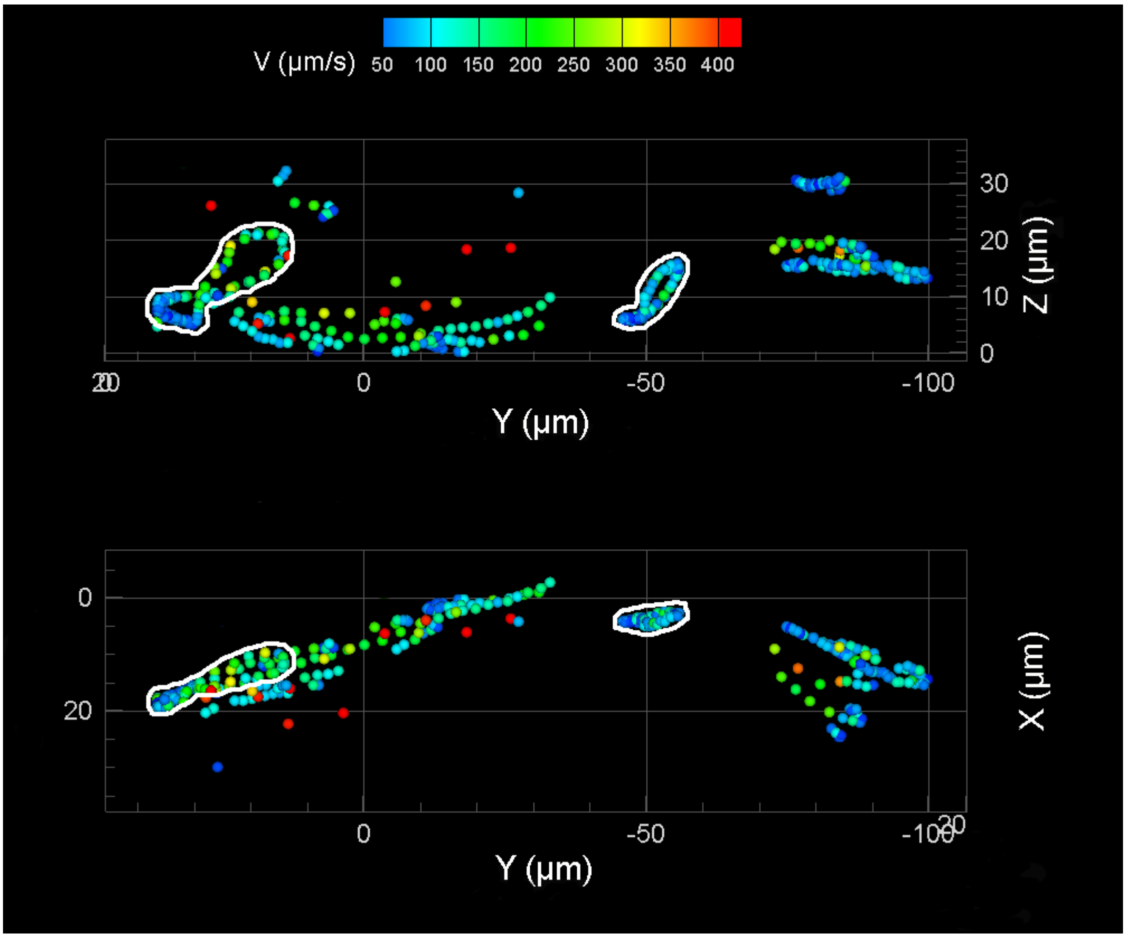

Figure 5.6. Y-Z and X-Y projections of tracer particles within a cardiac cycle in the 32-hpf heart tube. The white lines enclose trajectories of particles in the wall.

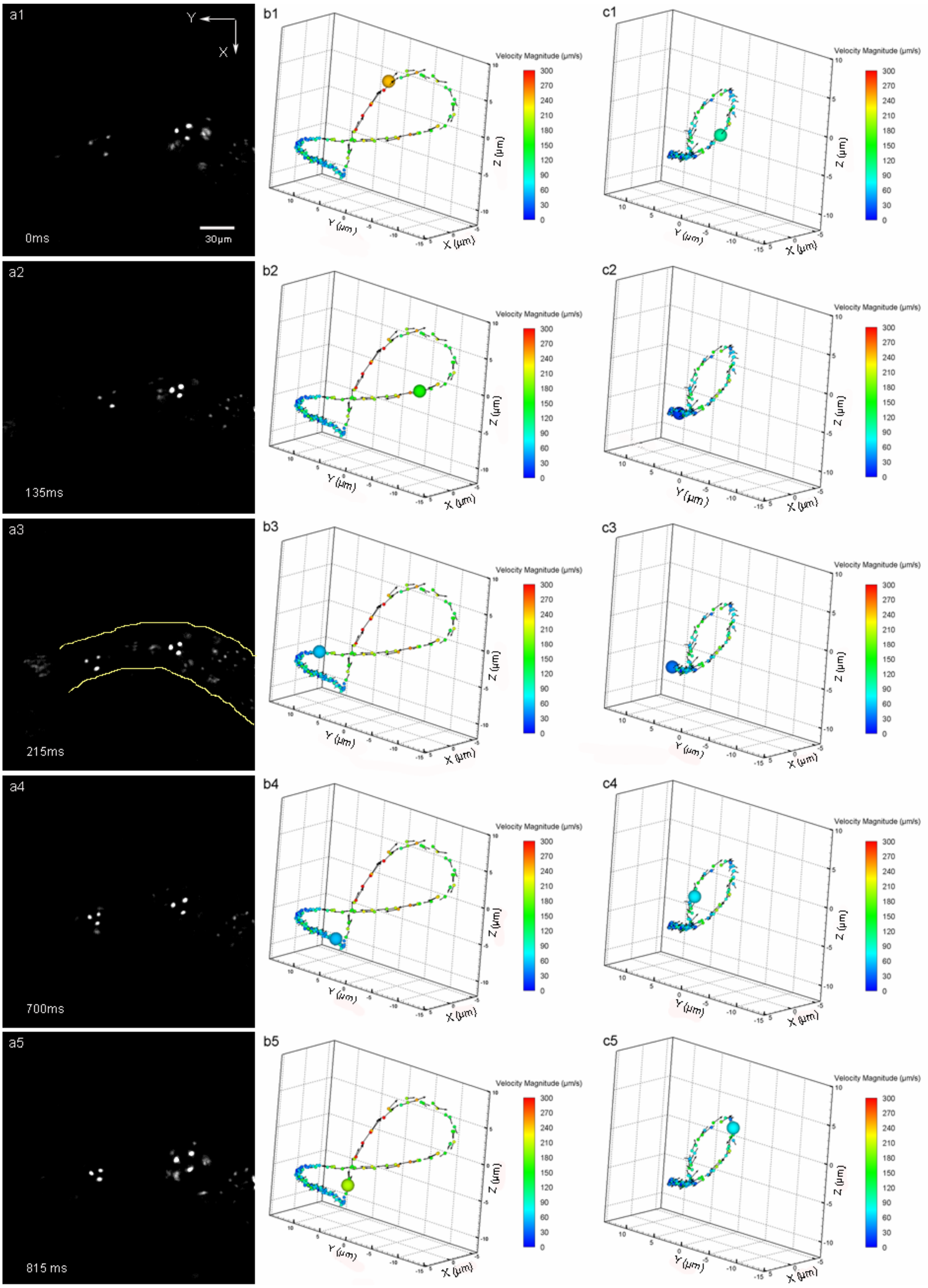

Figure 5.7. Trajectories of heart wall motions. Z-coordinates are exaggerated to help

describe the radial displacement.

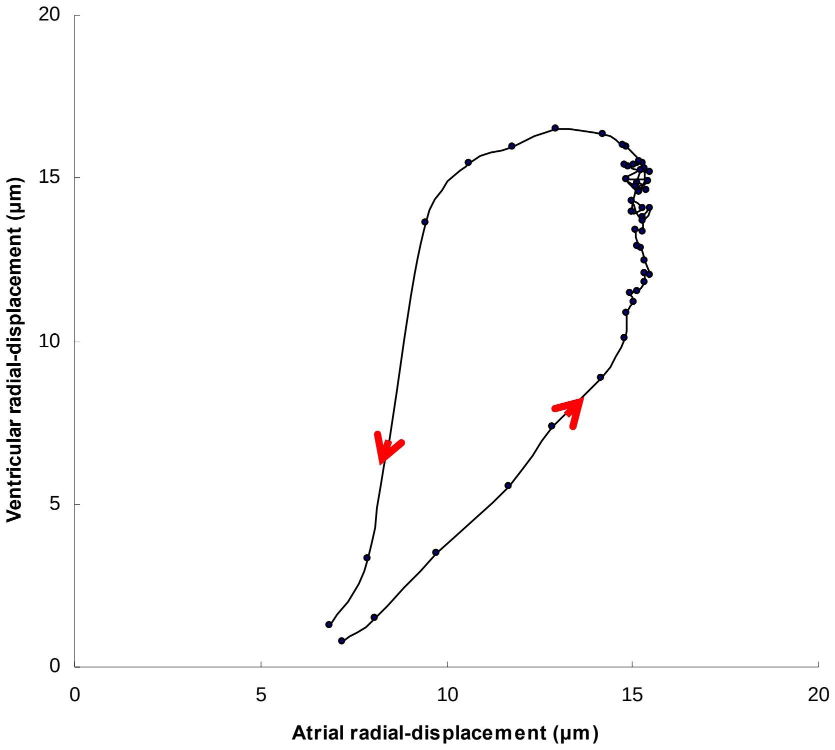

Figure 5.8. Particle radial displacements (ventricle vs atrium) throughout a cardiac cycle at 32 hpf.

Phase delay in the wall motions is more evident if the trajectories of the particles in the wall throughout a cardiac cycle are isolated. Radial deformations are clearly visible in Fig. 5.7, where **Z**-coordinates are exaggerated. We further isolate the radial displacements of the two particles in the wall throughout a cardiac cycle and plot them versus each other, where positive directions indicate diameter increases (Fig. 5.8). Radial displacement in the ventricle wall is more active than that in the atrium wall. Inactive periods in both chambers are also observed in the loop, where the atrium remains fully expanded (radial displacement= 15 μm) in late ventricular diastole when ventricle diameter increases gradually to its maximum, and then atrium diameter decreases rapidly with radial displacement changing from 15 μm to 10 μm while the ventricle remains constant in early systole. The phenomenon that one chamber is active while the other one remains inactive at some time instances provides an evidence of a suction wave traveling along the heart tube, generating a phase delay in the motions of different chambers.

5.4.3 48-hpf heart wall motions

The zebrafish heart chambers become more prominent with the embryo’s rapid development. The dynamic motion of the entire heart wall is able to be mapped with several injected particles adhered to the endocardium. Fig. 5.9 shows the movements of a 48-hpf heart wall with both chambers labeled by fluorescent particles and the corresponding reconstructed 3D structure with particle velocities. The heart rate is about 2.2 Hz. And the recording rate of the camera is 125 fps. The mean velocity of the heart wall contraction is about 300 μm/s. The reconstructed 3D positions and velocities of the particles (Fig. 5.9(b)) demonstrated the phase difference between the contraction of the atrium and that of the ventricle during a complete cardiac cycle. At t=0 ms diastole initiated: the ventricle expansion started while the atrium remained relaxed. The atrium then started to contract with further expansion in the ventricle. At t=183 ms the contraction initiated in the ventricle and the atrium was expanding. Further atrium expansion and ventricle contraction were observed at t=334 ms. Complete motions of the adhered particles can be observed in Movie 2a (Defocusing images) and Movie 2b (Reconstructed velocity fields).

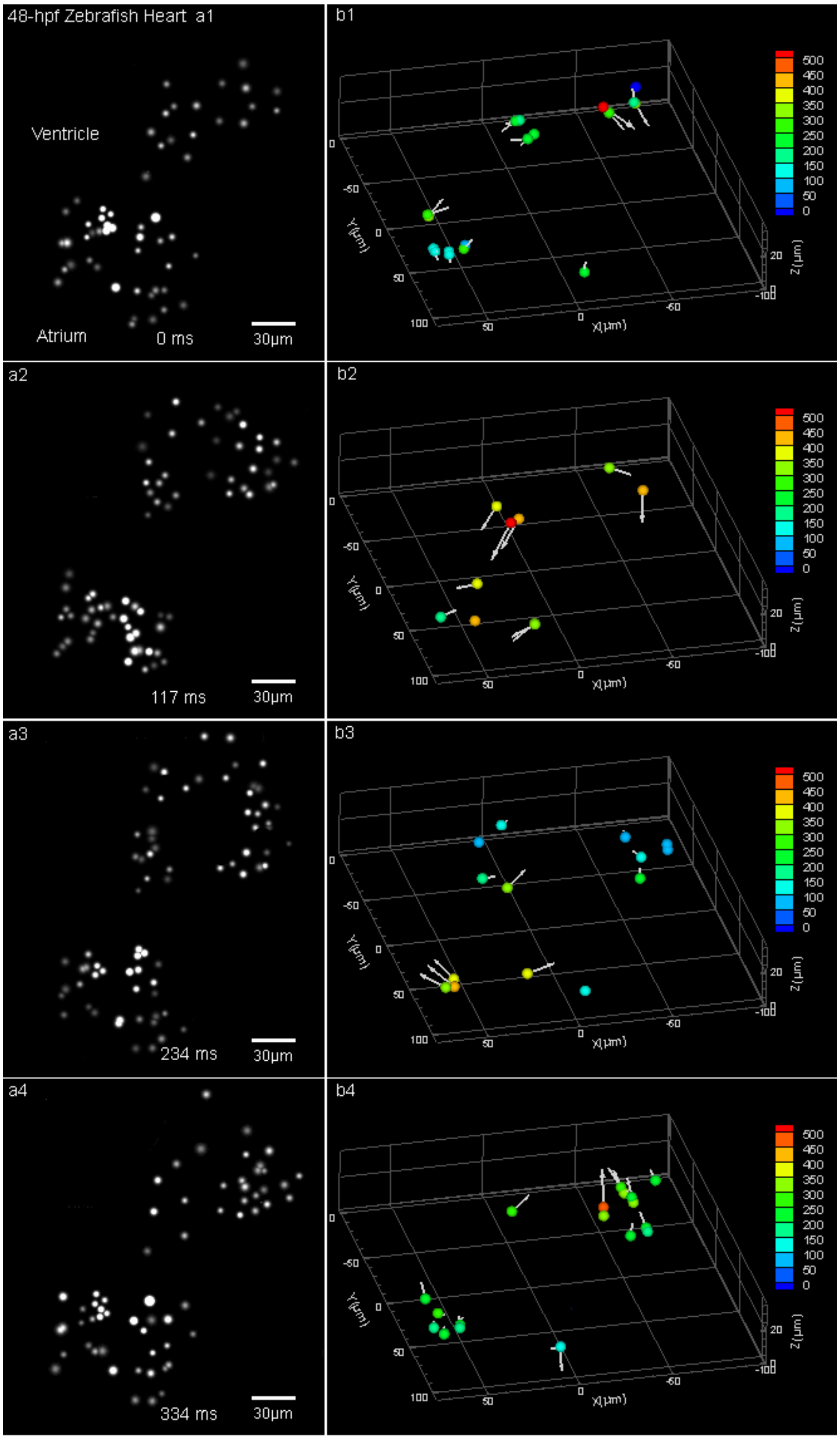

Figure 5.9. (a) A beating 48-hpf zebrafish heart labeled by injected tracer particles. Defocusing image patterns form upright triangles. (b) Reconstruction of the beating

ventricle at the corresponding time instance in (a). Velocities magnitudes are color coded and vector arrows represent velocity directions.

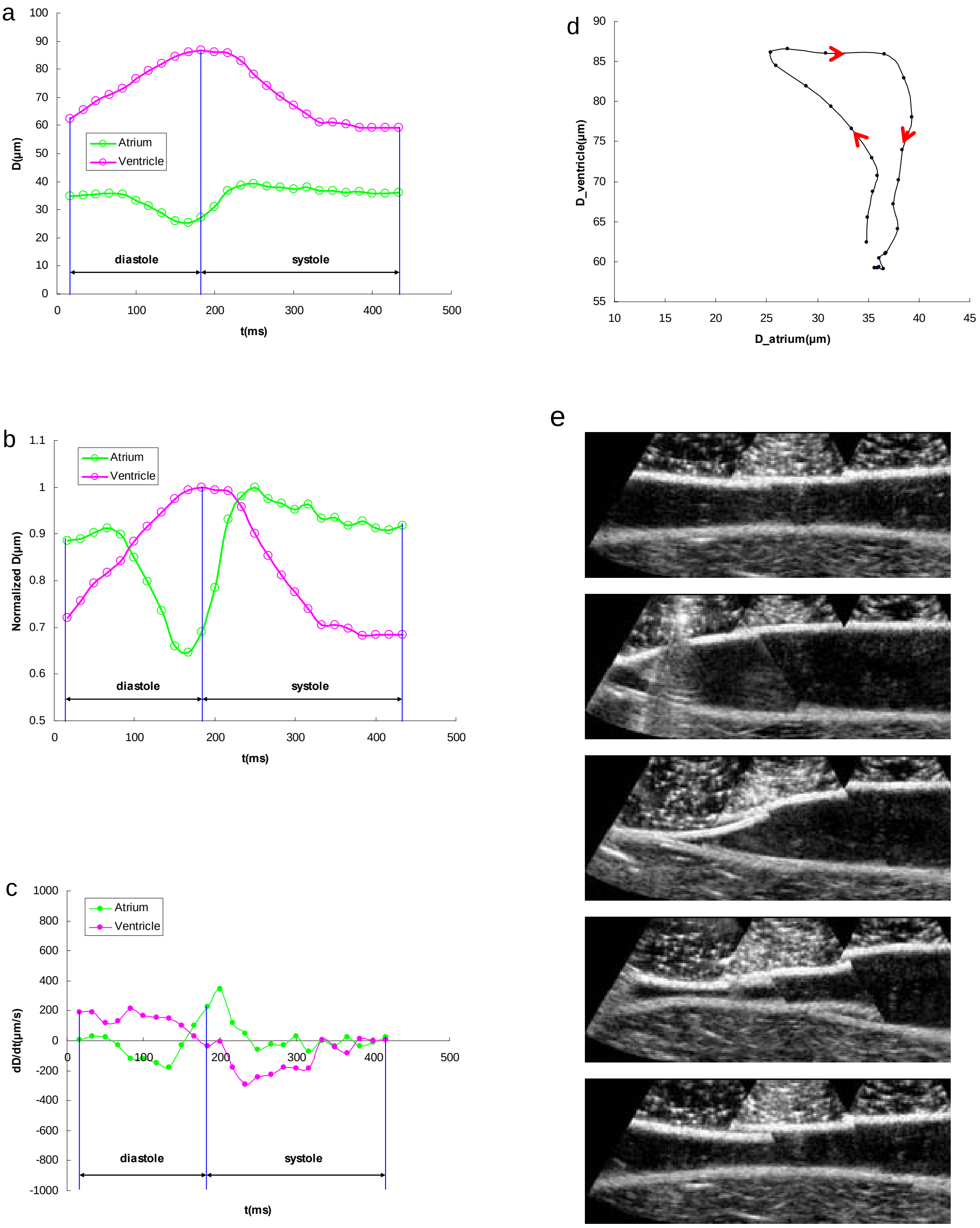

Figure 5.10. Diameter changes in the atrium and the ventricle during a cardiac cycle. (a) diamters vs time; (b) normalized diameters vs time; (c)diameter change rate vs time; (d)ventricle diameter vs atrium diameter; (e) ultrasound time series of a wave traveling in an elastic tube (Adapted from Hickerson's thesis, 2005).

Diameter changes in the heart chambers during a cardiac beating are measured by calculating the separation between two adequate particles located on either side of a chamber (Fig. 5.10). A wave propagating in the heart can be predicted from the diameter changes with time (Fig. 5.10(a), (b)) by comparing with the image sequence showing a wave in a tube (Fig. 5.10(e)), where the wave initiates in the left. In early diastole, the ventricle starts expansion as the result of a wave reflection while the atrium remains expanded. The atrium then initiates a new wave by starting contraction (t=83 ms); in the mean time the ventricle continues expansion. Shortly after the contraction completes in the atrium at t= 166 ms, the wave travels to the ventricle and initiates systole (t= 183 ms). At t= 250 ms the atrium reaches its maximal diameter and remains inactive until the next wave initiates in the following cycle. The ventricle contraction completes at t= 350 ms and remains its minimal diameter until systole ends. The atrium is seen to remain active for only about one third of the cardiac cycle while active diameter changes in the ventricle occurred during most time of the heart beat (i.e., about 350 ms), which predicts that a short period of wave initiation in the atrium produces a long period resonance in the ventricle including contraction due to forward wave and expansion due to reflected wave. Difference of active periods including phases and durations between the two chambers confirms the existence of a compression wave in the 48-hpf heart.

Changing rates of the diameters are calculated in Fig. 5.10 (c). The ventricular diameter changing rate decelerates towards zero in diastole. And it accelerates in early systole when contraction initiates, then decelerates again towards zero when the ventricle becomes inactive. The changing rate in the atrium accelerates when atrium contraction initiates in diastole, and decelerates towards zero when contraction completes. The rate accelerates again in late diastole and continues in early systole with the atrium expansion. It then decelerates towards zero when the atrium reaches the inactive state. Fig. 5.10 (d) clearly shows the inactive states in both chambers when the diameter remains constant.

5.4.4 Ventricular strain measurement in a 42-hpf heart

Knowledge of the ventricular wall deformation is a critical concern in cardiovascular research since many congenital heart diseases caused extensively malfunctions. Understanding of the mechanical function of a beating heart requires quantitative analysis of the regional deformation such as myocardial strain measurement. Besides many computational efforts utilized to model myocardial deformation, typical experimental approaches for measuring local strains in the myocardium include the employment of implanted markers or noninvasive imaging method such as cardiac magnetic resonance imaging (MRI) tagging. Waldman et al. (1985) performed the first effective 3D in vivo finite strain measurement by embedding beads in the epicardium of the canine left ventricle. MR tissue tagging was utilized to measure 3D myocardial fiber shortening (Rademarkers et al., 1994). However, providing sufficient temporal resolution remains a challenge in 3D MR tagging. Early embryonic zebrafish heart wall consists of endocardium and epicardium separated by cardiac jelly (Hu et al., 2000). Consistent transmural strain gradients have been found with greatest magnitudes at the endocardium. Whereas conventional optical or clinical imaging methods do not have 3D access to the endocardium deformation, here a simple endocardium strain measurement approach is developed based on the 3D real-time imaging system. Again, injected microspheres trapped in the zebrafish ventricular wall were adopted as tracers for endocardial strain measurement. Distances between two closely embedded tracer particles were measured throughout a cardiac cycle for calculation of 3D strains.

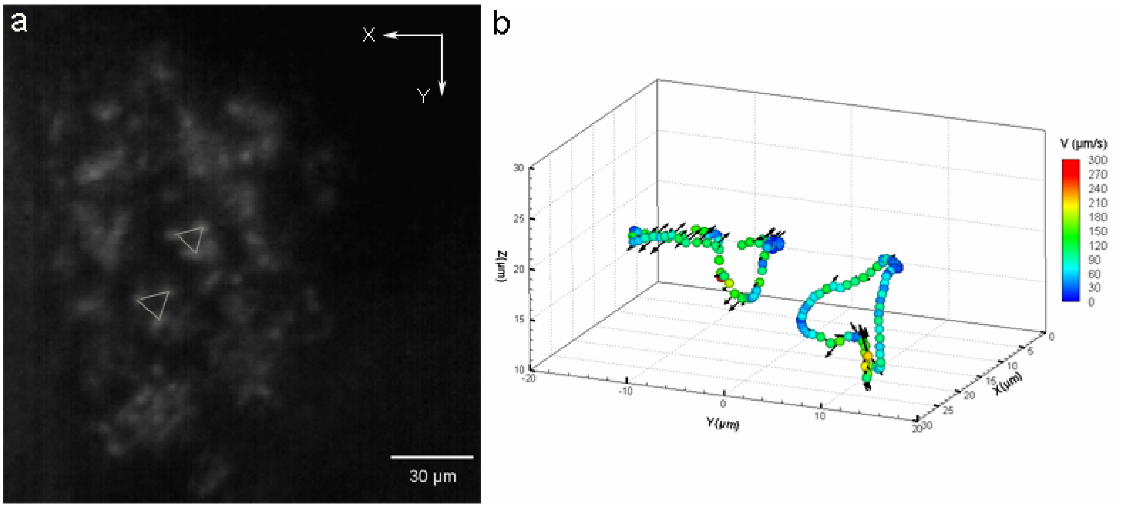

Figure 5.11. Defocusing image (a) and reconstructed trajectories (b) of two particles labeling the wall of a 42-hpf ventricle. Image patterns of the two selected particles are linked as triangles pointing downwards.

Fig. 5.11(a) shows a sample defocusing image of a 42-hpf ventricular wall labeled by tracer particles. The atrium is located above the ventricle in the image. Two adjacent particles in the mid-site are selected such that the **X** axis in the image represents circumferential direction, while **Y** axis representing longitudinal and **Z** axis representing radial direction. Particle trajectories throughout a cardiac cycle were tracked by utilizing the long-term tracking algorithm presented in Chapter 4. Because the myocardial deformation in the ventricle is three-dimensional and finite, nonlinear strain tensors are more appropriate to describe the wall motions than linear ones which neglect the second order terms. Green's strain tensors are employed as the measured 3D positions are Lagrangian coordinates (Fung, 1990).

$$E_{ij} = \frac{\partial u_i}{\partial X_j} + \frac{\partial u_j}{\partial X_i} + \frac{\partial u_k}{\partial X_i}\frac{\partial u_k}{\partial X_j} \qquad 5.1$$

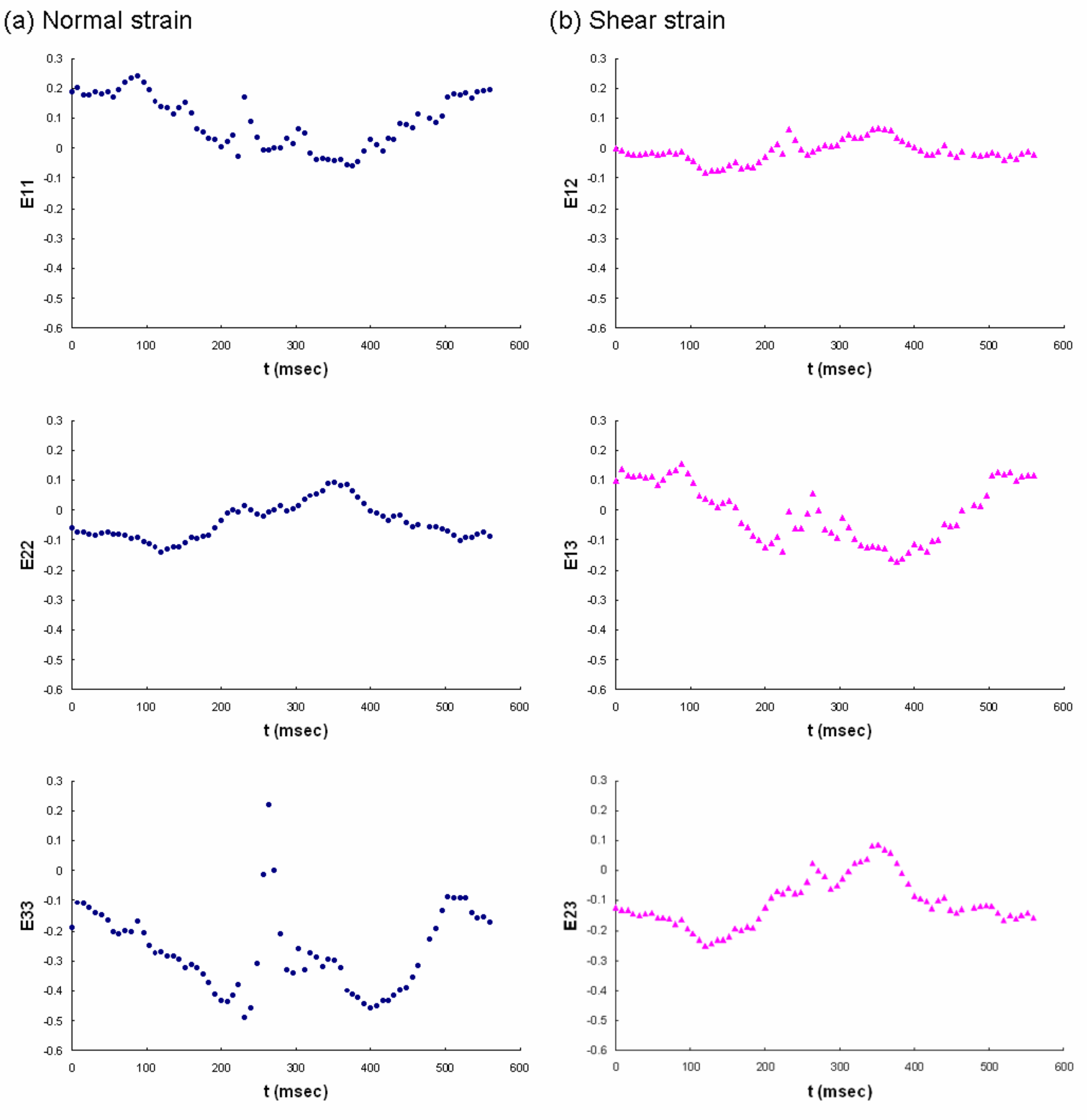

Figure 5.12. Time series of normal and shear strains relative to end-diastolic state in a 42-hpf ventricular myocardium during a cardiac cycle, where index 1 represents circumferential, index 2 for longitudinal and 3 for radial direction.

Assuming end diastole strains be zero, one is able to calculate the six components of the Green's strain tensor. The distance between the two particles at each reconstructed 3D space is calculated. Here the ***X*** in Eq. 5.1 is the particle distance at the end-diastolic state;

and ***u*** is the difference between the particle distance at a certain time instance and ***X***. Thereby the Green's stain tensor can be calculated at each time instance (see Fig. 5.12).

The time series started at end systole (t=0 ms), continued with end diastole at t=272 ms, and ended at end-systolic state. Radial strains (**E33**) are seen to be the most prominent one among all six tensor components. And Circumferential strain (**E11**) exceeds longitudinal strain (**E22**), which is consistent with epicardial strain measurements. It can be inferred heart deformation changes with the rapid cardiovascular development. In contrast to a 32-hpf heart tube where longitudinal and radial motions dominate, wall thickness and diameter changes occur more evidently in the 42-hpf ventricle. Among shear strains, the magnitudes of circumferential-radial (**E13**) and longitudinal-radial (**E23**) strains are higher than that of circumferntial-longitudinal strain (**E12**). Considering the three-dimensional coordinate system of the ventricle, the 42-hpf ventricle undergoes significant out-of-plane torsional deformations (i.e., **E13** and **E23**). Rapid clockwise twisting relative to the base is observed during inflation of the ventricle and then untwisting occurs during systole. Details of the three-dimensional torsion can be seen from both the raw image series (Movie 3a) and the reconstructed motions (Movie 3b), where sphere sizes represent depth positions.

5.4.5 Blood flow in a 59-hpf atrium

Cardiovascular blood velocity measurements are significant since blood flow involves in many cellular and subcellular events related to in vivo heart functions. Quantitative blood flow information in embryonic zebrafish heart is sparse due to the high flow velocity and complex 3D structures. Hove et al. (2003) measured 2D blood flow velocities in a 4.5 days post fertilization embryo with the aid of DPIV. Liebling et al. (2006) studied the 3D flow patterns of blood flow in the early embryonic zebrafish heart at eight different stages without direct velocity analysis. The present micro DDPIV system is implemented for quantitative study of blood flow in embryonic zebrafish atrium and ventricle.

Fig. 5.13 shows the velocity fields in the atrium of a 59-hpf zebrafish embryo during a cardiac cycle. Images were recorded at 250 fps. The measuring volume is 100X85X40 μm^3. An image sequence with a time interval of 48 ms describes the change of blood flow with the atrium contraction. The yolk sac (inflow track) lies in the right side of the image (negative **X**-axis), and the ventricle lies underneath the **X**-**Y** plane (negative **Z**-axis). The atrium initiated contraction at t=0 ms. Interestingly, a short period of inflow from the yolk sac appeared when the atrium underwent isovolumic contraction in early systole. We postulate that this is induced by the wave reflection near the sinus venous before the initiation of the next compression wave. Further contraction reduced the atrium volume and pumped the blood both into the ventricle and back to the yolk sac (t=48 and 96 ms). At the peak systole, few particles in the blood were visible, and the atrium reached its minimum volume (Fig. 5.13(d)). Then diastole started and rapid inflow entered from the yolk sac (Fig. 5.13(e)). Forward blood flow then filled the entire chamber with the expansion of the atrium wall, and the velocity gradually slowed down towards static (Fig. 5.13(f, g, h)). Velocity gradients of blood flow existed in the atrium during both diastole and systole, where the central region always had higher velocity than the near-wall region. Movie 4a and 4b show the dynamic motions of defocusing particle images (triangles pointing downwards) and reconstructed particle fields throughout a cardiac cycle, respectively.

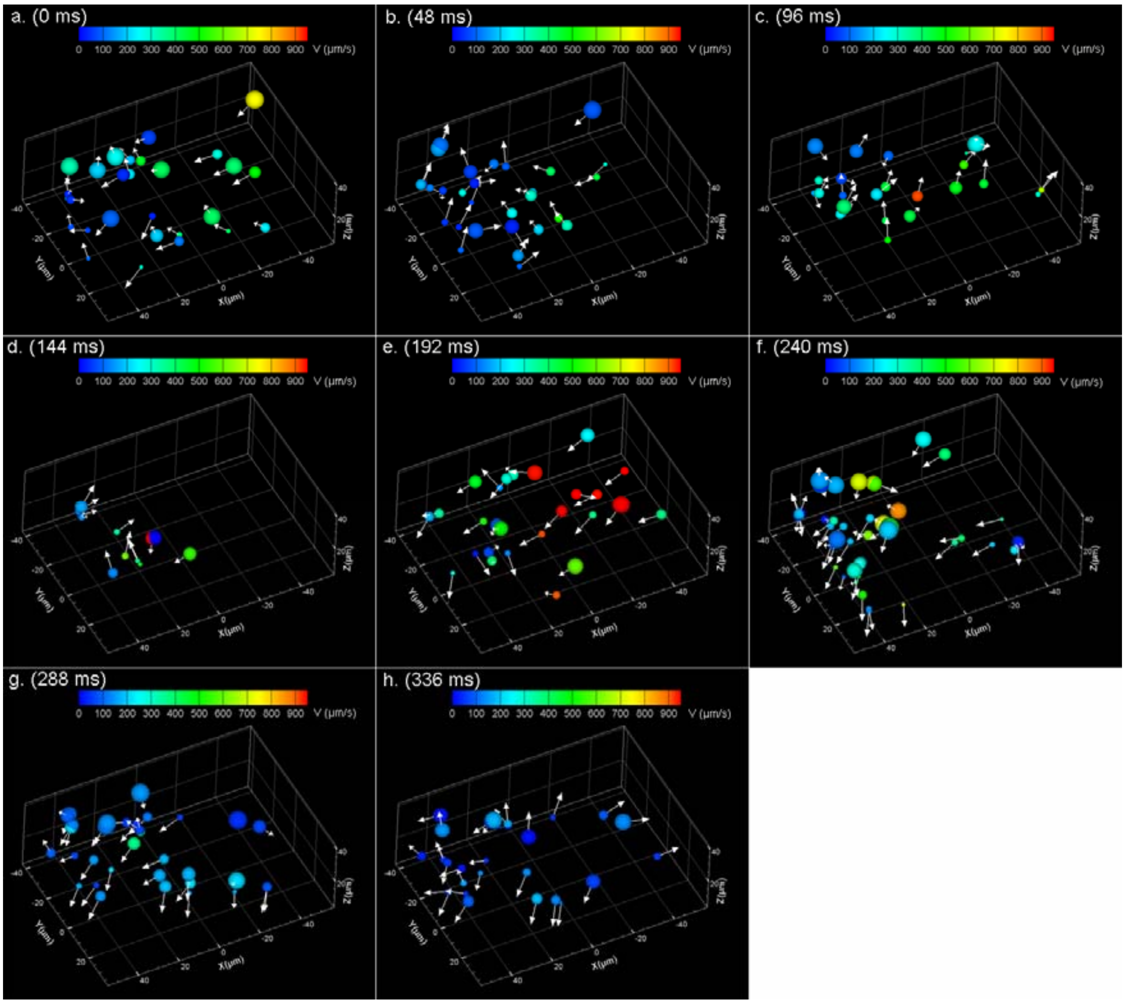

Figure 5.13. Particle velocity fields in a 59-hpf zebrafish atrium during a cardiac cycle. The spheres indicate particle positions. Velocity magnitudes are color coded. Particle sizes represent the depth location with larger spheres at higher Z-positions.

5.4.6 Blood flow in a 56-hpf ventricle

Blood flow in the ventricle of a 56-hpf zebrafish heart during a cardiac cycle was imaged as well as 3D reconstruction and velocity measurement. Duration of a cardiac cycle is 456 ms. Defocusing images were recorded at 250 fps. Fig. 5.14 shows the trajectories and velocity distribution of tracer particles moving with blood stream during systole, early diastole, and late diastole by superimposing the reconstructed image sequences at various time instances. The atrium was located in top-left corner, with the atrio-ventricular (A-V) cushion lying underneath the base plane of the image. And the blood flew out of the ventricle at the bottom-right corner. The depth of view in the reconstructed field is 35 µm. Flow velocities are color coded. And particle depths are size coded, with larger spheres indicating higher coordinates along **Z** direction.

One can see in Fig. 5.14(a) that in early systole particles near the heart wall followed a regrade-like loop, moving backwards to the atrium. With further contraction of the ventricle, rapid forward motions of the particles were established inside the entire chamber. It can also be inferred by following each trajectory that blood flow accelerates with the contraction of the ventricle, with the highest velocity existing in the flow exit. Duration of the systole is 236 ms. A short period of retrograde flow lasting about 72 ms appeared in early diastole (Fig. 5.14(b)). Particle velocities in the chamber center are higher than those near the wall. Fig. 5.14(c) exhibits flow trajectories during fast blood filling from the atrium.

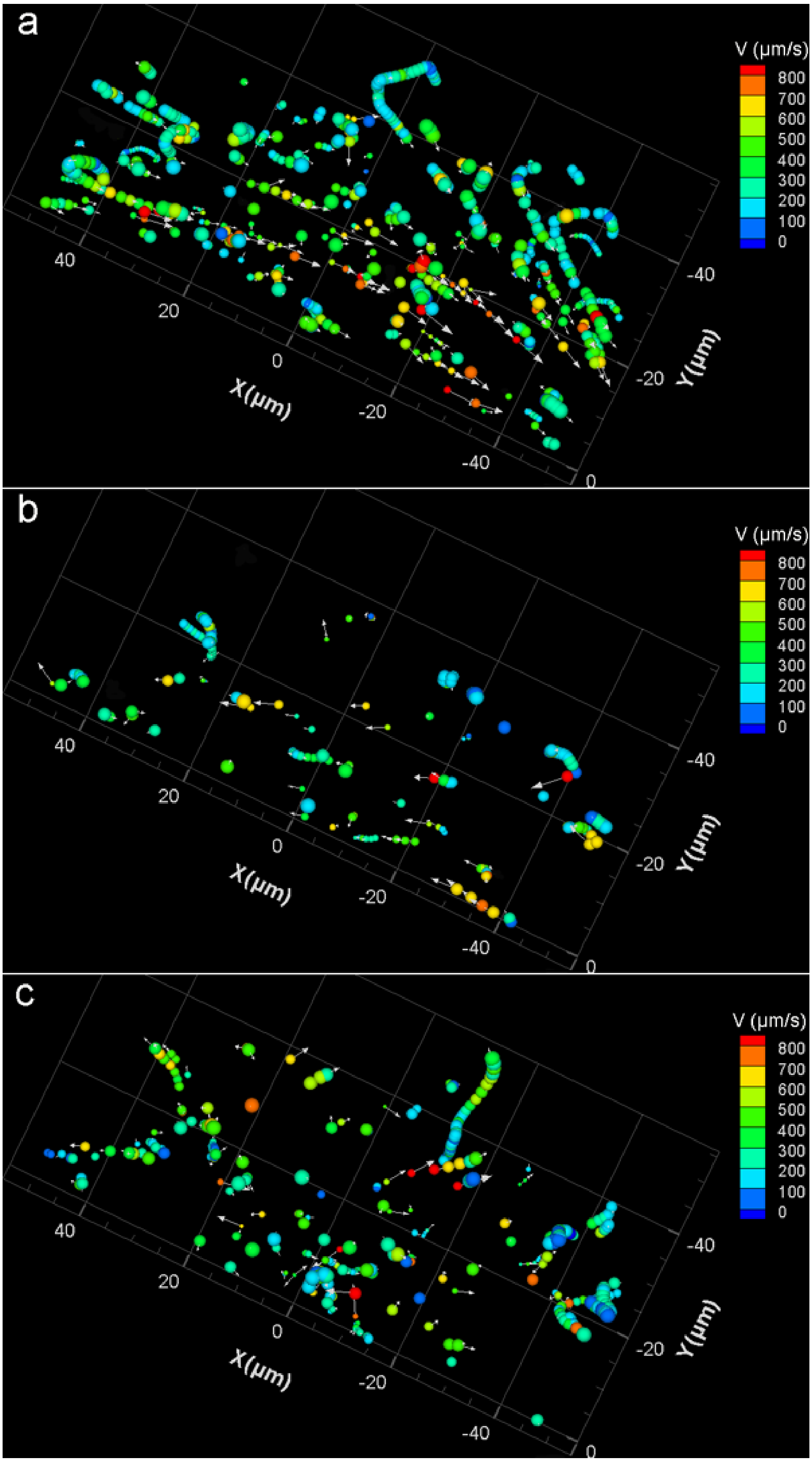
a
V (µm/s)
800
700
600
500
400
300
200
100
0
40
20
0
-20
-40
X(µm)
-40
-20
0
Y(µm)
b
V (µm/s)
800
700
600
500
400
300
200
100
0
40
20
0
-20
-40
X(µm)
-40
-20
0
Y(µm)
c
V (µm/s)
800
700
600
500
400
300
200
100
0
40
20
0
-20
-40
X(µm)
-40
-20
0
Y(µm)

Figure 5.14. Trajectories and velocity distribution of tracer particles in a 56-hpf ventricle during a cardiac cycle. (a) Trajectories during systole. (b) Trajectories of retrograde flow during early diastole. (c) Trajectories during late diastole showing blood filling from the atrium.

Instantaneous streamline fields at four typical time instances are computed by averaging velocity fields of identical phases over five cardiac cycles (Fig. 5.15). More detailed information about the blood flow is provided in the streamlines. In early systole (t=0 ms), particles near the wall moved backwards while blood in the center still moved forward. Forward flow existed in the entire chamber in the middle of systole (t=68 ms), moving out of the heart with the maximum velocity at the flow exit. Retrograde flow back to the atrium was evident in early diastole (Fig. 5.15(c)). Then blood filling from the atrium occurred in later diastole (t= 384 ms). A planar velocity result showing blood filling in a zebrafish ventricle has been reported in Hove et al. (2003)’s study, providing clues about blood flow in 3D space. The 2D flow field showed blood flowing upwards from the atrium ventricle lying at the bottom, and then expanding to the horizontal directions in the ventricle. Fig. 5.15(d) shows the details of 3D blood filling into the ventricle in a pattern like a burst of jet. The blood entered through the A-V cushion at the bottom, moved upwards into the ventricle, and then expanded along all directions to fill the chamber. Dynamic motions of blood flow during an entire cardiac cycle from early systole to end diastole are presented in Movie 5a (defocusing images) and 5b (reconstructed images).

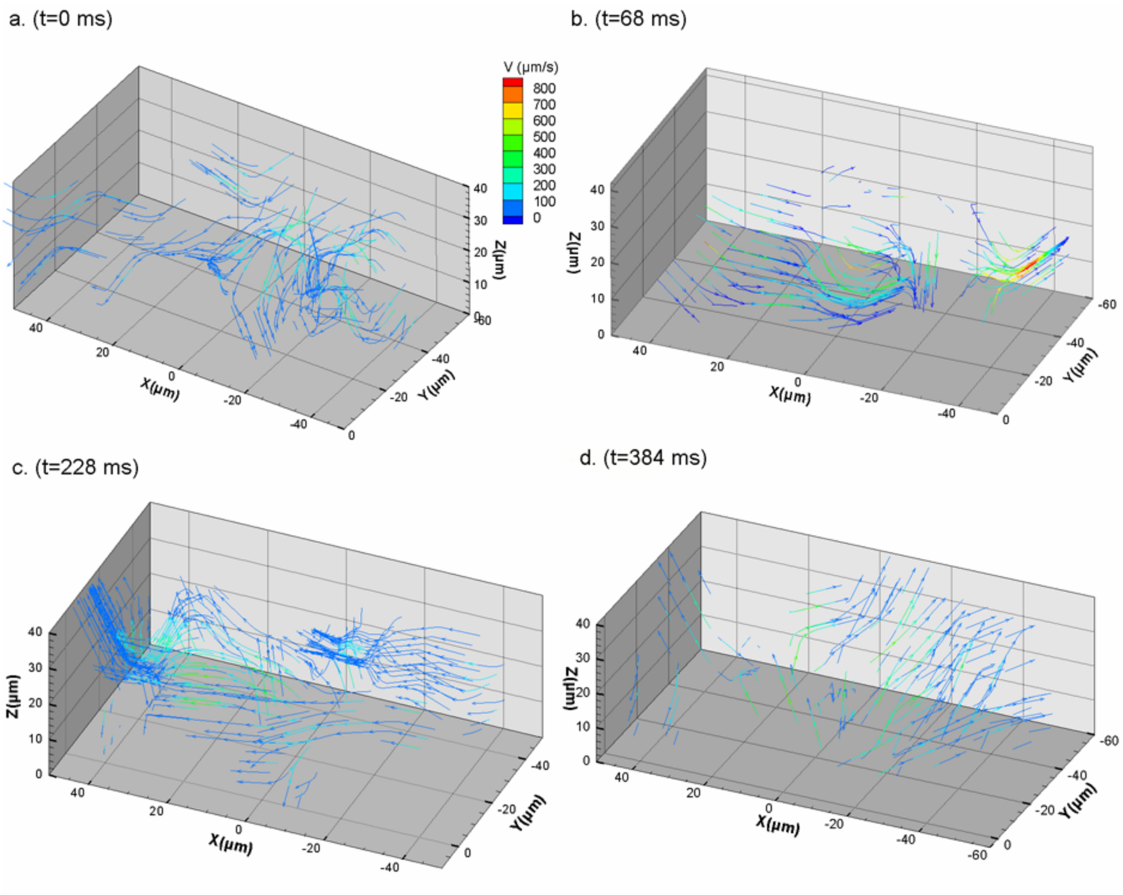

Figure 5.15. Streamlines of blood flow in a 56-hpf ventricle during a cardiac cycle: (a) streamlines in early systole, (b) in mid systole, (c) in early diastole, (d) in mid of diastole.

5.5 Conclusion and discussion

The newly developed micro DDPIV imaging system has been successfully implemented to three-dimensional real-time imaging of highly dynamic cardiac cell motions including blood flow and heart wall motions in living zebrafish embryos. Fluorescent microspheres were introduced into the cardiovascular systems to serve as markers to help describe the dynamic motions.

Blood flow in the yolk sac is observed to follow the structure of the surrounding tissues. 3D Flow velocities and heart wall motion trajectories in early heart tube and later heart chambers have been reconstructed based on the defocusing images acquired by a high-speed camera. Analysis of blood flow patterns and deformation of heart walls during a heart beat has been carried out. Blood flow following a suction pump mechanism in an early heart tube (32-hpf) has been resolved. It took about four cardiac cycles for a blood tracer particle to flow into the ventricle. Longitudinal and radial displacements in the atrium and the ventricle shows a phase difference between the wall motions, predicting a wave propagating along the heart tube. Diameter changes in a prominently separated atrium and ventricle (48-hpf) provide evidences of a compression wave in the heart. Comparing with a model of traveling wave in a tube, one can find that a suction wave is initiated in the atrium and produces resonance in the ventricle including contraction and expansion. Phase and duration differences between the inactive periods in both chambers confirm the wave propagating. Nonlinear strain tensors of ventricular deformations are able to be calculated, describing morphology changes such as wall thickening and twisting during a cardiac cycle. Difference of wall motions between 32-hpf and 42-hpf heart is also described. Velocity fields of blood flow in a 59-hpf atrium and a 56-hpf ventricle are obtained which shows the complex flow characteristics, such as retrograde flow and blood filling, in the embryonic heart.

Some limitations still exist in the application of this approach. The injected polystyrene microspheres are likely to stick to the endocardium, which impairs the ablility as blood flow tracers. A possible solution would be treating the microspheres in some cultures (e.g., PEG) to prevent endothelial cells from trapping the particles. In this research image sequences are acquired immediately after a successful injection to guarantee proper imaging of the blood flow. Low light condition is another difficulty for in vivo imaging. High-power illumination and an imaging intensifier are used to collect the weak signals from a living heart. Long-term tracking of heart wall motions by trapped particles is possible but can not last for long (e.g., 12 hours) because light scattering at surrounding tissues becomes more evident in hours after injection, providing more background and reducing the image contrast.

Given objective lenses with proper magnification and adequate markers, the present microscopic imaging system is capable of resolving 3D motions in other living organs. Details of the effects of optical configuration on micro DDPIV system are discussed in Appendix A. Future work would enhance the image quality by adjusting optical configurations and illumination approaches to broaden the application of this technique for in vivo imaging.

References:

Forouhar AS, Liebling M, Hickerson AI, Naisrei-Moghaddam A, Tsai HJ, Hove JR, Fraser SE, Dickinson ME, Gharib M (2006) The embryonic vertebrate heart tube is a dynamic suction pump. *Science* 312: 751-753.

Fung YC (1990) Biomechanics: Motion, Flow, Stress, and Growth. Springer-Verlag, New York.

Hickerson AI (2005) An experimental analysis of the characteristic behaviors of an impedance pump. Ph. D thesis, California Institute of Technology.

Hove JR, Köster R., Forouhar AS, Acevedo-Bolton G, Fraser SE, and Gharib M (2003) Intracardiac fluid forces are an essential epigenetic factor for embryonic cardiogenesis. *Nature* 421: 172-177.

Hu N, Sedmera D, Yost J. et al. (2000) Structure and function of the developing zebrafish heart. *Anat Record* 260: 148-157.

Liebling M, Forouhar AS, Wolleschensky R, Zimmermann B, Ankerhold R, Fraser SE, Gharib M, and Dickinson ME (2006) Rapid three-dimensional imaging and analysis of the beating embryonic heart reveals functional changes during development. *Dev Dyn* 235: 2940-2948.

Lu J, Pereira F, Fraser SE, Gharib M Three-dimensional real-time imaging of cardiac cell motions in living embryos. *J Biomed Opt* (In print).

Pereira F and Gharib M (2002) Defocusing digital particle image velocimetry and the three-dimensional characterization of two-phase flows. *Mea. Sc. Technol* 13: 683-694.

Rademarkers FE, Rogers WJ, Guier WH, Hutchins GM, Siu CO, Weisfeldt ML, Weiss JL, Shapiro EP (1994) Relation of regional cross-fiber shortening to wall thickening in the intact heart three-dimensional strain analysis by NMR tagging. *Circulation* 89: 1174-1182.

Walderman LK, Fung YC, and Covell JW (1985) Transmural myocardial deformation in the canine left ventricle normal in vivo three-dimensional finite strains. *Circ Res* 57: 152-163.

Westerfield M (2000) The zebrafish book. A guide for the laboratory use of zebrafish (Danio rerio). 4th ed. University of Oregon Press.

Chapter 6

Conclusions

The main objective of this project is to develop a visualization approach to acquire real-time volumetric information for quantitative study of micromechanics in complex three-dimensional microfluidic systems as well as mechanical factors involved in cardiovascular cell motions in vivo. A novel high-speed three-dimensional microscopic imaging system has been successfully built based on the defocusing technique (DDPIV) with laser-induced fluorescence to provide quantitative analysis on microscale complex dynamic systems. The present microscopic imaging modality is capable of resolving 3D spatial information by recording the defocused image patterns of the flow tracers produced by a mask with three apertures forming an equilateral triangle. Inaccessibility of the optical parameters of an objective lens brings difficulties to resolve the depth coordinates through geometrical analysis. The technique is validated by a calibration procedure which establishes the relationship between a tracer's depth position and the separation between its corresponding defocusing images. Calculation of 3D spatial coordinates by the defocusing concept does not require any information (such as motion period) of the imaged motion. The microscope is equipped with a high-speed camera acquiring data at up to several thousand frames per second, providing sufficient speed to acquire fast-moving motions. Additionally, all the 3D data were resolved by this method without any time delay as triangular pattern matching was performed at each single defocused image. Therefore the calculated 3D information provides real-time information inside a microscopic volume of interest.

We then utilized the 3D microscopic system to visualize the internal circulation due to evaporation inside a 2-mm water droplet on a nearly hydrophobic substrate. Flow patterns in the center and near the edge of the droplet were visualized in the experiments. Fountain-like flow in the center and vortex flow near the edge were observed, providing evidences of convection flow induced by Marangoni effects. We further investigated the structure of the toroidal particle trajectories in the center and confirmed the existence of vortex flow in all three planes.

The imaging system has then been applied to 3D imaging of cardiac cell motions in living zebrafish embryos. With proper fish handling and delicate microinjection at the fish tail, we were able to introduce micron/sub-micron fluorescent microspheres into the blood stream. And thereby the cardiovascular blood flow was immediately visible and heart walls were also labeled when injected particles adhered to the endocardium within minutes. These trapped particles always followed the same trajectories throughout several cardiac cycles, while particles in the blood stream moved out of the heart after a complete heart beat. Therefore particles in the heart wall can be easily identified and separated through an image sequence where a few cardiac cycles were recorded. Dynamic motions of the blood flow and heart wall motions have been quantitatively mapped. Blood flow in the yolk sac was seen to follow the approximately spherical structure of the surrounding tissues. A pumping flow in the early heart tube was evident in the 3D flow field, where some blood flow tracers spent four cardiac cycles to enter the ventricle from the atrium. Phase differences between heart walls of the atrium and the ventricle as well as heart wall motions and blood flow during a cardiac cycle have been investigated, exhibiting more active motions in the ventricle. Furthermore, ventricular wall motions in a 32-hpf heart are observed to be mostly longitudinal and radial, while in a 42-hpf ventricle circumferential and radial motions are more prominent and out-of-plane torsional deformations are evident. Endocardial 3D strains in the ventricle were calculated based on the reconstructed coordinates of two particles in the ventricular wall. Complex blood flow patterns in the atrium and the ventricle at older stages were also measured, describing interesting flow phenomena in the heart chambers during a cardiac cycle. Throughout the course of this study, we provide valuable information and significant findings for better understanding of mechanical factors in cardiac motions.

Some difficulties still exist in the imaging technique and the visualization method which limit further application of in vivo quantitative analysis. High intensity illumination and very bright tracers are needed as the aperture mask which generated the defocused patterns blocked a major portion of the emitted light. The depth of the field was limited to 40 μm because a 20X objective lens with high numerical aperture was adopted to allow more light passing through. Microinjection was not able to accurately locate the particles in the entire regions of interest. Furthermore, the injected tracer particles could not be used for long-term blood flow mapping as they moved out of the blood stream in several hours. Similarly, particles are not suitable for long-term wall motion tracers in an identical heart due to the increasing tissue scattering with time.

Effects of optical configuration on micro DDPIV system have been discussed. Further adjustments of the optical configurations in the 3D imaging system are critical to enhance the light budget and the capability of the technique at extremely low light conditions. Future work will have to search for optimal flow tracers not intended to be trapped in the tissues, or to treat the current microspheres with chemical solutions to prevent tissue trapping. Because the current injection needle can not easily penetrate the fish skin after 3 dpf, another noninvasive approach to introduce tracers into the blood stream of embryonic zebrafish at older stages (i.e., older than 72 hpf) would be found to image cardiac motions in the heart when intense morphological changes such as valve formation occurs. Alternatively, an integration of the imaging technique with fluorescent labeled zebrafish mutants would largely reduce the difficulties induced by externally injected tracers. The demonstrated real-time 3D imaging systems opened numerous windows to explore volumetric quantitative information in dynamic living biological systems as the techniques is generally applicable to any system with optical accessibilities. Given appropriate objective lenses and cameras, dynamic motions within other organs such as the brain, the kidney, and the circulation systems can be adequately analyzed based on this technique.

Appendix A. Optical configuration in micro DDPIV system

Optical parameters in the micro DDPIV system are known to affect the capabilities of the imaging technique. It has been discussed in Chapter 3 that separation between apertures (d) in the mask is related to the depth resolution of the system. In this chapter, I will discuss the effects of optical parameters on the defocusing images and the depth of field of the imaging system.

The depth of field of an objective lens in a microscope is defined as:

$$d_{tot} = \frac{\lambda \cdot n}{NA^2} + \frac{n \cdot e}{M \cdot NA} \qquad \text{A.1}$$

Where **λ** is the wavelength of illuminating light, **n** is the refractive index, **e** is the smallest distance can be resolved by a detector in the focal image plane (typically between 4 μm and 24 μm), **M** is the magnification and **NA** represents the numerical aperture (Nikon MicroscopyU). By attaching a mask with three apertures, the objective lens in the microscope is converted into three equivalent lenses with equivalent numerical aperture **NA_{eq} = $NA*D_a/D_m$**, where **D_a** and **D_m** are diameters of the pinholes and the mask, respectively. Therefore the depth of field of the micro DDPIV system is given by

$$d_{tot} = \frac{\lambda \cdot n \cdot D_m^2}{NA^2 \cdot D_a^2} + \frac{n \cdot e \cdot D_m}{M \cdot NA \cdot D_a} \qquad \text{A.2}$$

In the current imaging system, λ = 515 nm, n = 1, $e \approx 17$ µm, M = 20, NA = 0.75, D_m = 20 mm. Given the pinholes used in experiments with D_a = 2 mm, the depth of field of the defocusing system d_{tot} = 113 µm, which is consistent with the measurement in the experiments (details in Chapter 3). If all triangular patterns in an image are oriented in the same direction, such as the data acquired in the zebrafish heart (Chapter 5), the measurable depth $d_m = 0.5d_{tot}$.

Low light intensity of the defocusing images remains a challenge in this technique, which limits extensive applications to biological systems with low optical accessibility. Light intensity I of a microscopic image is proportional to NA^2 and $1/M^2$ of the objective lens. Given the same magnification, a mask with larger pinholes or an objective lens with higher NA will induce higher NA_{eq}, and consequently increases the light intensity (I) of the defocused images. However, the depth of field d_{tot} will be seriously reduced according to Eq. A.2. Additionally, larger pinholes in the aperture mask generate larger defocusing images at the same depth position (w), which generate more overlaps in the particle images and in turn induce more errors in image detection and triangle matching. Fig. A.1 shows the defocusing images generated at the same depth in the current experimental system by three masks with different pinhole sizes. Effects of optical parameters on micro DDPIV system are summarized in Table 1.

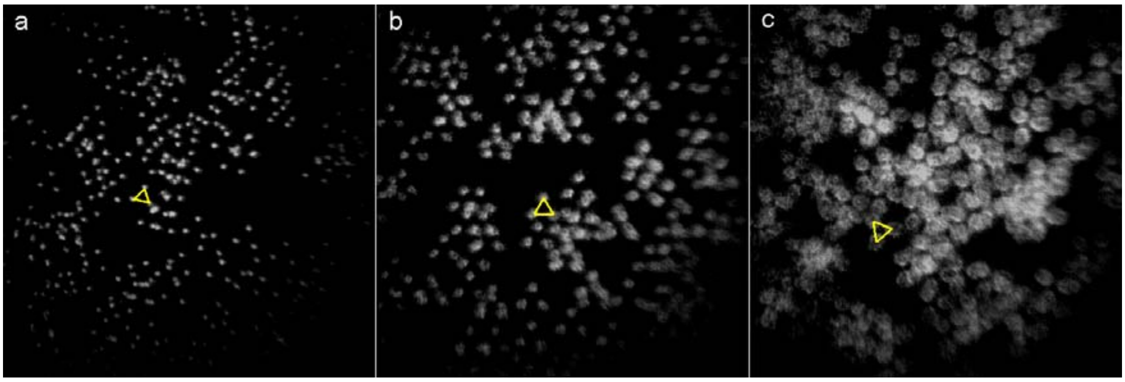

Figure A.1. Defocused images generated from masks with different pinhole sizes and identical aperture separation (d = 7mm) at relative depth w = 10 µm. (a) D_a = 2 mm, d_{tot} = 120 µm; (b) D_a = 4 mm, d_{tot} = 60 µm; (c) D_a = 6 mm, d_{tot} = 25 µm. A sample triangular pattern is linked in each image. Depth of field of the system is reduced if increasing the pinhole diameter. Particle detection generates less than 5% error in image (a), while 20% error in (b) and almost 50% in (c).

Table A.1. Effects of optical parameters on micro DDPIV system.

Parameters	**M**	**NA**	D_a
Effects on the system	Higher **M** reduces **I** and d_{tot}.	Higher **NA** increases **I**, and reduces d_{tot}.	Higher D_a increases **I**, reduces d_{tot}, increases image sizes, and thereby induces more errors in particle detection.

In general, application of micro DDPIV technique for 3-D real-time imaging requires a microscope equipped with a 3-pinhole aperture mask in the back of the objective. Incident light (i.e., bright field illumination or fluorescence excitation) will enter the objective from the front. An objective lens with appropriate magnification and tracers with proper sizes labeling the volume of interest are required such that the tracers are clearly separated in the images. Large aperture separation (**d**) is usually recommended in the mask design to obtain high depth resolution. Proper objective **NA** and pinhole diameter $\mathbf{D_a}$ (typically between 1 mm and 4 mm) has to be selected to generate relatively small defocused images with sufficient intensity and produce high depth of field to map the whole volume of interest. Defocused triangular image patterns will be recorded by a high-speed camera and reconstructed by DDPIV 4.5.1 software package developed by Pereira et al (2006). The maximum number of particles can be resolved is about 1500 from a 512X512 pixel^2 image.

References:

Nikon MicroscopyU. http://www.nikonmicroscopyu.com.

Pereira F, Graff EC and Stuer H (2006) DDPIV 4.5.1. California Institute of Technology, Pasadena, CA 91125 USA.

Appendix B[*]

Movie 1. Blood flow in a 32-hpf heart tube over 5 cardiac cycles with two particles adhered to the heart wall.

Movie 2. A beating 48-hpf zebrafish heart with the wall labeled by injected tracer particles.

Movie 3. A 42-hpf ventricle in a zebrafish embryo with the wall labeled by tracer particles.

Movie 4. Blood flow in a 59-hpf zebrafish atrium throughout a cardiac cycle.

Movie 4. Blood flow in a 56-hpf zebrafish ventricle throughout a cardiac cycle.

---

[*] Please note that movie series (a) are defocusing image sequences of tracer particles and series (b) are the reconstructed flow fields. Defocusing image patterns in Movie 2(a) are upright triangles while in other movies are triangles pointing downwards. Velocity magnitudes in movie series (b) are color coded. Sizes of spheres in Movie 3(b), 4(b), and 5(b) represent particle depth positions.